2010

Experimental And Theoretical Study Of The Optical Properties Of Semiconductor Quantum Dots

Gero Nootz
University of Central Florida

EXPERIMENTAL AND THEORETICAL STUDY OF THE OPTICAL PROPERTIES OF SEMICONDUCTOR QUANTUM DOTS

by

GERO NOOTZ
Dip.Ing. Fachhochschule Lübeck, 1999

A dissertation submitted in partial fulfillment of the requirements
for the degree of Doctor of Philosophy
in the Department of Physics
in the College of Sciences
at the University of Central Florida
Orlando, Florida

Fall Term
2010

Major Professors: Eric W. Van Stryland and David J. Hagan

ABSTRACT

The aim of this dissertation is to gain a better understanding of the unique electronic structure of lead salt quantum dots (QDs) and its influences on the nonlinear optical (NLO) properties as well as the time dynamics of the photogenerated charge carriers. A variety of optical techniques such as Z-scan, two-photon excited fluorescence and time-resolved pump probe spectroscopy are used to measure these properties.

The one-photon as well as the degenerate and nondegenerate two-photon absorption (2PA) spectra are measured and the electronic wave functions from a four-band envelope function formalism are used to model the results. We observe local maxima in the 2PA spectra for QD samples of many different sizes at energies where only 1PA is predicted by the model. This is similar to the previously measured transitions in the 1PA spectra which are not predicted by the model but accrue at the energies of the two-photon allowed transitions. Most importantly we observe 2PA peaks for all samples at the energy of the first one-photon allowed transition. This result can only be understood in terms of symmetry breaking and therefore is strong evidence that other transitions, not predicted by the model if the selection rules are left intact, also have the origin in the lifted spatial symmetry of the wave functions. On the other hand, the uniquely symmetric eigenenergies of these quantum-confined energy states in the conduction and valance bands explain the observed trend toward larger two-photon cross-sections as the quantum confinement is increased in smaller QDs. Moreover, this unique feature is shown to reduce the possible relaxation channels for photoexcited carriers, which is confirmed experimentally by the reduced carrier relaxation rate as compared to CdSe QDs which lack this symmetry. Carrier multiplication (CM), a process in which several electrons are excited by the

absorption of a single photon is studied in PbS QDs. We show that for PbS QDs with radius smaller than 2.5 nm the parameters of CM get very close to the theoretical optimum. Next-generation solar cells operating under these ideal conditions could potentially have conversion efficiency of up to 42%. This compares favorably to the 30% efficiency limit of a single junction silicon solar cell.

ACKNOWLEDGMENTS

I thank Dr Eric Van Stryland and Dr. David Hagan for the opportunity to work in the Nonlinear Optics Group. I'm grateful for their excellent mentoring and support throughout the years. Their personalities created a cooperative and friendly atmosphere which made working in the NLO group very fruitful and enjoyable. I also would like to thank my colleagues, many of whom have become dear friends, for their willingness to lend a helping hand whenever possible and for the many discussions on both practical and theoretical problems. I extend my special thanks to Lazaro Padilha for his motivation, interest and deep involvement in this work.

Lastly, my heartfelt thanks goes to my parents, for being there for me every step of the way.

TABLE OF CONTENTS

LIST OF FIGURES

LIST OF TABLES

LIST OF ACRONYMS/ABBREVIATIONS

1PA	One-Photon Absorption
2PA	Two-Photon Absorption
2PF	Two-Photon Excited Fluorescence
cm	Centimeter
eV	Electron-Volt unit of energy
ESA	Excited State Absorption
fs	Femtosecond (10^{-15}s)
FWHM	Full Width Half Maximum
GM	Goppert-Mayer unit for the 2PA cross-section
GVD	Group-Velocity Dispersion
GVM	Group-Velocity Mismatch
IR	Infrared
ISRE	Intermediate State Resonance Enhancement
kHz	Kilohertz (10^3 Hz)
μJ	Microjoule (10^{-6} J)
μm	Micrometer (10^{-6} m)
NBF	Narrow Band Filter
nJ	Nanojoule (10^{-9} J)
nm	Nanometer (10^{-9}m)
NLA	Nonlinear Absorption
NLR	Nonlinear Refraction
OPA	Optical Parametric Amplifier

OPG	Optical Parametric Generator
pJ	Picojoule (10^{-12} J)
ps	Picosecond (10^{-12} s)
QCL	Quantum Confined Level
QD	Quantum Dot
RSA	Reverse Saturable Absorption
TA	Transient Absorption
WLC	White-Light Continuum

CHAPTER 1:
INTRODUCTION

1.1. *Background and Motivation*

Since the first successful synthesis of colloidal semiconductor quantum dots (QD) in the early 1980s these materials have been under intense investigation. Semiconductor QDs are the logical conclusion of a trend which starts with utilization of one dimensional quantum confinement in the so called quantum wells and then two-dimensional confinement in quantum wires. In semiconductor quantum dots the electronic wavefunctions are confined in all three dimensions, which leads to discrete energy levels reminiscent of the atoms orbitals. As a man-made material, sometimes coined 'artificial atoms", they come with inherent flexibilities which allow us to tailor their optical properties to suit the application at hand. Nowadays semiconductor QDs are being used or are considered promising candidates for diverse applications such as saturable absorbers [1], solar cells [2], q-bits [3] and lasing media [4]. In addition to these practical applications, the relatively simple structure of these materials allows the study of quantum confinement effects in a controlled environment.

Many of their potential applications utilize the nonlinear optical (NLO) properties of these materials [1, 2, 5]. Several strategies, such as resonance enhancement, stronger quantum confinement and selection of the right starting materials, can be utilized to enhance the nonlinear optical response. This study is motivated by the need to better understand the physics of these systems in order to make these NLO based applications a reality.

1.2. *Outline*

Chapter 2 is devoted to an introductory discussion of the effects of quantum confinement in semiconductors and outlines the four-band envelope function model employed to calculate the electronic wave functions in these systems. It furthermore explains how these wavefunctions can be used to calculate the one-photon as well as the degenerate and nondegenerate two-photon transitions. In Chapter 3 the experimental techniques utilized for the measurement of the nonlinearities are introduced and discussed with respect to their weaknesses and strengths. Also the laser systems used in this study are discussed. Chapter 4 introduces the lead salt QDs. The unique properties of these materials are discussed and the experimental results from the 2PA measurements are compared to the predictions of the four-band envelope function theory. The relaxation dynamics of excited charge carriers in PbS QDs are discussed in Chapter 5. Carrier-multiplication a process in which several electrons are promoted to the conduction band by the absorption of a single photon is the topic of Chapter 6. Chapter 7 provides concluding remarks. In the appendix a step by step guide to the operation of the MathCad code written to calculate the energies and oscillator strength according to the four-band envelope function model is given.

CHAPTER 2:
THE EFFECTS OF QUANTUM CONFINEMENT IN SEMICONDUCTORS

2.1. *Introduction*

The band structure in a crystalline bulk material is derived from the possible wavefunctions of an electron in a spatially infinite but periodically varying potential of the lattice structure. The wave functions can be represented by Bloch-Functions which are the solutions to the equation of motion of an electron under these conditions. According to Bloch's theorem the eigenfunction of the electrons can be represented as the product of a plane wave ($e^{i\mathbf{k}\cdot\mathbf{r}}$) and a function with the same periodicity as the as the lattice potential $u_k(\boldsymbol{r})$ [6].

$$\psi(\boldsymbol{r},t) = u_{n,k}(\boldsymbol{r})\, e^{i(\mathbf{k}\cdot\mathbf{r}-\omega t)} \qquad (2\text{-}1)$$

The eigenvalues of Bloch's functions are the energies of an electron with a given $\boldsymbol{k}$. This gives the dispersion relations $E(\boldsymbol{k})$ and leads to energy regions with a quasi continuum density of states and other energy regions where the density of states is zero. Energy regions with a continuous density of states, in the terminology of solid states physics, are named "Energy Bands". Each band can accommodate 2N electrons where N is the number of atom of the sample [6]. Since electrons are Fermions, i.e. no two electrons can occupy the same state, each electron, in the confines of the periodic lattice, apart from the spin, must have a different **k**. Therefore, the electrons (at zero temperature) will first occupy the lowest available states and depending whether the number of valence electrons per unit cell is even or odd will either completely or partially fill an energy band. If a band is only partially filled, as in a monovalent metal i. g. Cu, Au and Ag, the electrons can easily transition to unoccupied states thereby changing the charge distribution and an electric current can flow; the material is a conductor. On the other hand, if the

number of valence electrons is even all the available states are occupied and if the filled band dose not overlap with lowest laying empty band an electronic current is not possible i.e. the material at is an insulator. A semiconductor is essentially a dielectric in the sense that is has fully occupied bands, but the energy gap between the first fully occupied and empty band is narrow ($\lesssim 4eV$). This criteria is somewhat arbitrary, but the discerning factor is that at finite temperatures electrons from the valence band or from impurities can be thermally excited into the conduction band where they can now freely move and generate an electronic current. For a semiconductor, the energetically lowest fully occupied band is the valence band and the first empty band is called the conduction band.

This thesis is only concerned with semiconductors,.Quantum structures of other materials. i. g. metal nanoparticles [7], while interesting, will not be discussed.

2.2. ***Quantum confinement in semiconductors***

If the dimensions of a semiconductor crystal are reduced in size to an extent that they are comparable to the wavelength of the electronic wavefunctions, quantum confinement effects become observable. Assuming an infinite potential well the amplitude of the wavefunctions have to be zero at the boundary of the quantum confined structure. Therefore in the direction of the confined dimension only states which have wavevectors satisfying

$$k_n = \frac{n\,\pi}{L}, \tag{2-2}$$

can exist, here n is integer and L is the extent of the confined dimension. The density of states, which in the case of the bulk semiconductor was a continuum in $\boldsymbol{k}$, now becomes limited to specific $\boldsymbol{k}$ vectors and therefore to discrete energies. In Fig. 2-1 the density of states as a function

of energy is shown for different degrees of quantum confinement. In the bulk semiconductor, where there is no quantum confinement, the density of states is a monotonically rising function of energy. For the quantum well the confinement is in one dimension and the density of states has a step-like form. Confining space in one more dimension one arrives at the so called quantum wires which have narrow spikes in there density of states function. Finally, if the wavefunctions are constrained in all three dimensions the allowed states have discrete energies. These structures are the quantum dots which are the topic of this work.

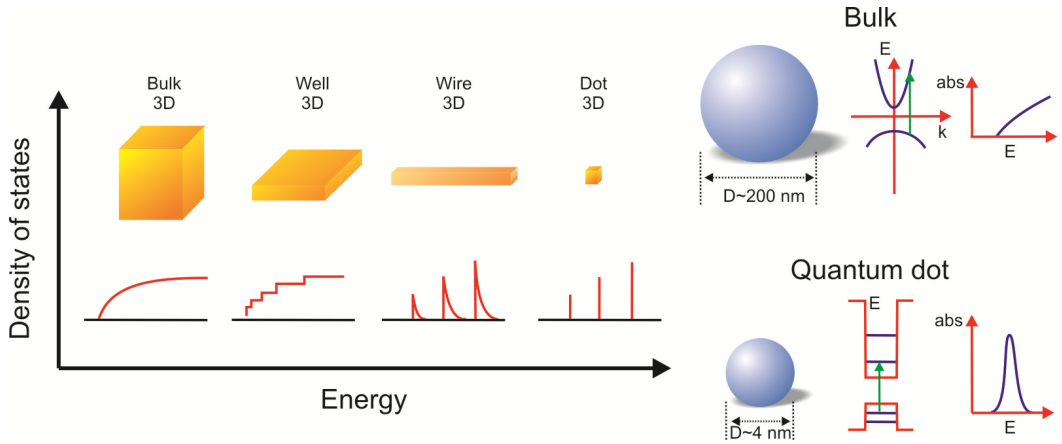

Figure 2-1: The effect of quantum confinement on the density of states.

An effective-mass or synonymic parabolic band model can be used to demonstrate the most prominent features in a spherical QD with infinite potential barriers. By confining the parabolic bands in a spherical and infinite potential the energies for the quantum confined states in the valence and conduction band are calculated as [8, 9]

$$E_{n,l}^{e,h} = E^{c,v} \pm \frac{\hbar^2 \, \xi_{nl}^2}{2 \, m^{e,h} \, R^2}. \qquad (2\text{-}3)$$

Where $E^{c,v}$ is the band-edge energy of the bulk semiconductor, ξ_{nl}^2 are the zeros of spherical Bessel functions, m denotes the effective mass of either the electron or the hole, R is the radius of the QD and $+$ or $-$ are used to calculate the energies in the conduction or valence band respectively. From Eq. 2-2 it is clear that the minimum energy separation of the quantum confined levels in a QD is the bandgap of the bulk semiconductor. In this three dimensional quantum confined structure the charge carriers cannot separate and therefore "feel" each other through the Coulomb force i. e. electrons and holes from excitons. This is in contrast to the bulk semiconductor where potential excitons dissociate readily due to their small binding energy. It is therefore common in this context to use the term "exciton" to describe the excited state of a QD. Only for structures comparable in size to the Bohr radius of the exciton in a given material does quantum confinement significantly increase the bandgap. Fig. 2-2 gives an overview of several regularly used QD materials and the energy range over which their bandgap is tunable by varying the radius.

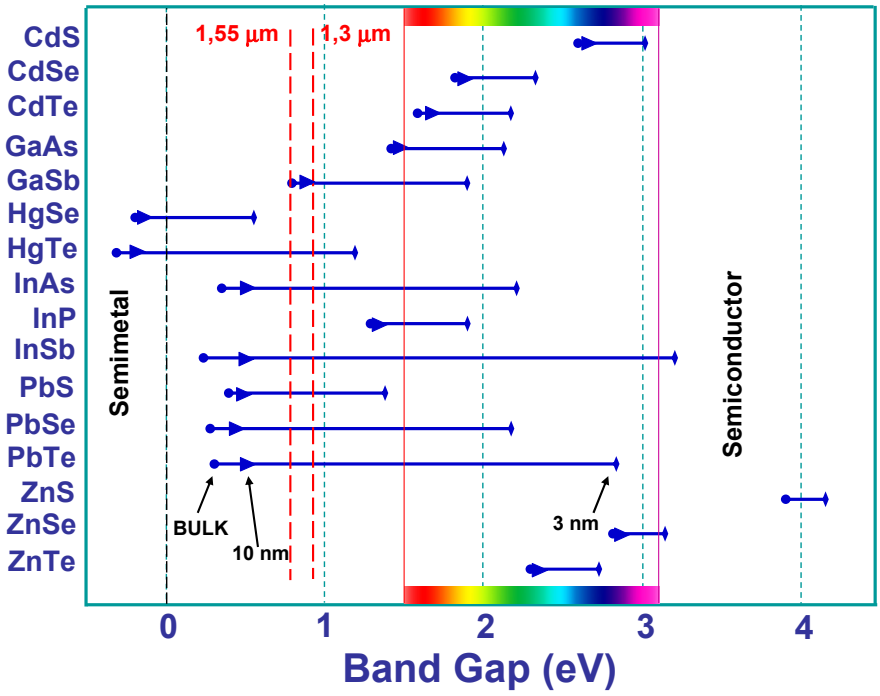

Figure 2-2: Tunability of the bandgap energy of common QD systems

The energetic states of a single QD are of discrete energy, and homogeneously broadened according to the dephasing time [10]. In practice it has been very difficult to synthesize QDs with a narrow size distribution and therefore the linear absorption spectrum of an assembly of QDs is dominated by inhomogeneous broadening due to the size distribution of the QDs. However, great progress has been made in recent years and QD samples with size distributions < ±5% can be synthesized. In these samples the linear absorption spectrum clear shows a blue shift of the onset of the absorption and pronounced peaks due to transitions between the quantum confinement induced discrete energy levels are observed (see Fig. 2-3).

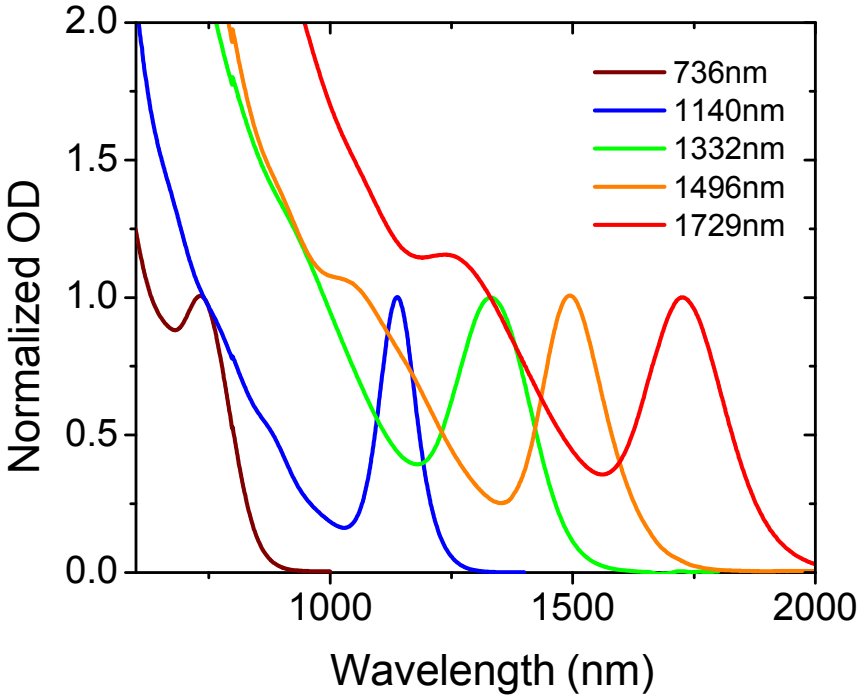

Figure 2-3: Linear absorption spectrum of a PbS QD samples with different average sizes.

The parabolic band approximation is only valid in the vicinity of k = 0. For smaller quantum dots, which require high k values in order to satisfy Eq. 2-2, this is clearly not valid and the effective mass approximation strongly overestimates the quantum confinement energy (see Fig. 2-4). Several theoretical approaches improve upon this simple model [11-13]: most notably the tight binding approach, the pseudo potential approach and the ***k·p*** approach. The tight binding model uses the wavefunction of an individual atom and by superposition attempts to build up the electronic band structure of the solid. As such it is somewhat limited by the total number of atoms which can reasonably be considered and is thus especially useful for smaller QDs [11]. The pseudopotential approach on the other hand uses an empirical shape of the lattice potential of the bulk semiconductor and then applies boundary conditions to these functions representing

the finite dimensions of the QD. The potential is found by searching for a shape of the lattice potential which reproduces band parameters which have been measured or calculated from first principle [12, 13]. The ***k·p*** method, like the pseudopotential method, starts with the wavefunctions of the bulk semiconductor, but then uses mathematical methods to separate the slowly varying envelope function from the rapidly varying Bloch functions. In this way analytical solutions to the quantum-confined wavefunctions can be found. In this work the ***k·p*** method as developed by Kang and Wise [14] is used to calculate the QCL in PbS and PbSe QDs. The ***k·p*** method is outlined in the next chapter.

2.3. *k·p Band Calculations*

The ***k·p*** method is based on Loewdin perturbation theory [15] which allows the rapidly varying Bloch part $u_{n,k}(r)$ in Eq.2-1 to be separated from the slowly varying envelope functions. By diagonalizing the Hamiltonian the electronic wave functions are then comprised of only the slowly varying envelop functions [16-18]. If the ***k·p*** method is used to calculate the wave functions of the QCL in a quantum confined structure, appropriate boundary conditions are imposed on the slowly varying envelope functions of the electronic wavefunctions of the bulk material.

The ***k·p*** calculations for the lead salt QDs was derived by Kang and Wise in 1997 [14]. They uses the ***k·p*** Hamiltonian of lead salts crystal according to Michell and Wallis [19] as well as by Dimmock (Eq. 2-4) where the parameters are given in Table 2-1.

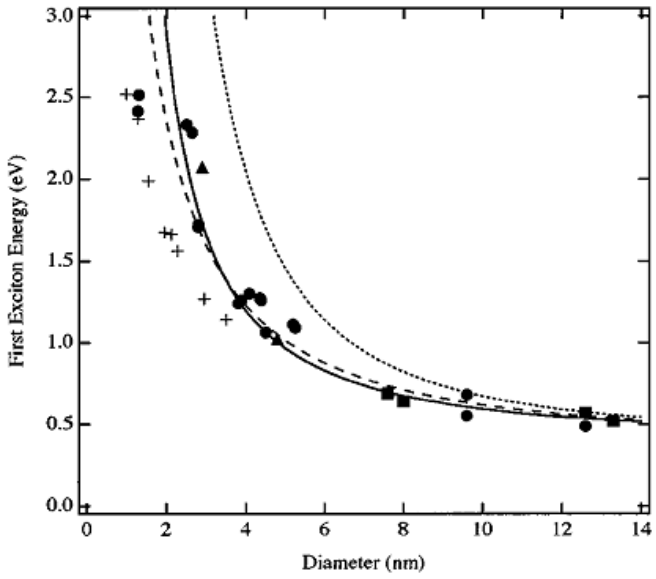

Figure 2-4: Energy of the first excited state; theoretical calculation (lines, and crosses) versus experiment (filled symbols). Solid, dashed and dotted curves are from the **k·p**, hyperbolic-band and parabolic-band model respectively. Crosses are the confinement energies according to the tight-binding calculations [14].

$$\begin{pmatrix} \frac{E_g}{2}+\frac{\hbar^2 k_t^2}{2m_t^-}+\frac{\hbar^2 k_z^2}{2m_l^-} & 0 & \frac{\hbar}{m}P_l k_z & \frac{\hbar}{m}P_t(k_x-ik_y) \\ 0 & \frac{E_g}{2}+\frac{\hbar^2 k_t^2}{2m_t^-}+\frac{\hbar^2 k_z^2}{2m_l^-} & \frac{\hbar}{m}P_t(k_x+ik_y) & -\frac{\hbar}{m}P_l k_z \\ \frac{\hbar}{m}P_l k_z & \frac{\hbar}{m}P_t(k_x-ik_y) & -\frac{E_g}{2}-\frac{\hbar^2 k_t^2}{2m_t^+}-\frac{\hbar^2 k_z^2}{2m_l^+} & 0 \\ \frac{\hbar}{m}P_t(k_x+ik_y) & -\frac{\hbar}{m}P_l k_z & 0 & -\frac{E_g}{2}-\frac{\hbar^2 k_t^2}{2m_t^+}-\frac{\hbar^2 k_z^2}{2m_l^+} \end{pmatrix} \quad (2\text{-}4)$$

Table 2-1: Parameters of the **k·p** Hamiltonian for PbS and PbSe [14]

	E_g (eV)	m/m_t^-	m/m_l^-	m/m^-	m/m_t^+	m/m_l^+	m/m^+	$2P_t^2/m$ (eV)	$2P_l^2/m$ (eV)	$2P^2/m$ (eV)
PbS	0.41	1.9	3.7	2.5	2.7	3.7	3.0	3.0	1.6	2.5
PbSe	0.28	4.3	3.1	3.9	8.7	3.3	6.9	3.0	1.7	2.6

The derivation of the wave functions, following Kang and Wise is outlined in the following. The Hamiltonian (2-4) can be separated into a spherically symmetric part ($\widehat{H}_0$) and an anisotropic part ($\widehat{V}$) (Eq. 2-5 and Eq. 2-6 respectively), where the later is small and could be treated as a perturbation, but will be ignored in the reminder of this work.

$$\widehat{H}_0(k) = \begin{pmatrix} \left(\frac{E_g}{2} + \frac{\hbar^2 k^2}{2m^-}\right)\mathbf{1} & \frac{\hbar P}{m}\,\boldsymbol{k}\cdot\boldsymbol{\sigma} \\ \frac{\hbar P}{m}\,\boldsymbol{k}\cdot\boldsymbol{\sigma} & -\left(\frac{E_g}{2} + \frac{\hbar^2 k^2}{2m^+}\right)\mathbf{1} \end{pmatrix} \tag{2-5}$$

$$\hat{V} = \begin{pmatrix} \epsilon_- T_0^{(2)} & 0 & \delta_l T_0^{(1)} & \sqrt{2}\delta_t T_{-1}^{(1)} \\ 0 & \epsilon_- T_0^{(2)} & -\sqrt{2}\delta_t T_1^{(1)} & -\delta_l T_0^{(1)} \\ \delta_l T_0^{(1)} & \sqrt{2}\delta_t T_{-1}^{(1)} & \epsilon_+ T_0^{(2)} & 0 \\ -\sqrt{2}\delta_t T_1^{(1)} & -\delta_l T_0^{(1)} & 0 & \epsilon_+ T_0^{(2)} \end{pmatrix} \tag{2-6}$$

Eq. 2-6 is not used in in this work and only included for completeness. The parameters $\epsilon_-, \epsilon_+, \delta_l$ and δ_t as well as the operators $T_0^{(1)}$and $T_0^{(2)}$ can be found in the literature [14].

In the spherical part of the Hamiltonian **1** is a 2×2 unit matrix and **σ** is the Pauli spin matrix. The electronic wave functions can be obtained by solving the Schrödinger Equation for the spherical part of the Hamiltonian.

$$\widehat{H}_0 \mathcal{F}(\boldsymbol{r}) = E\,\mathcal{F}(\boldsymbol{r}) \tag{2-7}$$

In this notation $\mathcal{F}(\boldsymbol{r})$ are the eigenvectors whose components are the envelope functions of the Bloch equations which representing the bands.

$$\mathcal{F}(\boldsymbol{r}) = [F_1(\boldsymbol{r}),\, F_2(\boldsymbol{r}),\, F_3(\boldsymbol{r}),\, F_4(\boldsymbol{r})] \tag{2-8}$$

The complete wavefunction is then constructed as

$$|\psi(\boldsymbol{r})\rangle = F_1(\boldsymbol{r})|L_6^- \uparrow\rangle + F_2(\boldsymbol{r})|L_6^- \downarrow\rangle + F_3(\boldsymbol{r})|L_6^+ \uparrow\rangle + F_4(\boldsymbol{r})|L_6^+ \downarrow\rangle, \tag{2-9}$$

or

$$|\psi(\boldsymbol{r})\rangle = \sum_{i=1}^{4} F_i(\boldsymbol{r})\, u_i(r), \tag{2-10}$$

for short. Where u_i are the periodic Bloch functions which for the rock salt lattice structure have L_6^- symmetry in the double-group notation for the bottom of the conduction band and L_6^+ symmetry for the top of the valence band. The arrow in Eq. 2-9 denotes the electron spin. Since the Hamiltonian has spherical symmetry it commutes with the total angular momentum operator $\hat{\boldsymbol{J}}$ and the parity operator $\widehat{\boldsymbol{\Pi}}$.

$$\hat{\boldsymbol{J}} = \hat{\boldsymbol{L}} + \frac{\hbar}{2}\begin{bmatrix} \boldsymbol{\sigma} & 0 \\ 0 & \boldsymbol{\sigma} \end{bmatrix} \tag{2-11}$$

$$\widehat{\boldsymbol{\Pi}} = \begin{bmatrix} -\hat{\boldsymbol{P}}\otimes\mathbf{1} & \mathbf{0} \\ \mathbf{0} & \hat{\boldsymbol{P}}\otimes\mathbf{1} \end{bmatrix} \tag{2-12}$$

Solving the eigenequation in spherical coordinates leads to two distinct eigenvectors

$$\mathcal{F}_{\pi,j,m}(\boldsymbol{r}) = \begin{bmatrix} if_l(r)\sqrt{\dfrac{l+m+1/2}{2l+1}}\,Y_l^{m-1/2} \\ if_l(r)\sqrt{\dfrac{l-m+1/2}{2l+1}}\,Y_l^{m+1/2} \\ f_{l+1}(r)\sqrt{\dfrac{l-m+3/2}{2l+3}}\,Y_{l+1}^{m-1/2} \\ -f_{l+1}(r)\sqrt{\dfrac{l+m+3/2}{2l+3}}\,Y_{l+1}^{m+1/2} \end{bmatrix} \tag{2-13}$$

For $\pi = (-1)^{l+1}$ and

$$\mathcal{F}_{\pi,j,m}(\boldsymbol{r}) = \begin{bmatrix} ig_{l+1}(r)\sqrt{\dfrac{l-m+3/2}{2l+3}}\,Y_{l+1}^{m-1/2} \\ -ig_{l+1}(r)\sqrt{\dfrac{l-m+3/2}{2l+3}}\,Y_{l+1}^{m+1/2} \\ g_l(r)\sqrt{\dfrac{l+m+1/2}{2l+1}}\,Y_l^{m-1/2} \\ -if_{l+1}(r)\sqrt{\dfrac{l-m+1/2}{2l+1}}\,Y_l^{m+1/2} \end{bmatrix} \quad (2\text{-}14)$$

For $\pi = (-1)^l$.

In Eq. 2-13 and 2-14 the Y_m^l are the spherical harmonics. The angular momentum quantum numbers are *l* (the angular momentum) and *m* (the z-projection of the total angular momentum). π represents the parity quantum number. The radial functions f_l and g_l are determined by substituting Eq. 2-13 and 2-14 into Eq. 2-7. This produces coupled second order equations of the form

$$\left\{\frac{E_g}{2} - E - \frac{\hbar^2}{2m^-}\left[\frac{d^2}{dr^2} + \frac{2}{r}\frac{d}{dr} - \frac{l(l+1)}{r^2}\right]\right\} f_l(r) - \frac{\hbar P}{m}\left\{\frac{d}{dr} + \frac{(l+2)}{r}\right\} f_{l+1}(r) = 0 \quad (2\text{-}15)$$

$$\frac{\hbar P}{m}\left\{\frac{d}{dr} - \frac{l}{r}\right\} f_l(r) - \left\{\frac{E_g}{2} + E - \frac{\hbar^2}{2m^+}\left[\frac{d^2}{dr^2} + \frac{2}{r}\frac{d}{dr} - \frac{(l+1)(l+2)}{r^2}\right]\right\} f_{l+1}(r) = 0 \quad (2\text{-}16)$$

$$\left\{\frac{E_g}{2} + E - \frac{\hbar^2}{2m^-}\left[\frac{d^2}{dr^2} + \frac{2}{r}\frac{d}{dr} - \frac{l(l+1)}{r^2}\right]\right\} g_l(r) - \frac{\hbar P}{m}\left\{\frac{d}{dr} + \frac{(l+2)}{r}\right\} g_{l+1}(r) = 0 \quad (2\text{-}17)$$

$$\frac{\hbar P}{m}\left\{\frac{d}{dr} - \frac{l}{r}\right\} g_l(r) - \left\{\frac{E_g}{2} - E - \frac{\hbar^2}{2m^-}\left[\frac{d^2}{dr^2} + \frac{2}{r}\frac{d}{dr} - \frac{(l+1)(l+2)}{r^2}\right]\right\} g_{l+1}(r) = 0. \quad (2\text{-}18)$$

Their general solutions are

$$f_l(r), g_l(r) = aj_l(kr) + bi_l(\lambda r) \tag{2-19}$$

$$f_{l+1}(r), g_{l+1}(r) = cj_{l+1}(kr) + di_{l+1}(\lambda r). \tag{2-20}$$

Here $j_l(kr)$ and $i_l(\lambda r)$ are the spherical Bessel functions and modified spherical Bessel functions respectively. The parameters a, b, c, d, k and λ are determined by the boundary conditions and the normalization of Eq. 2-15 to 2-18. With this the dispersion relations can be found.

$$\left[\frac{E_2}{2} - \frac{\hbar^2 k^2}{2m^-} - E(k)\right]\left[-\frac{E_2}{2} - \frac{\hbar^2 k^2}{2m^+} - E(k)\right] = \frac{\hbar^2}{m^2}P^2k^2 \tag{2-21}$$

$$\left[\frac{E_2}{2} - \frac{\hbar^2 k^2}{2m^-} - E(\lambda)\right]\left[-\frac{E_2}{2} + \frac{\hbar^2 k^2}{2m^+} - E(\lambda)\right] = -\frac{\hbar^2}{m^2}P^2\lambda^2 \tag{2-22}$$

The explicit form of the dispersion relations in the conduction band (+) and valence band (-) (Eq. 2-23) are found by inserting Eq. 2-19 and 2-20 into Eq. 2-15 to 2-20.

$$E_{\pm}(k) = \frac{1}{2}\left[\gamma k^2 \pm \sqrt{\left(E_g + \alpha k^2\right)^2 + \beta^2 k^2}\right], \tag{2-23}$$

where λ, β and γ are defined as:

$$\alpha = \frac{\hbar^2}{2}\left(\frac{1}{m^-} + \frac{1}{m^+}\right) \tag{2-24}$$

$$\beta = \frac{2\hbar^2 P}{m} \tag{2-25}$$

$$\gamma = \frac{\hbar^2}{2}\left(\frac{1}{m^-} - \frac{1}{m^+}\right) \tag{2-26}$$

Since $E(k)$ must be equal $E(\lambda)$ the relation between k and λ is

$$\lambda_{\pm}(k) = \sqrt{\frac{2\alpha E_g + \beta^2 + (\alpha^2 - \gamma^2)k^2 + 4\gamma E_{\pm}(k)}{\alpha^2 - \gamma^2}}. \tag{2-27}$$

By invoking infinite potential wells at the surface of a QD of radius a, the envelope functions (Eq. 2-13 and 2-14) have to go to zero at r = a.

$$\mathcal{F}(r = a) = 0. \tag{2-28}$$

With this Eq. 2-19 and 2-20 lead to Eq. 2-29 and 2-30

$$\varrho_{\pm}(k) j_{l+1}(ka) i_l(\lambda_{\pm} a) - \mu_{\pm}(k) j_l(ka) i_{l+1}(\lambda_{\pm} a) = 0, \tag{2-29}$$

$$\varrho_{\pm}(k) j_l(ka) i_{l+1}(\lambda_{\pm} a) + \mu_{\pm}(k) j_{l+1}(ka) i_l(\lambda_{\pm} a) = 0. \tag{2-30}$$

The functions $\varrho_{\pm}(k)$ and $\mu_{\pm}(k)$ are defined as

$$\varrho_{\pm}(k) = \frac{[E_g + (\alpha+\gamma)k^2 - 2E_{\pm}(k)]}{\beta\, k}, \tag{2-31}$$

$$\mu_{\pm}(k) = \frac{[E_g - (\alpha+\gamma)\lambda_{\pm}(k)^2 - 2E_{\pm}(k)]}{\beta\, \lambda_{\pm}(k)}. \tag{2-32}$$

Due to the quantum confinement, only discrete values for k and λ are permissible for a state with angular momentum *l*.

They can be found numerically by finding the roots of Eq.2-29 and 2-30 (see Fig. 2-5). The label + (-) throughout the text stands for states in the conduction (valence) band.

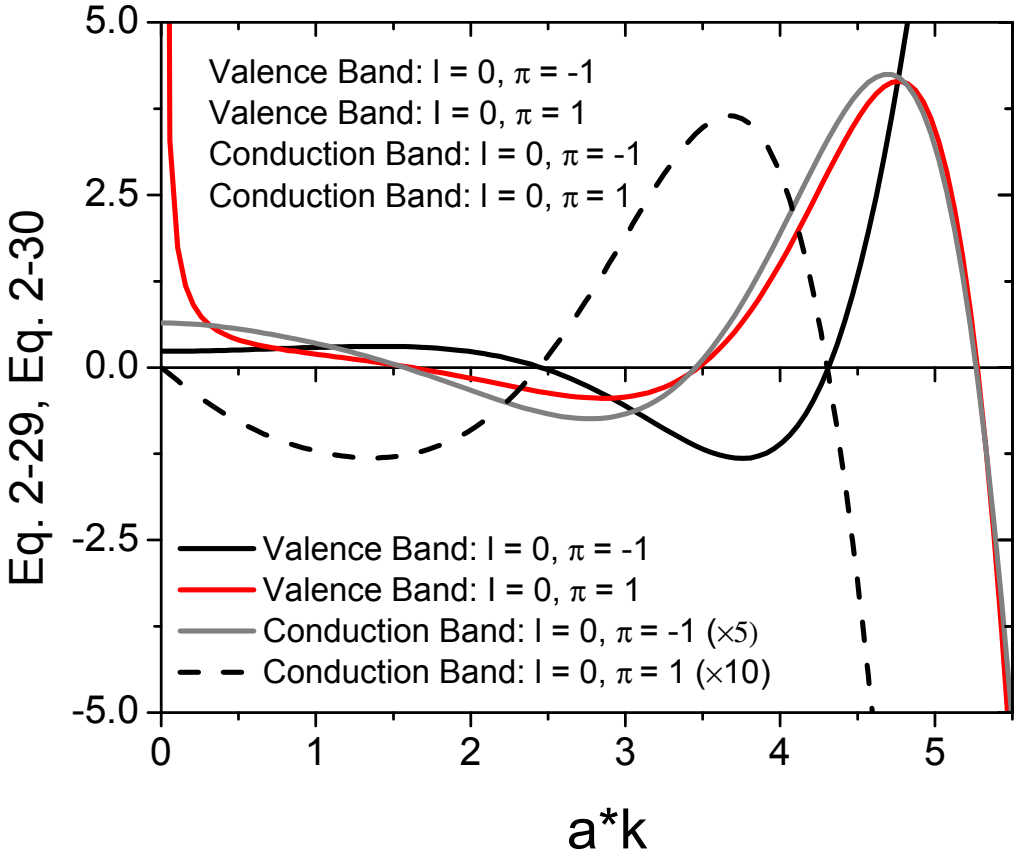

Figure 2-5: Plot of Eq. 2-29 and 2-30 over the dimensionless parameter a·k for $l = 0$. The roots of the functions corresponds to the wave vectors (k) allowed for the QCL in a QD of size a.

Substituting the discreet k values for the states identified by the quantum numbers l, π and n into the dispersion relation E(k) (Eq. 2-23), the energies of the QCL are found. Here l relates to the total angular momentum by $j = l + 1/2$, π is the parity and n denotes n^{th} zero in Fig. 2-5. Since in a spherically symmetric QD the QCL are degenerate in m (the total angular momentum in the z-direction), m is omitted in the notation. The energies of the QCL as a function of the QD radius are shown in Fig. 2-6 for electronic states in the valence band with negative energies and for electronic states in the conduction band with positive energies. Furthermore, since the quantum

number m can take on values in the range $-l \leq m \leq +l$ (l is the letter not the number 1), the bands in the rock salt lattice have 4 equivalent valleys and each level can be occupied by 2 electors (spin up and dowen) the QCL have $2l$+1×4×2 degeneracy i. e. the S levels with $l = 0$ are 8 fold degenerate the P levels have 24 fold degeneracy et cetea.

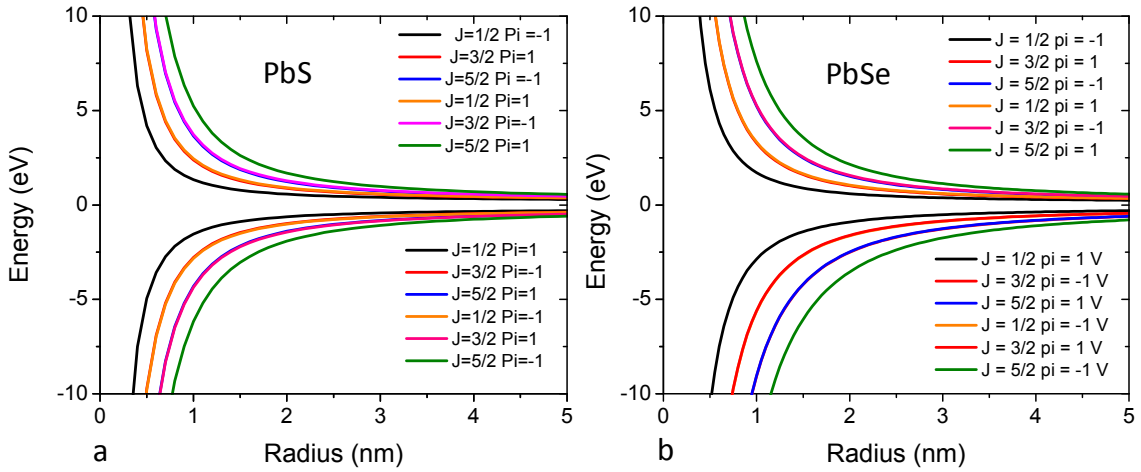

Figure 2-6: Energies of the first six QCL's for PbS and PbSe in the conduction and valence band plotted as a function of the QD radius.

Apart from a normalization constant, the radial functions $f_l(r), f_{l+1}(r), g_l(r), g_{l+1}(r)$ in Eq. 2-13 and 2-14 have the form

$$f_l(r) = j_l(kr) - \frac{j_l(ka)}{i_l(\lambda a)} i_l(\lambda r), \tag{2-33}$$

$$f_{l+1}(r) = \varrho(k)\left[j_{l+1}(kr) - \frac{j_{l+1}(ka)}{i_{l+1}(\lambda a)} i_{l+1}(\lambda r)\right], \tag{2-34}$$

$$g_{l+1}(r) = j_{l+1}(kr) - \frac{j_{l+1}(ka)}{i_{l+1}(\lambda a)} i_{l+1}(\lambda r), \tag{2-35}$$

$$g_l(r) = -\varrho(k)\left[j_{l+1}(kr) - \frac{j_l(ka)}{i_l(\lambda a)} i_l(\lambda r)\right]. \tag{2-36}$$

With this information the electronic wavefunctions $\left|\psi_{j,\pi,n}^{c,v}\right\rangle$ in the quantum confined system are known and the strength of the dipole transitions can be calculated from first order perturbation theory i. e. Fermi's golden rule [20].

$$M_{v,c} = \frac{2\pi}{\hbar}\sum_{v,c}\left|M_{v,c}\right|^2\delta(E_c - E_v - 2\hbar\omega), \tag{2-37}$$

$$M_{c,v} = \left\langle\psi_{j,\pi,n}^{c}\middle|\mathbf{e}\cdot\mathbf{p}\middle|\psi_{j,\pi,n}^{v}\right\rangle. \tag{2-38}$$

In the matrix element (Eq. 2-38) **e** is the polarization direction of the electric field and **p** is the momentum operator. This approximation is derived for a CW excitation. However, since the time of an electronic transition accrues on timescales of sub fs the 140fs duration of a typical experiment satisfy the condition of constant field amplitude over the duration of the electronic transition [21].

Substituting Eq. 2-10 for the initial and final state in Eq. 2-38 we arrive at

$$M_{c,v} = \left|\int\left(\sum_{i=1}^{4}F_i^c u_i\right)^{\dagger}(\mathbf{e}\cdot\mathbf{p})\left(\sum_{j=1}^{4}F_j^v u_j\right)d(r)\right|^2. \tag{2-39}$$

If we now use the fact that the envelope functions (F) have slowly varying amplitudes over the unit cell of the semiconductor, M can be expressed as

$$\begin{aligned} M = \Bigg|\sum_{i,j=1}^{4}\Bigg\{&\Omega\sum_{k\ cell}[F_i^c(\boldsymbol{r}_k)]^*(\mathbf{e}\cdot\mathbf{p})F_j^v(\boldsymbol{r}_k)\times\frac{1}{\Omega}\int_{cell}d\boldsymbol{r}u_i^{\dagger}(\boldsymbol{r})u_j(\boldsymbol{r}) \\ &+\Omega\sum_{k\ cell}[F_i^c(\boldsymbol{r}_k)]^*F_j^v(\boldsymbol{r}_k) \\ &\times\frac{1}{\Omega}\int_{cell}d\boldsymbol{r}u_i^{\dagger}(\boldsymbol{r})(\mathbf{e}\cdot\mathbf{p})u_j(\boldsymbol{r})\Bigg\}\Bigg|^2, \end{aligned} \tag{2-40}$$

here Ω is the volume of the unit cell. With the properties [19].

$$\frac{1}{\Omega}\int_{cell} d\boldsymbol{r} u_i^{\dagger}(\boldsymbol{r}) u_j(\boldsymbol{r}) = \delta_{i,j},$$

$$\frac{1}{\Omega}\int_{cell} d\boldsymbol{r} u_1^{\dagger}(\boldsymbol{r}) \boldsymbol{p} u_3(\boldsymbol{r}) = \frac{1}{\Omega}\int_{cell} d\boldsymbol{r} u_3^{\dagger}(\boldsymbol{r}) \boldsymbol{p} u_1(\boldsymbol{r}) = P_l \hat{z}, \tag{2-41}$$

$$\frac{1}{\Omega}\int_{cell} d\boldsymbol{r} u_2^{\dagger}(\boldsymbol{r}) \boldsymbol{p} u_4(\boldsymbol{r}) = \frac{1}{\Omega}\int_{cell} d\boldsymbol{r} u_4^{\dagger}(\boldsymbol{r}) \boldsymbol{p} u_2(\boldsymbol{r}) = -P_l \hat{z},$$

Equation 2-40 simplifies to

$$\begin{aligned} M_{c,v} = \Bigg| \int \sum_{i=1}^{4} & F_i^c(r)^* (\mathbf{e}\cdot\mathbf{p}) F_i^v(r) \\ & + (\mathbf{e}\cdot\hat{z})\, P_l \{F_1^c(r)^* F_3^v(r) \\ & + F_3^c(r)^* F_1^v(r) - F_2^c(r)^* F_4^v(r) - F_4^c(r)^* F_2^v(r)\} dr \Bigg|^2. \end{aligned} \tag{2-42}$$

The interaction Hamiltonian **e·p** connecting the wave functions is

$$\mathbf{e}\cdot\mathbf{p} = \left(e_x, e_y, e_z\right)\cdot(-i\hbar\nabla). \tag{2-43}$$

In spherical coordinates this can be expressed in terms of the orbital angular momentum operator L_z and its leader operators L_+ and L_-

$$\begin{aligned} \mathbf{e}\cdot\mathbf{p} = -i\hbar \Bigg\{ & \left[\cos\theta \frac{d}{dr} + \frac{\sin\theta}{2r}\left(e^{i\varphi}L_- - e^{-i\varphi}L_+\right)\right] e_z \\ & + \left[\sin\theta\, e^{-i\varphi}\frac{d}{dr} + \frac{1}{r}\left(\sin\theta\, e^{-i\varphi}L_z - \cos\theta\, L_-\right)\right]\frac{e_x + ie_y}{2} \\ & + \left[\sin\theta\, e^{i\varphi}\frac{d}{dr} + \frac{1}{r}\left(-\sin\theta\, e^{i\varphi}\, L_z + \cos\theta\, L_+\right)\right]\frac{e_x - ie_y}{2} \Bigg\}, \end{aligned} \tag{2-44}$$

where

$$\mathbf{L_z} = -i\,\frac{\partial}{\partial\phi}, \tag{2-45}$$

$$\mathbf{L_\pm} = \boldsymbol{L_x} \pm i\boldsymbol{L_y} = \pm e^{\pm i\phi}\left[\frac{\partial}{\partial\theta} \pm \mathrm{i}\,\cot\theta\,\frac{\partial}{\partial\phi}\right]. \tag{2-46}$$

The action of $L_\pm$ on the spherical harmonics Y_l^m of the QCL is

$$\mathbf{L_\pm} Y_l^m = \hbar\sqrt{l(l+1) - m(m\pm 1)}\; Y_l^{m\pm 1}. \tag{2-47}$$

If the operator **e**·**p** (Eq. 2-44) acts on the the wavefunctions Eq. 2-13 and Eq. 2-14 it becomes apparent that the one photon selection rules are

$$\Delta j = 0, \pm 1, \qquad \Delta m = 0, \pm 1, \qquad \pi_c \pi_v = -1. \tag{2-48}$$

The same interaction Hamiltonian (Eq. 2-43) and wavefunctions $|\psi(\boldsymbol{r})\rangle$ (Eq. 2-10) can be used to calculate general two-photon transitions in a second-order time dependent perturbation approach [20, 22].

$$M_{v,c} = {}^1\!/_2 \sum_i \frac{\langle\psi_c|e\cdot p|\psi_i\rangle\langle\psi_i|e\cdot p|\psi_v\rangle}{E_i - E_v - \hbar\omega_1} + \frac{\langle\psi_c|e\cdot p|\psi_i\rangle\langle\psi_i|e\cdot p|\psi_v\rangle}{E_i - E_v - \hbar\omega_2} \tag{2-49}$$

This formula simplifies to

$$M_{v,c} = \sum_i \frac{\langle\psi_c|e\cdot p|\psi_i\rangle\langle\psi_i|e\cdot p|\psi_v\rangle}{E_i - E_v - \hbar\omega} \tag{2-50}$$

for the degenerate case.

The set of selection rules for the two-photon case are

$$\Delta j = 0, \pm 1, \pm 2 \;\; \Delta m = 0, \pm 1, \pm 2 \;\; \pi_c \pi_c = 1 \tag{2-51}$$

With the selection rules (2-48 and 2-51) and the dispersion relations (2-23) the allowed one- and two-photon transition energies as a function of QD size can be calculated as is shown in Fig. 2-7.

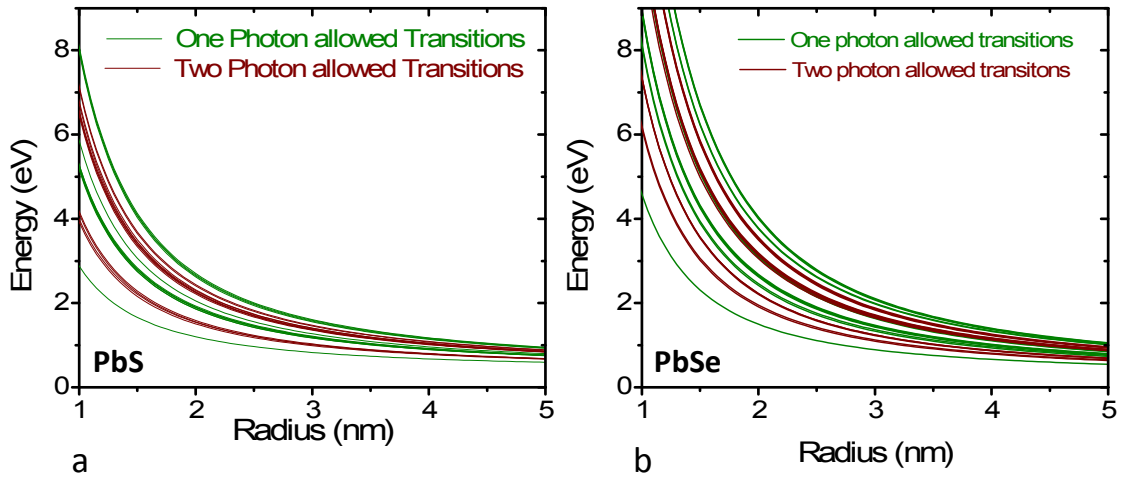

Figure 2-7: One- and two-photon allowed transitions energies as a function of the QD radius calculated for PbS (a) and PbSe (b)

The calculations of the transition strengths of one-photon absorption and the degenerate and nondegenerate two-photon absorption between QCLs from the $\boldsymbol{k \cdot p}$ model requires solutions of the integrals in Eq. 2-38, 2-49 and 2-50 respectively. This is implemented in a Mathcad code (see appendix). Two different versions of the program are used to calculate the oscillator strength of a specific number of transitions for the degenerate and the nondegenerate 2PA case. The only input parameters required to calculate the optical transitions are the material (PbS or PbSe), the radius of the QD, the range of transitions to calculate and how many intermediate QCL are to be included in the calculation of the two-photon transitions. The number of intermediate QCL needed in the calculation depends on the particular transition, but for transitions with quantum numbers $l \leq 3$ and $n \leq 2$ intermediate stats with quantum numbers l, $n \leq 4$ are sufficient to converge the oscillator strength to about 1% accuracy. Alternatively a range for QD radii and a step size for

the radius can be chosen to calculate the trend of the oscillator strength with changing quantum confinement at a significantly higher computational cost. A detailed instruction of how to operate the two versions is given in the appendix.

The calculated transition strength is shown in Fig. 2-8 and 2-9 for one-photon and degenerate two-photon absorption for a 3nm PbS and PbSe QD. Clearly identifiable are energy regions with relatively dense transition lines separated by regions of no transitions. This is a consequence of the aforementioned near mirror symmetry of the QCLs in the conduction and valence bands and is more pronounced in PbS than in PbSe.

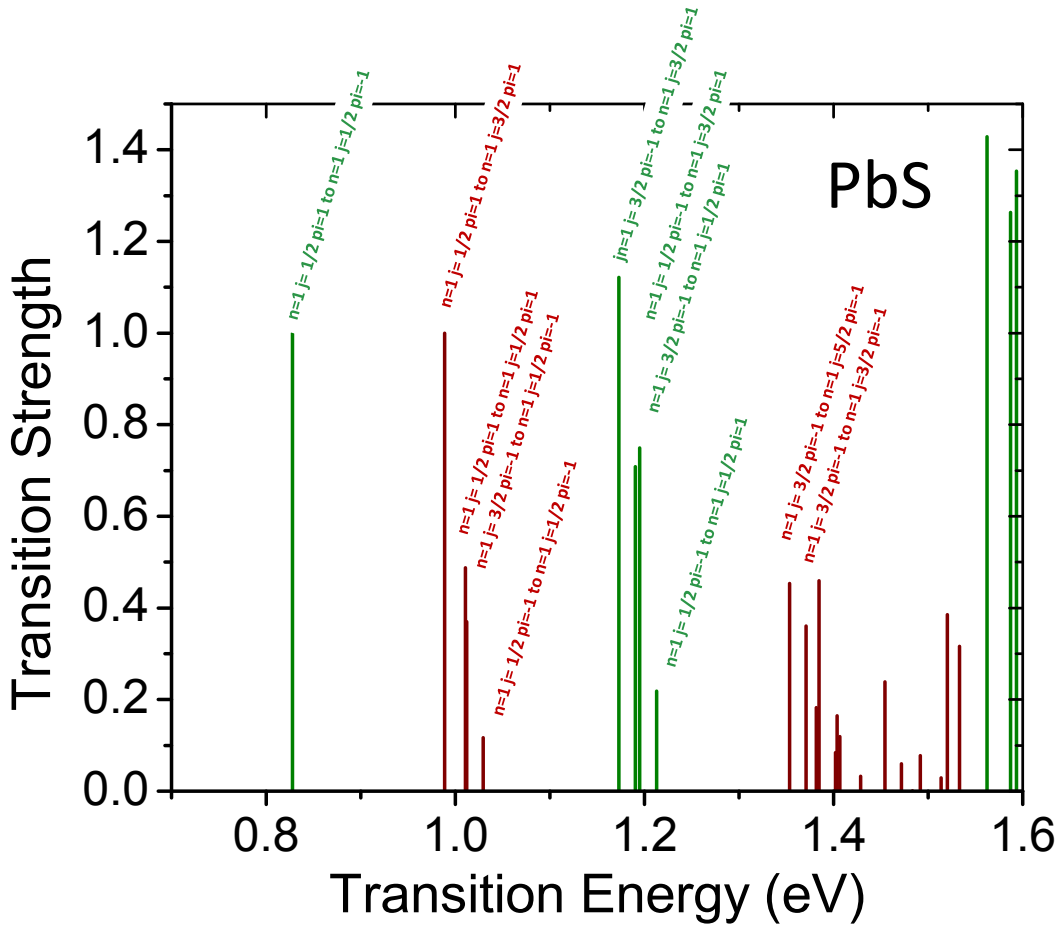

Figure 2-8: One- and two-photon transitions as calculated by the ***k·p*** model for a 3.0nm PbS QD. One-photon transitions are indicated as green vertical lines, two-photon transitions are represented as red lines. The height of the lines represents the relative transition strength.

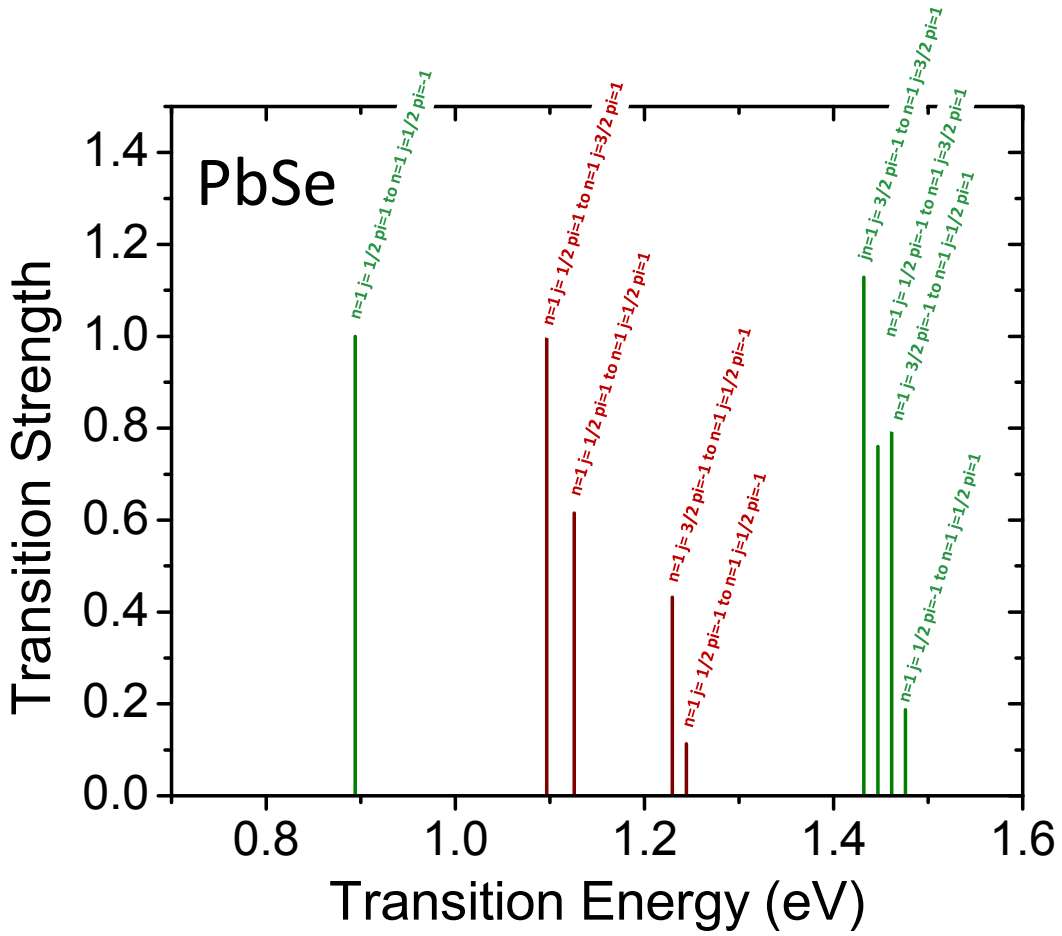

Figure 2-9: One- and two-photon transitions as calculated by the ***k·p*** model for a 3.0nm PbSe QD. One-photon transitions are indicated as green vertical lines, two-photon transitions are represented as red lines. The height of the lines represents the relative transition strength.

CHAPTER 3:
EXPERIMENTAL TECHNIQUES AND LIGHT SOURCES

The high electric fields typically required for nonlinear optical effects can only be provided by laser systems. Of particular interest are ultrashort pulsed laser sources since the high irradiances (W/cm^2) can be achieved with relatively small pulse energies. The wavelength tunability for nonlinear spectroscopy can be achieved by means of optical parametric generation/amplification or white light continuum generation (WLC).

3.1. *Laser System*

To achieve the required high irradiance a regeneratively-amplified, femtosecond Ti:Sapphire laser system manufactured by Clark-MXR, Inc is used. The Ti:Sapphire laser cavity amplifier is seeded from a diode pumped mode-locked fiber laser operating at 27MHz. In order to prevent damage due to high irradiance to the Ti:Sapphire crystal, the seed pulse is temporally stretched before amplification and later re-compressed. This is called "Chirped Pulse Amplification" (CPA) and was first implemented by Strickland and Mourou in 1985 [23]. Single pulses from the seed laser are selected at a rate of 1kHz and directed into the amplifier by means of an electro-optical switch. The selected pulse than makes several passes through the amplifier until the maximum amount of energy is extracted from the Ti:Sapphire crystal. The Ti:Sapphire amplifier is pumped synchronously with the seed from a Q-switched frequency doubled Nd:YAG laser. When the seed has extracted the maximum energy from the Ti:Sapphire crystal the pulse is directed out of the cavity into the compressor via the electro optical switch and the optical insulator. The final result are 1.7mJ 140fs pulses at 775nm with a repetition rate of 1kHz.

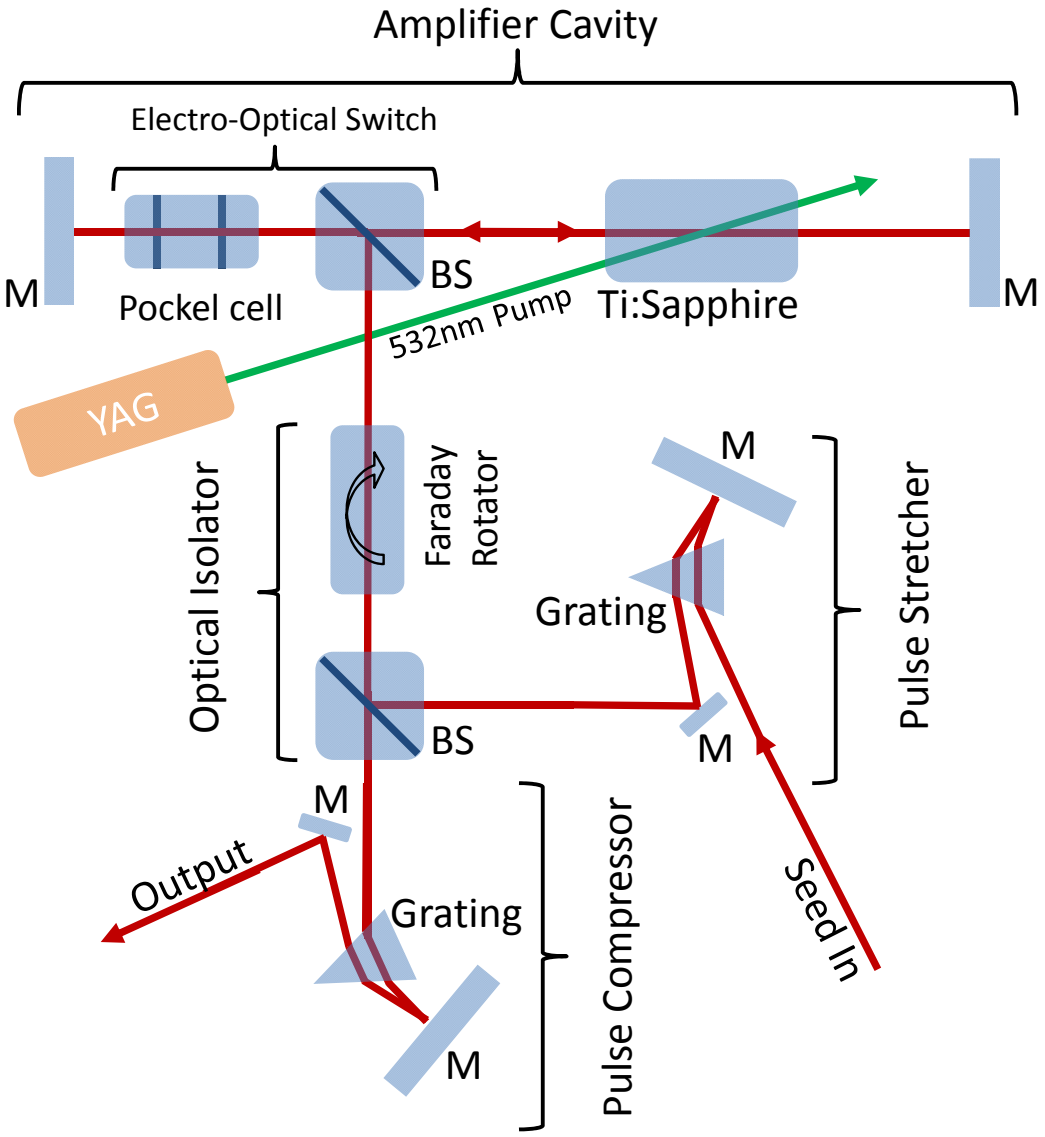

Figure 3-1: Regenerative amplifier. M-mirror; BS-beamsplitter.

3.2. *Optical parametric Generation*

Optical parametric generation followed by parametric amplification and if necessary further parametric processes is used to tune the output of the system pumped by the 775nm wavelength of the laser. The system used to generate pulses of the desired color is a

commercially available Traveling-wave Optical Parametric Amplifier of Superfluorescence (TOPAS) manufactured by Light Conversion. While the details may vary in different models, the basic principle of operation remains the same and will be outlined in the following:

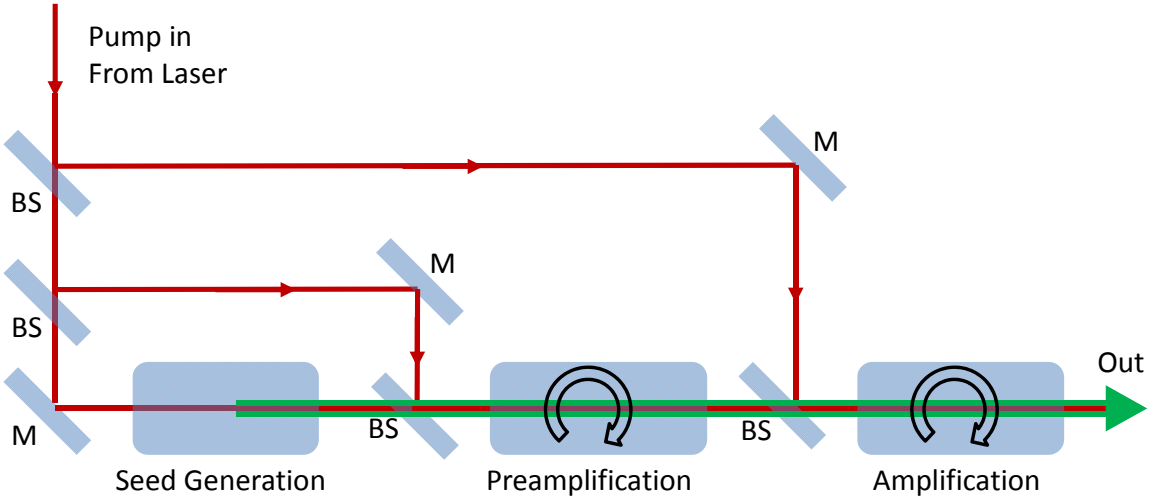

Figure 3-2: TOPAS; Principe of operation. M-mirror; BS-beam-splitter

The beam of the Ti:Sapphire laser is divided by means of beam splitters (see Fig. 3-2). One of the beams is used to generate a broad band superfluorescence seed inside a BBO (Barium Borate-β-BaB2O4crystal). In some of the newer setups the initial seed is produced by the inherently more stable supercontinuum or WLC generation described in section 3.3 [24]. A specific wavelength of the seed is selectively amplified by overlapping it with a second pump pulse and adjusting the angle of the BBO crystal in order to achieve phase matching [25]. The amplification process is repeated several times to achieve the required pulse energy. Further extension of the tunability range can be achieved by second and fourth harmonic generation of the signal or idler and by either sum-frequency of the idler and the pump or by difference-frequency generation of the signal and idler. The total tunability range achieved with the fs light source is from 270nm to 12µm (see Fig. 3-3).

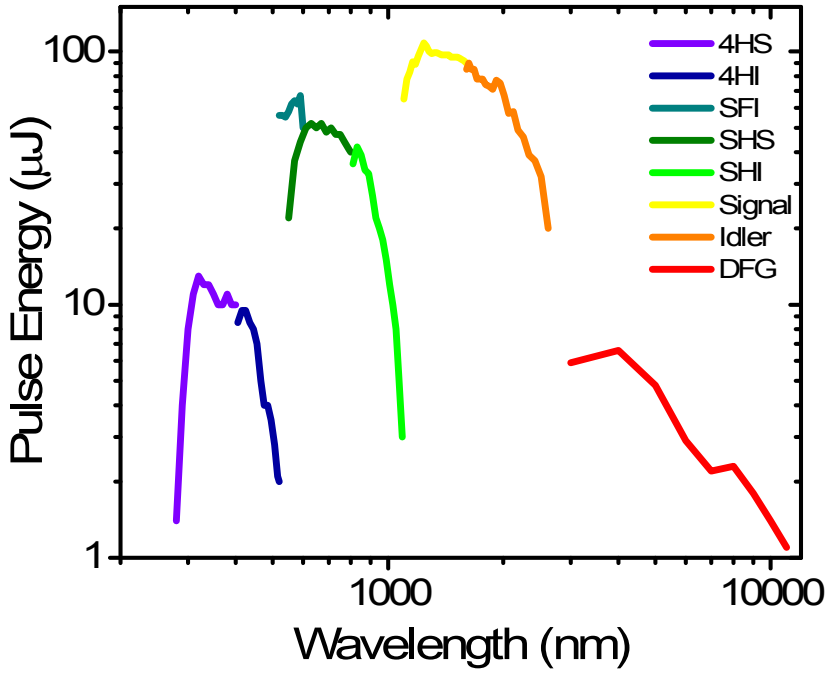

Figure 3-3: TOPAS tuning range. The modes of operation starting at short wavelength to long wavelength are: Fourth harmonic of the signal (4HS), Fourth harmonic of the idler (4HI), Sum frequency of the 775 laser line plus idler (SFI), second harmonic of the signal (SHS), second harmonic of idler (SHI), signal, idler and difference frequency generation between signal and idler (DFG).

3.3. ***Supercontinuum generation***

The technique mentioned above is capable of producing high energy pulses over a vast wavelength range, but it has certain challenges. The main drawback is that in order to switch between the different modes of generation e.g. signal to idler or second harmonic generation the beam path as well as the spatial and temporal profile is significantly altered and realignment of the experimental setup is required. Even the slight angle change of the BBO crystal, necessary to achieve phase-matching for a new wavelength within the same mode of operation changes the propagation of the beam enough to make manual readjustment necessary.

A relatively simple way to generate ultrashort broad-band pulses is the previously mentioned supercontinuum generation or white-light continuum generation (WLC). The rapid change in irradiance (derivative of the magnitude of the electric field, see Eg. 3-1) of the fs pulses introduces an equally fast change of the refractive index in a nonlinear medium. This fast change of the refractive index rearranges the phase of the pulse itself and introduces new frequency components. This is called Self-Phase Modulation (SPM) and was first studied by Brewer, Shimizu and Cheung in the late 60is [26-28]. The change in frequency over the duration of the pulse is given in Eq. 3-1 [29].

$$\delta\omega(t) = -\frac{\partial\varphi_{NL}}{\partial t} \propto -\frac{\partial}{\partial t}|E(t)|^2. \qquad (3\text{-}1)$$

While details of the frequency shift depend on the nonlinear response of the medium and the temporal shape of the pulse, a couple of general statements can be made. First, since the frequency change is proportional to the derivative of the pulse irradiance (amplitude of E^2) SPM and WLC generation work best for short pulses (sub ps) and second the pulse will be chirped with the low frequency components leading the high frequency components for $n_2>0$. Schematically this is shown in Fig. 3-4 where the temporal irradiance profile of a Gaussian beam is shown in part (a). If the nonlinear refraction is proportional to the irradiance (and positive), as in an instantaneous process, than the change in refractive index as well as the phase change will be directly proportional to the irradiance (also shown in a). The derivative of the change in phase according to Eq. 3-1 is shown in part b of Fig. 3-4. For positive n_2 the instantaneous changes is towards lower frequencies at earlier times and higher frequencies at later times and the pulse is therefore chirped. For negative n_2 the frequency shift will be reversed i. e. the leading part of the

pulse will be shifted toward the blue. The chirp is typically further increased while traveling thru the dispersive media in which the WLC is generated.

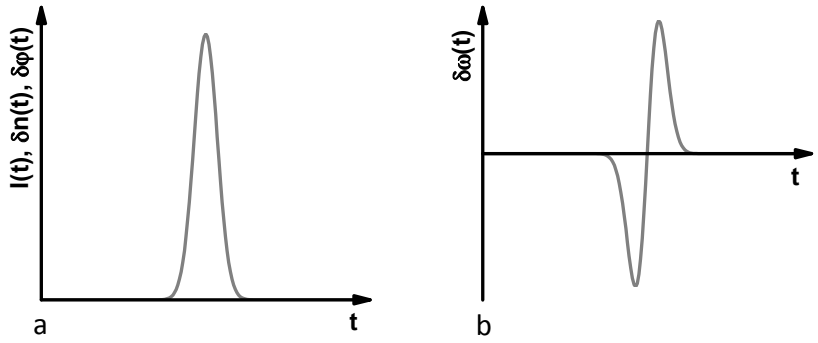

Figure 3-4: (a) Temporal irradiance profile of incident pulse together with instantaneous change of the refractive index and phase (for $n_2>0$). (b) Instantaneous change in frequency.

If SPM is due to an instantaneous change in n like for an electronic $\chi^{(3)}$ process the broadening will be symmetric around ω_0 (see Fig. 3-4) but will be waited towards one side of the frequency spectrum for a change in n which does not follow the intensity profile of the pulse. In most practical circumstances the pulse will be predominantly broadened on the blue side. A discussion of the various physical mechanisms responsible for SPM can be found in ref [30]. By this method an initially transform limited fs pulse with a bandwidth of ~10 nm can be significantly broadened in the spectral domain to several hundred nm.

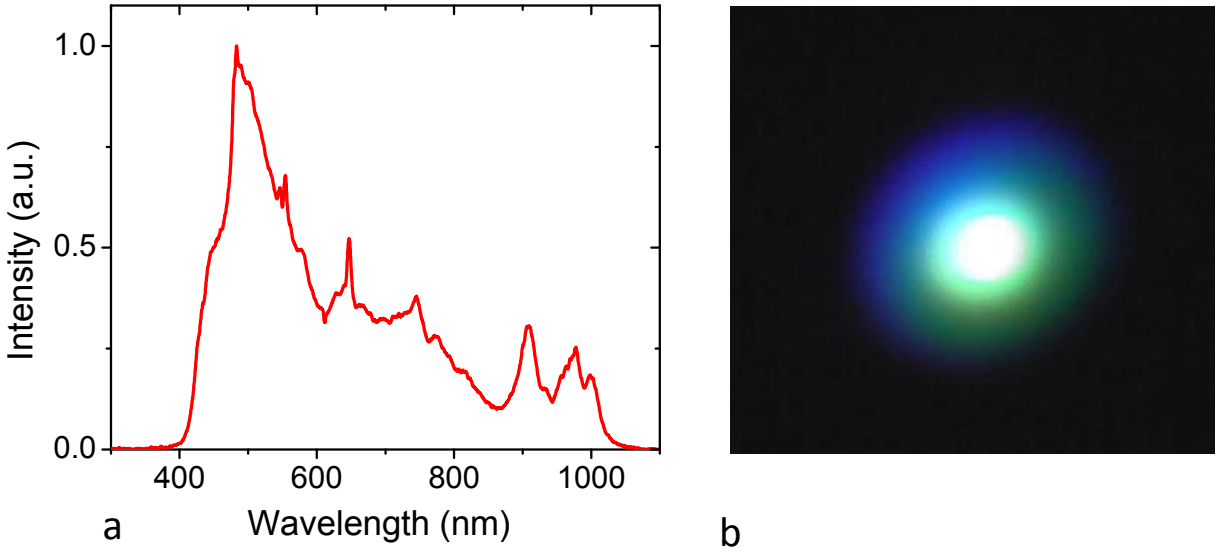

Figure 3-5: (a) White-light continuum spectrum in the VIS and near IR region. The pump wavelength is 1400 nm, outside the detector responsivity range. (b) CCD image of WLC.

In our laboratory we generate a WLC by focusing the 1300nm light from a TOPAS onto a Calcium fluoride CaF_2 window. The window rotates slowly (one rotation per hour) to avoid thermal effects which can damage the crystal. This way a WLC from 400nm to 1600nm is generated (see Fig. 3-5). Spectral regions are selected by means of narrow band interference filters. and a rapidly tunable ultrafast light source is realized [31].

3.4. ***Z-Scan Technique***

Z-scan is a powerful technique used to study nonlinear absorption and refraction. The basic idea is that the irradiance of a focused Gaussian beam will change along its propagation direction

which we will assume to be in the z direction. Any nonlinear optical effect which by definition depends on the irradiance will therefore depend on the position of the sample along the Z axis hence the term "Z-scan".

The so called open aperture Z-scan (Illustrated in Fig. 3-6) measures nonlinear absorption i.e. in case of a pure two-photon absorber the imaginary part of the third order susceptibility ($\mathrm{Im}(\chi^{(3)})$) which changes the total amount of energy transmitted through the sample. This is in contrast to the closed aperture Z-scan which measures optically induced phase changes i. e. the real part of the third order nonlinearity ($\mathrm{Re}(\chi^{(3)})$). Assuming that the sample is a two-photon absorber, it is easy to see that at focus, where the irradiance is highest, the energy transmittance is at a minimum, while in the wings where the irradiance is low the energy transmitted is high and limited by the linear properties of the sample. Typically the open aperture Z-scan trace, as shown on the right side of Fig. 3-6, is fitted numerically by solving the differential equation appropriate for the nonlinear process i. g. two-photon absorption (2PA), excited state absorption (ESA) or reverse saturable absorption (RSA).

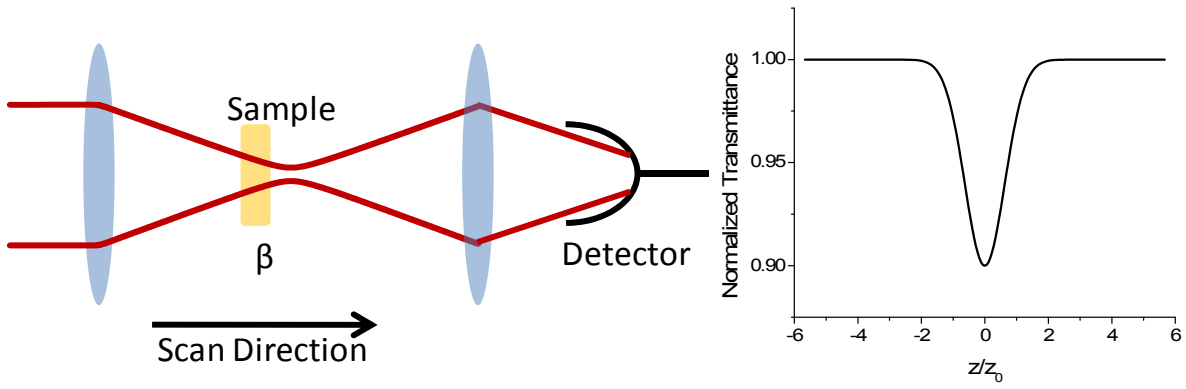

Figure 3-6: Schematic of open aperture Z-scan

In the closed aperture configuration an aperture is placed in the far field between the focal point and the detector. In this configuration the nonlinear refraction is measured. The method works, because the beam irradiance not only varies along the Z-direction, but also along the radius in a finite beam i.e. in a Gaussian beam. Therefore, in a nonlinear refracting medium the phase of the electric field is most strongly altered close to the beams axis and an index gradient lens is formed. The effect is observable only with the sample close to the focal point where again the irradiance is strongest. For positive nonlinear refraction ($n_2 > 0$) the phase is retarded in the center causing the beam to self-focus. Negative nonlinearities ($n_2 < 0$) tend to defocus the beam. As a result, the beam phase curvature is dependent on the sample position along the Z axis and is either concentrated or spread in the far field which changes the transmittance through the aperture. In most experimental settings the sample can be kept thin compared to the Rayleigh range of the focusing geometry. Under these conditions and under the condition that the induced phase distortion does not result in beam shape changes within the sample we are in the so-called thin sample approximation. This external self-action regime allows solving for the transmittance through the aperture by Gaussian decomposition as well as numerically in a full beam propagation model. A closed aperture Z-scan is illustrated in Fig. 3-7. The Z-scan technique is self-calibrating in the sense that all necessary parameters other than the pulse energy are geometrical and as such are easily measured: for example the sample thickness and aperture diameter.

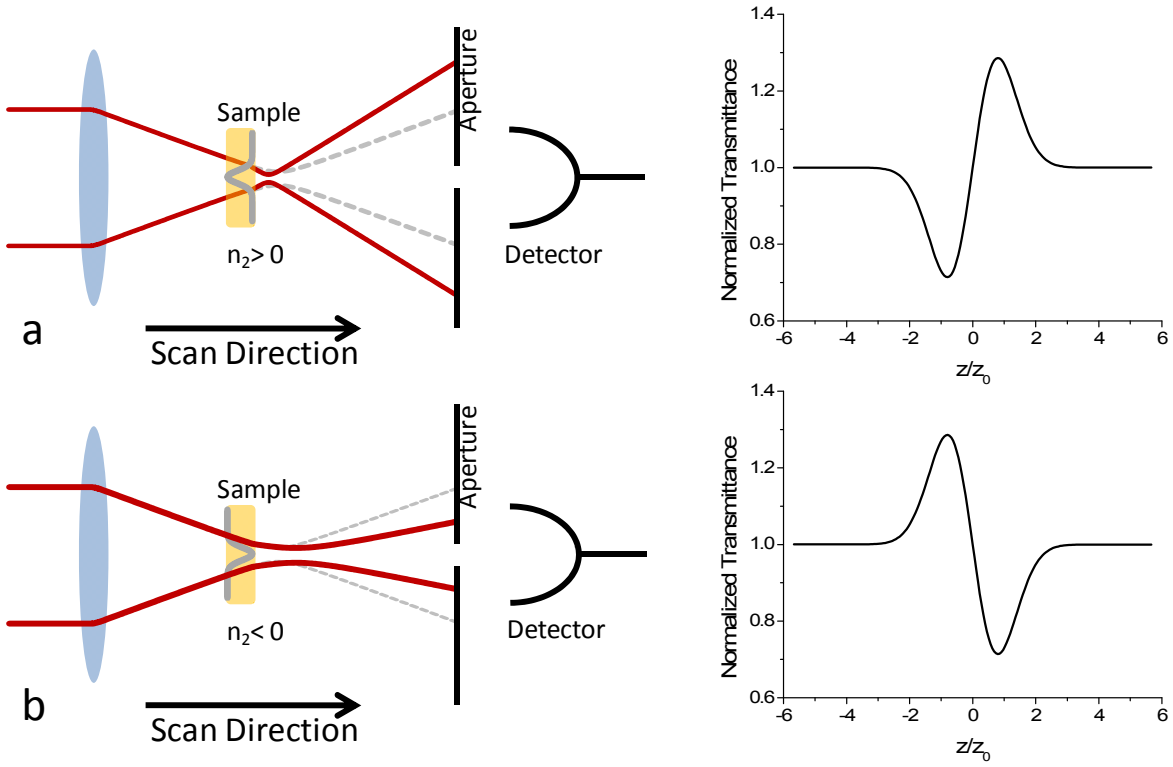

Figure 3-7: Closed aperture (CA) Z-scan for a thin sample. The trace of a beam through a nonlinear refracting sample situated just before focus is indicated by red lines. Also shown is the trace of the beam as it would propagate if the sample where not present or moved far away from focus (gray/dashed lines). Typical closed aperture Z-scan traces are shown on the right side for $n_2 > 0$ in (a) and $n_2 < 0$ in (b).

As a single beam technique Z-scan has the advantage of relatively simple alignment compared to other techniques used to study optical nonlinearities such as four-wave mixing or pump-probe. Z-scan is capable of measuring nonlinear absorption in the presence of linear absorption and nonlinear refraction in the presence of linear and nonlinear absorption. The later is achieved by fitting both open and then closed aperture data or by simply dividing the closed aperture signal by the simultaneously recorded open aperture signal and treating as if there were no nonlinear absorption. It may be counter intuitive, but the phase sensitivity of the closed aperture Z-scan is

actually as good as any interferometic method. Phase distortions of less than λ/300 [32] or even λ/10000 with some trickery [33] can be detected.

For the Z-scan experiments in our laboratories we use large area Si and Ge photodiodes for wavelengths up to 1.7μm. Thorlabs PDA30G PbS and PDA20H PbSe detectors are used for wavelength to 2.9μm and 4.8μm. For even longer wavelength HgCdTe liquid nitrogen cooled detectors are used (λ_{max} ~15μm). In combination with the widely tunable light sources at our disposal the nonlinear absorption and refraction can be investigated from 270nm to 12μm with fs pulse. Similarly wide tunable light sources for ps and ns pulses are available in our group, but where not used in this work.

3.5. ***Two-photon excited Fluorescence Technique***

Two-photon fluorescence, 2PF, relies on the validity of Kasha's Rule [34] which states than no matter how high one excites a system above the first excited state, all carriers will relax back to the first excited state and fluoresce from there with a quantum yield independent of the excitation. Conversely, the number of emitted photons will be directly proportional to the number of absorbed photons. Therefore, by scanning the excitation wavelength and measuring the fluorescence intensity, the absorption of samples with reasonable high quantum yields can be deduced. The discussion above is independent of the absorption process and so if the excited state is populated by 2PA the resulting fluorescence is a measure of the two-photon absorption coefficient. We have found very few exceptions to this rule in our studies and due to the fast

intra band relaxation in QDs (see Chapter 5.1) this method should work well for the samples studied in this work.

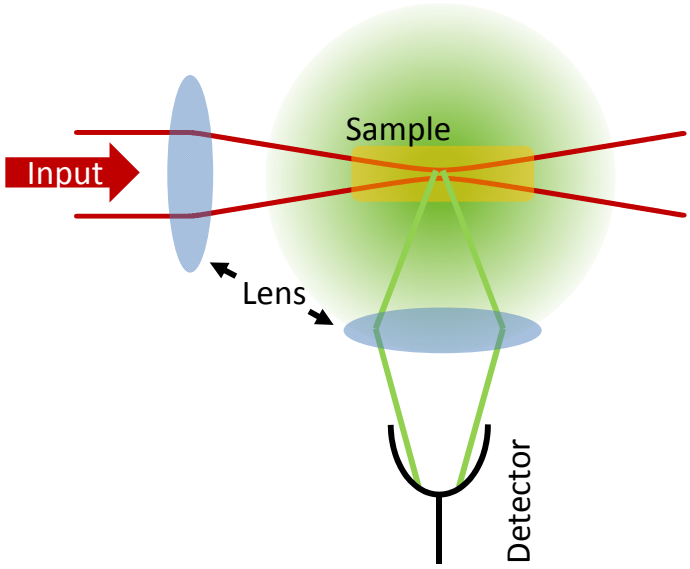

Figure 3-8: Schematic of 2PF setup.

Unlike than the Z-scan technique, 1PF and 2PF are relative measurements and as such need to be calibrated against a known reference or some other technique like Z-scan. Advantages of the 2PF technique are its good sensitivity, it's insensitivity to excited-state absorption, ESA (at least in principle), and ease of alignment[35].

It is currently the most rapid technique to measure nonlinear absorption at our disposal, but we are limited to samples which fluoresce at wavelengths shorter than 800nm by our current detection system (Type R928P photomultiplier tube).

3.6. *Pump-Probe Technique*

The pump probe technique, sometimes also called transient absorption spectroscopy (TA) allows time resolved spectroscopy with temporal resolution only limited by the pulse duration of the light [36, 37] [1,2]. A synchronized pump and a probe beam are generated from the same primary pump source. In our case the primary pump is the regeneratively-amplified, Ti:Sapphire laser described in Chapter 3.1 which produces 140 fs pulses. The laser pumps two optical parametric generators (TOPAS 1 and 2 in Fig. 3-9). The output of TOPAS 1 is used as a pump pulse and TOPAS 2 is used to generate a WLC (see Chapter 3.3). By using a narrow band pass filters a small portion of the WLC spectrum is selected and used as a probe. The relative travel time of the pump and the probe can be altered by changing the relative path length by moving a retroreflector mounted on a linear translation stage.

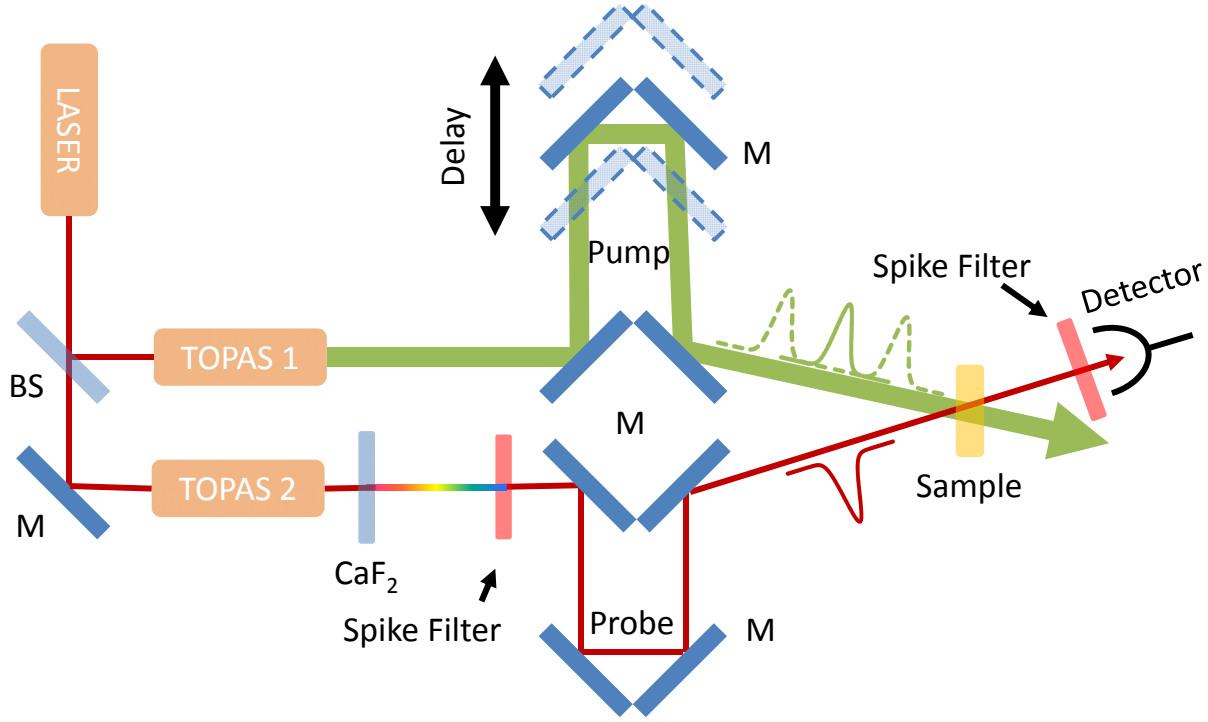

Figure 3-9: Pump-Probe Setup

The energy available for the probe beam depends on the shape of the WLC spectra and the transmission of the narrow band spike filter. The probe irradiance must be kept very weak so that any nonlinear effect created by the probe itself can be neglected and the experiment can be viewed as if the material under investigation is changed by the pump alone and then linearly probed by the weak probe beam. It is in this sense that the energy of the probe is not important for the experiment as long as the irradiance of the probe is much smaller than the irradiance of the pump ($I_{Probe} << I_{Pump}$). In order to ensure good spatial overlap of the pump and the probe while changing the delay, the pump beam waist is set several times larger than the tightly focused probe beam. This has the added advantage that the pump irradiance of the typically Gaussian beam can now be considered constant, as far as the interaction of the probe is concerned, since only the center part is probed. Typically, since the probe beam waist is smaller than the pump, the energy of the pump is 10^3 times stronger than the probe in order to ensure the afore mentioned condition of high pump and low probe irradiance. The pump and the probe beam meet at a small angle of typically 10°. This is necessary to separate the about three orders of magnitude stronger pump from the weak probe on the detector. In addition the same narrow band filter type used to select the spectral region of the WLC is used in front of the detector to further suppress any scattered light from the pump. In this manner the effect of a strong pump beam impressed upon a sample can be measured. If the effect is a quasi-instantaneous like nondegenerate 2PA the resulting change in the transmission of the probe is the cross-correlation of the two pulses. Longer lived effects like ESA are identified by an exponential change of the probe transmission with increasing delay (see Fig. 3-10).

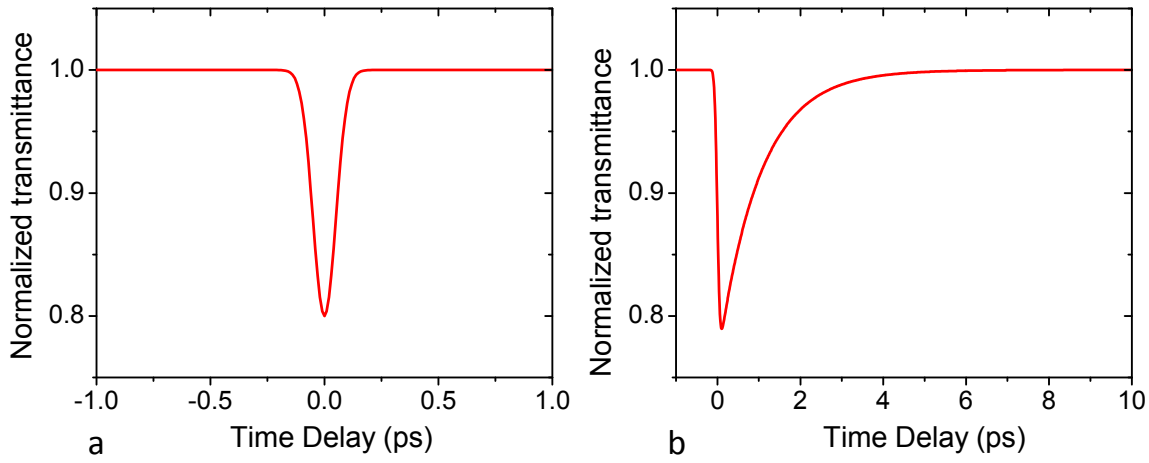

Figure 3-10: Typical TA trace for an instantaneous (a) and long lived NLO response (b) i. g. 2PA and ESA respectively.

CHAPTER 4:
TWO PHOTON ABSORBTION IN LEAD SALT QDS

PbS and PbSe belong to the group of the lead salt semiconductors. They have rock salt lattice or sodium chloride structure and while technically IV-VI materials are pseudo II-VI semiconductors. The high atomic number of the Pb cation renders the 6s orbital chemically ineffective making the group IV Pb an effective group II element [38]. Their bandgap, as in the more conventional zincblende (e.g. CdSe and ZnSe), is direct, but occurs at the L point in the Brillouin Zone rather than at the Γ point. The L-point is 4 fold degenerate which, together with the electron spin makes the first excited state 8-fold degenerate and not 2 fold degenerate as in the other II-VI materials. Most importantly the PbS and PbSe materials investigated in this work have narrow bandgaps as well as small and similar effective masses of their electronic charge carriers in the valence and conduction band (see Table. 4-1). The small bandgap of 0.41 eV and 0.28 eV for PbS and PbSe respectively enables these QDs to be used at IR wavelengths, starting at 3μm in the case of PbS and 4.4μm for PbSe. (see Eq. 2-3). Due to the small effective masses the Bohr Radius of these materials is large and quantum confinement effects are strong. Therefore, they can be tuned substantially by changing the QD size from the mid IR into the visible regime, covering the important telecommunication window.

Table 4-1 Charge carrier parameters and bandgap for PbS and PbSe [39].

	Bandgap (eV) (300k)	Effective Mass m_e^*	Effective Mass m_h^*	Bohr Radius a_B (nm)
PbS	0.41	0.085	0.085	18
PbSe	0.28 eV	0.047	0.041	46

Even more important is the fact that the effective masses are almost identical in the case of PbS and still very similar in PbSe (see Table 4-1). Consequently both electronic carriers enter the strongly quantum confined state at the same QD radius. This is in contrast to other II-VI QDs where the heavier holes are much more weakly confined than the light electrons. The QCL are therefore symmetric in the valence and conduction band. This gives an important insight into the behavior of the lead-salt QDs like the positions of the optical transitions which accrue bunched together in narrow energy regions and are not spread as far apart as in CdSe (see Fig. 4-1).

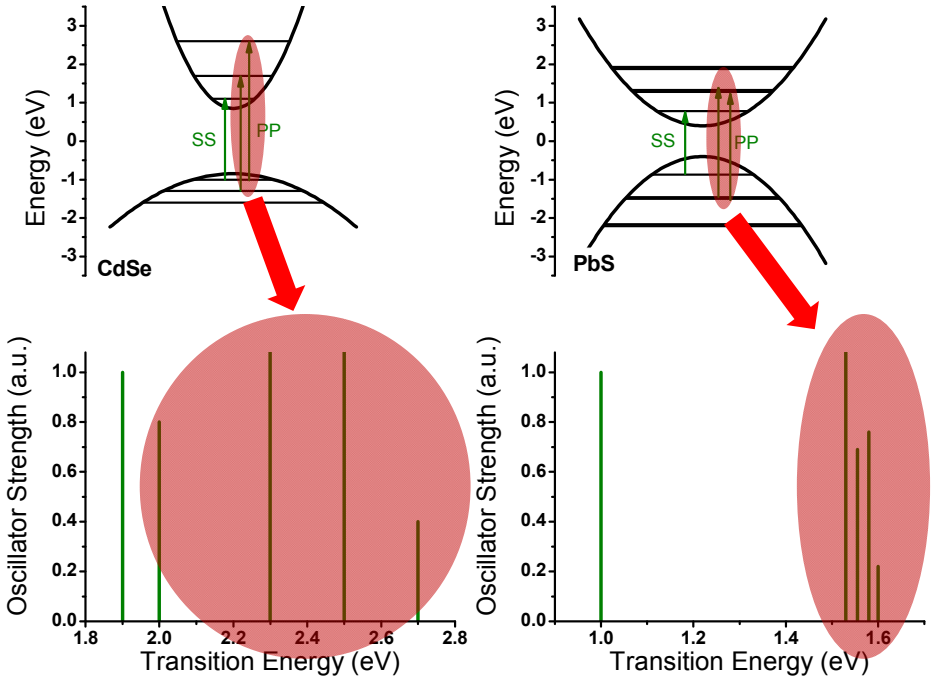

Figure 4-1: Distribution of the QCL in CdSe and PbS and the resulting energies distribution of the optical one-photon transitions.

4.1. ***Sample Preparation***

The lead salt samples investigated in this work are oleic acid caped colloidal PbS and PbSe QDs suspended in toluene. The QDs are grown by our collaborators in Toronto, Canada (see acknowledgments) using a solution-based organometallic route [40, 41]. The QDs are synthesized and purified using standard air-free techniques in two-neck flask equipped with magnetic stirrer, thermocouple, and heating mantle. Lead oleate stock solution (SS) used for PbS and PbSe synthesis is prepared by pumping the mixture of 4.0 mmol of PbO (0.9 g), 9.5mmol of

OA (2.67 g) and 18.8 mmol of ODE (4.73 g) at 100°C for 16 hours. The sulfur or selenium precursors were prepared in a Nitrogen-filled Glove box.

A mixture of 4.5 mL of SS and 15 mL of ODE is pre-pumped at 1000°C for 30 min for each synthesis. The sulfur or selenium precursors are quickly injected. Then the heater is turned off without removing the heating mantel and the reaction flask is let to cool down slowly. The Sulfur precursor for PbS QDs synthesis is prepared by mixing of 2.0 mmol bis(trimethylsilyl)sulfide (TMS) with 10 mL ODE. In a typical synthesis after the injection of sulfur precursor at 70°C the solution slowly turns from colorless to yellow – orange – red to brown indicating the formation of PbS NCs. When the temperature reaches 30-35°C the reaction is quenched by injecting 40 mL of room temperature Acetone. The size of the final quantum dots depends on the injection temperature (60°C to 120°C) as well as by the reaction time. The PbS oleate capped QDs are isolated from any side products by precipitating with acetone and redispersing in toluene repeatedly. The isolation and purification of the QDs is done in a glove box under Nitrogen atmosphere to avoid contact with oxygen and moisture. The resulting PbS QDs are redispersed in Toluene and stored under Nitrogen. PbSe QDs are prepared following the same procedure described for PbS QDs with a Se precursors TMSe (bis(trimethylsilyl) selenide). Especially the PbS QDs have very good size distribution (~±3%) as is evident from the numerous and well pronounced quantum confinement features in their linear absorption spectrum (Fig. 4-2a) (typical size distribution of PbSe samples, (~±7%). By taking the second derivative of the linear absorption spectrum the curvature of the spectrum is calculated. This is a simple way of highlighting the individual transitions in the linear absorption spectrum which might be difficult to distinguish by eye. This is shown in Fig. 4-2b where the inverted second derivative is superimposed on the linear absorption spectrum.

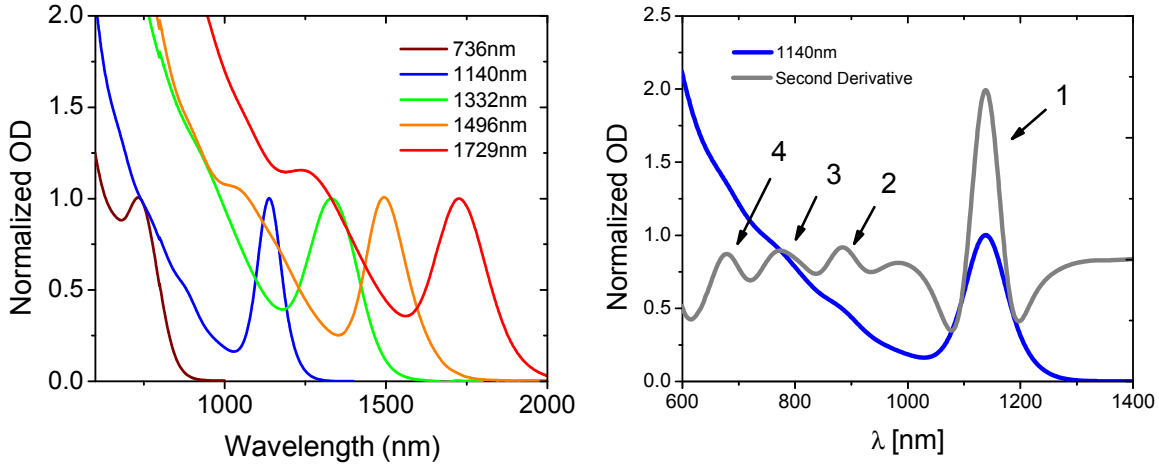

Figure 4-2: (a) Linear absorption of different sized PbS QDs with 1.3nm, 2.4nm, 2.8nm and 3.7nm radius corresponding to the wavelength of the first absorption peak of 736nm, 1140nm, 1332nm, 1496nm and 1729nm respectively. (b) Linear absorption spectrum of 2.2nm PbS QD. The inverted second derivative highlights 4 identified QCLs.

The size distribution can be found by using the wavelength at FWHM of the first absorption peak to calculate the radius of the QDs and comparing it to the QDs radius at the peak wavelength.

2PA measurements are performed at room temperature by either open-aperture Z-scan (Chapter 3.4, p. 31) or 2PF (Chapter 3.5, p. 35). In this study the 2PA is determined by 2PF whenever the wavelength limitations of the 2PF setup do not prevent it. All 2PF measurements are calibrated at several wavelengths by Z-scan in order to obtain absolute values.

For all measurements the QD colloids are contained in 1mm spectrophotometer UV quartz cells (Sterna, Type 21-Q-1), except for the 2PF measurements where 10mm fluorometer cells (Sterna Cells, Type 23-Q-10) are used. Linear absorption spectra are taken with a Cary 500 UV-Vis-NIR spectrophotometer with an identical cell containing toluene in the reference arm.

4.2. *The breaking of the wavefunction symmetry*

The ***k·p*** model which was described in detail in Chapter 2.3 treats the QDs as ideal spheres in which the constituent atoms are symmetrically distributed around the center of the sphere. Hence the electronic wavefunctions possess well defined symmetry and the possible 1PA and 2PA transitions should obey strict but opposite parity selection rules. However, due to the experimental observation of 1PA peaks in the linear absorption spectra (see Fig. 4-5) at energies where the parity selection rules only allow 2PA transitions, the robustness of the parity selection rules and the validity of the isotropic model in its entirety are currently under intense and controversial discussion[42-46].

Some researchers address the nature of the second observed 1PA peak by considering the band anisotropy of the bulk either in the ***k·p*** four-band envelope formalism [42, 43], or in atomistic pseudo-potential calculations [44, 45]. Due to the band anisotropy, the $1P_{h,e}$ levels are spread in energy, leading to 1PA transitions ($1P_h \rightarrow 1P_e$) that energetically coincide with the 2PA allowed $1S_h \rightarrow 1P_e$ and $1P_h \rightarrow 1S_e$ transitions for PbSe QDs Optical [47], potentially explaining the extra one-photon transitions not predicted by the isotropic ***k·p*** model. However, band anisotropy fails to predict the second peak in PbS QDs which are more isotropic. This can be seen in Figure 4-3 where the transitions predicted by the isotropic **k·p** is compared to the anisotropic counterpart. In PbSe (Fig. 4-3b) the splitting of the second group of QCL in the anisotropic model is clearly visible, while the transitions in PbS are almost unchanged (see top and button Fig. 4-3b) [42, 43]. Other approaches predict that the inversion symmetry of the wavefunctions is broken in lead-salt QDs allowing optical transitions which are parity forbidden according to the simple ***k·p*** four-band envelop function formalism [47].

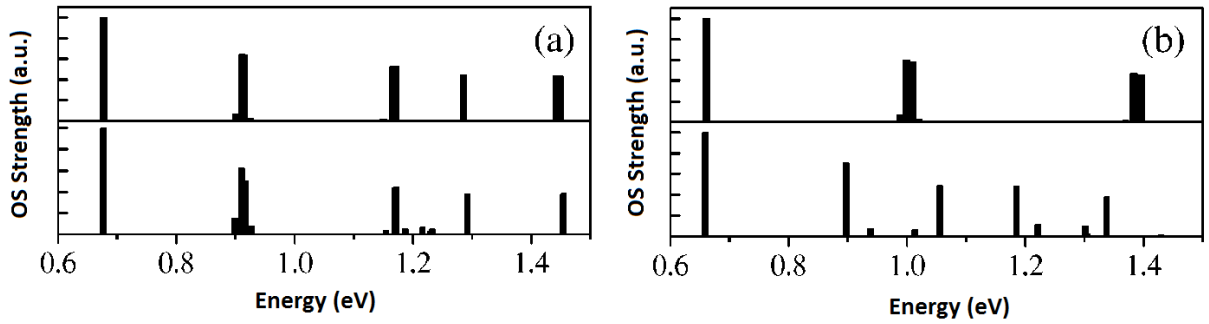

Figure 4-3: Transition Strength of (a) PbS and (b) PbSe QDs with 4 nm radius. The isotropic (anisotropic) results correspond to the top (bottom) graph. From Ref. [43].

Figure 4-4 shows a schematic of the possible 1PA and 2PA transitions according to the different models. Figure 4-4a shows the allowed transitions of the isotropic $\boldsymbol{k \cdot p}$ model with strict parity selection rules [14], Figure 4-4b shows only parity allowed transitions but takes into account the splitting of the electronic states due to anisotropy [42, 43] and Figure 4-4c includes the formally parity forbidden transitions of the isotropic bands which become allowed by breaking the parity selection rules [46]. Possible mechanisms leading to the breaking of the selection rules will be discussed later. Note from Figure 4-4c that only the model considering symmetry breaking predicts two-photon transitions at the same energy as the one-photon allowed 1Sh → 1Se transition.

Still, to date, there is no consensus in the literature for the physical origin of the second transition in lead salt QDs. This chapter will shine some light on the origin of this transition.

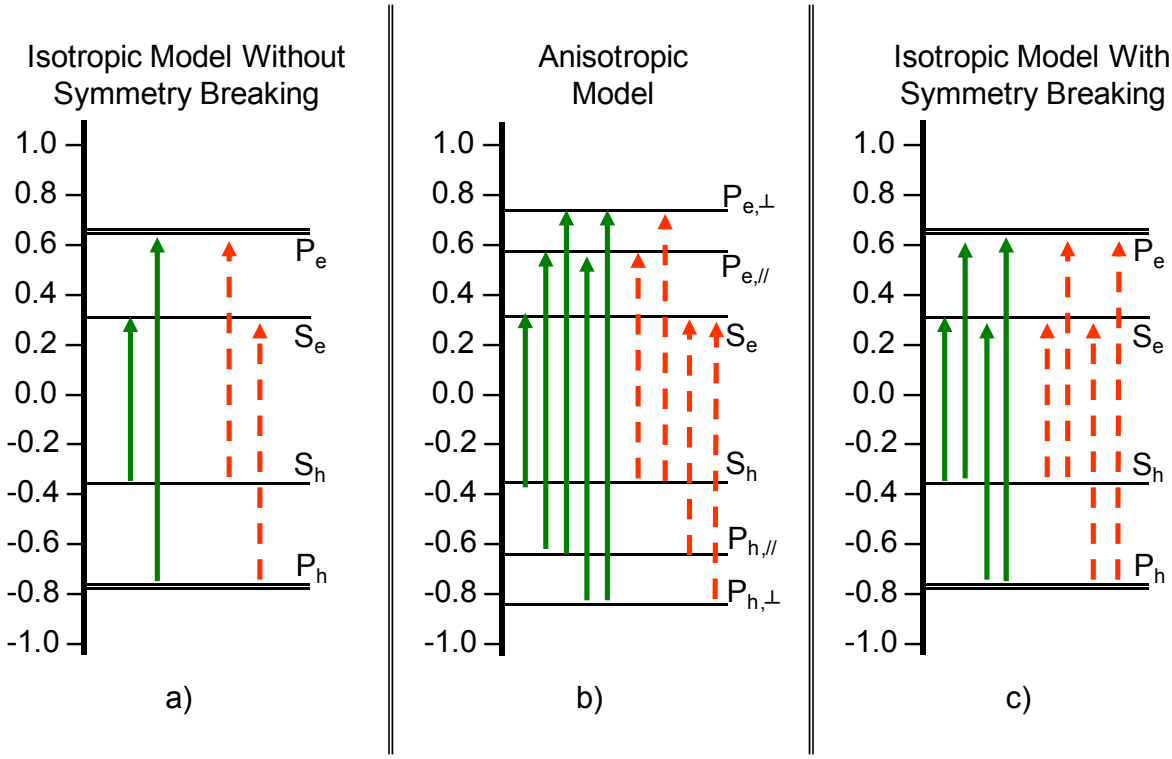

Figure 4-4: Schematic diagram of three different theoretical approaches for the one- and two-photon transitions in lead salt QDs. One-photon transitions are indicated by green/solid lines, two-photon transitions are indicated by red/dashed lines. 1a) parity allowed transitions according to the isotropic ***k·p*** four-band envelope function formulism. 1b) parity allowed transitions considering the anisotropy of the PbSe bulk semiconductor. 1c) possible one-and two-photon transitions if the principal parity forbidden transitions are allowed.

Despite the fact that most studies on this topic have been performed on PbSe QDs, we find that PbS QDs are better suited to study the origin of the second peak in the linear absorption spectra. This is because of the more isotropic bands in PbS which lead to reduced density of transitions and lets us answer the question of the origin of the second transition in the linear 1PA spectra more easily.

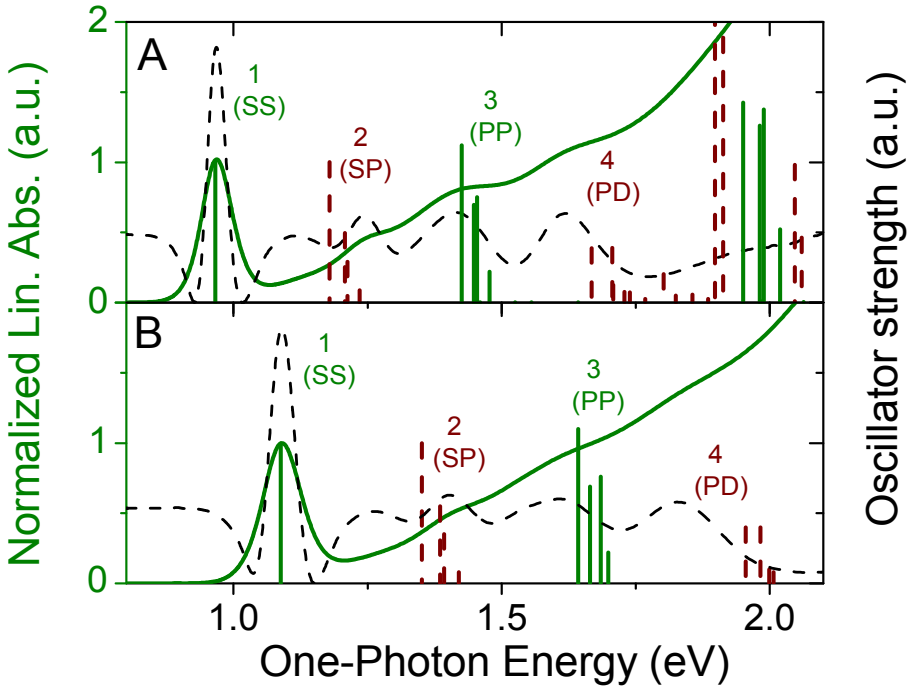

Figure 4-5: A) Linear absorption spectrum of 2.3nm PbS QDs (solid green lines) and inverted second derivative (dashed black line) indicating identifiable transitions. Calculated one and two photon transitions are shown as vertical lines (green/solid are one photon transitions, red/dashed lines are two photon transitions). Transition 1 (SS) and 3 (PP) accrue at energies where one photon transitions are theoretically predicted, but transitions 2 (SP) and 4 (PD) are at energies where the theory only predicts 2 photon allowed transitions. B: Same as in A) for a smaller PbS QD (r=2nm).

Figure 4-5 compares the 1PA- and 2PA transitions predicted by the four-band envelope function model with the linear absorption of two PbS QDs with the $1S_h \rightarrow 1S_e$ peak at 0.97eV and 1.09eV (at room temperature). Due to the nearly equal effective masses of the carriers in the valence and conduction bands [14], the allowed 1PA and 2PA transitions are grouped together in narrow energy ranges. As previously observed by several authors in PbSe QDs [47], our measurements in PbS QDs, show that the second peak in the linear absorption spectrum occurs at

the energy of the first group of theoretically predicted 2PA $1S_h \rightarrow 1P_e$ and $1P_h \rightarrow 1S_e$ transitions (seeFig. 4-5, feature 2). This represents a problem since the $1S_h \rightarrow 1P_e$ and $1P_h \rightarrow 1S_e$ transitions are forbidden by the 1PA selection rules. However, because of the good agreement in terms of energy, it has been suggested that the second peak in the linear absorption spectrum should be attributed to these parity forbidden transitions which become allowed due to some mechanism which breaks the wavefunction's inversion symmetry [47, 48]. (It should be noted that the two-photon transitions in Figure 4-5 only indicate the energies at which the theoretically forbidden one-photon transitions occur, but do not reflect their magnitudes.) Subsequent experimental observation of a strong 2PA peak with the energy of the nearly degenerate SP transitions confirmed the existence of two-photon allowed transitions at these energies [46] in agreement with the predictions by the isotropic $\boldsymbol{k \cdot p}$ model. Figure 4-5 shows that, as for the second peak, also the fourth identifiable peak in the 1PA spectrum agrees with the second group of 2PA allowed transitions ($1P_h \rightarrow 1D_e$ and $1D_h \rightarrow 1P_e$) at energies where again one-photon transitions are not expected. Therefore, in analogy to the second peak in the linear absorption spectra, this fourth feature may also be explained by inversion symmetry breaking.

With the assumption, justified by the extra peaks in the 1PA spectra, that the parity selection rules are weakened in these QDs, one would expect to observe 2PA at energies corresponding not only to the parity allowed two-photon transitions, $1S_h \rightarrow 1P_2$ and $1P_h \rightarrow 1S_e$, but also to the two-photon forbidden ones ($1S_h \rightarrow 1S_e$ and $1P_h \rightarrow 1P_e$).

To verify this expectation we have performed 2PA spectroscopy in a series of PbS and PbSe QDs. Fig 4-6 shows the open aperture Z-scan traces for three different energies together with the fittings for the 2PA model at 2.48eV in Fig. 4-7B. All energies can be fitted with the same two-photon coefficient verifying that observed signal is in fact due to 2PA. Similar conclusions can

be drawn from the 2PF measurements, where the fluorescence signal was found to vary with the second power of the excitation energy. This again is indicative of 2PA.

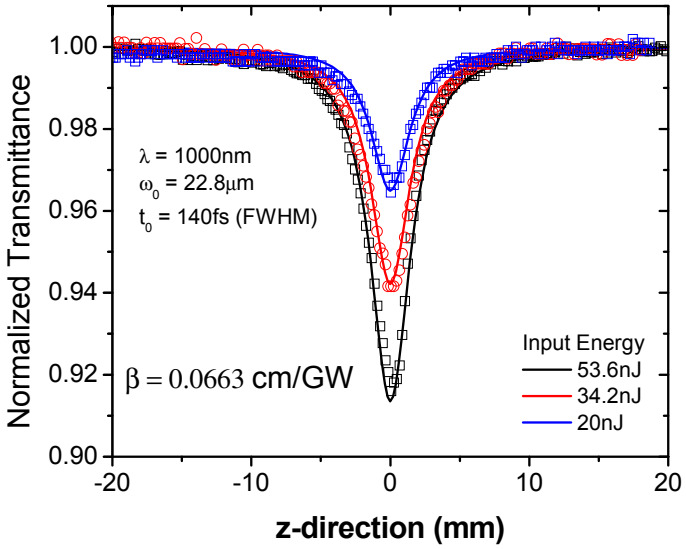

Figure 4-6: Open aperture Z-scan curves for 730nm PbS QD. Symbols are the experimental values and the fittings are shown as solid lines.

Figure 4-7 shows the measured 2PA spectra for different sizes of PbS and PbSe QDs together with their linear absorption and the predicted one- and two-photon transitions. The QD radii used in the calculation are chosen to match the energy of the first linear transition and might be somewhat smaller than the real QD size determined i. g. by the empirical method outlined in Chapter 4.3 [49]. Then, the four-band envelope function model works reasonably well to provide the relative position of the first allowed 1PA transition and the first 2PA allowed transitions for larger PbS and PbSe QDs. For smaller QDs, due to the overestimated confinement energies, the theory predicts a larger spread between these transitions than experimentally observed.

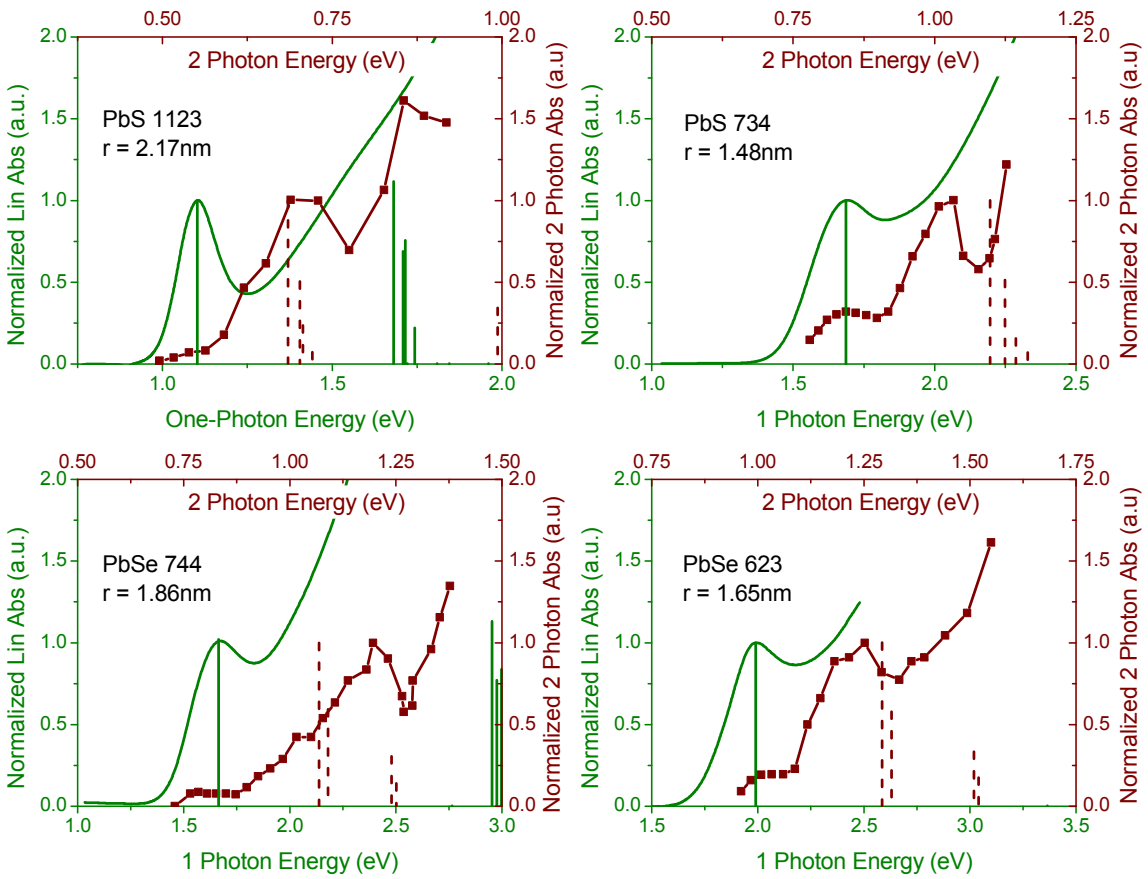

Figure 4-7: One- and two-photon absorption spectra for PbSe and PbS QDs of different sizes together with the theoretically predicted one- and two-photon transitions. The 1PA spectrum is drawn as solid green lines and the 2PA spectra as red lines plus symbols. Theoretical one- and two-photon transitions at their respective energies are vertical lines with their height indicating the oscillator strength (one-photon transitions are green/solid lines, two-photon transitions are red/dashed lines).

Note that the oscillator strength of the one- and two-photon transitions (as indicated by the height of the vertical lines in Fig. 4-7) only has meaning for parity allowed transitions and can only be used to indicate the position in energy, but not the strength, of possible symmetry forbidden transitions. For the PbS QDs studied we are able to identify three peaks in the 2PA spectrum. For example, for PbS QDs in Fig. 4-7 A the peaks are identified at 1.10 eV, 1.35 eV

and 1.60 eV. For the second PbS QDs in Fig. 4-7 B the peaks are located at 1.70eV, 2.03eV and 2.44eV, which, due to the known overestimation of the quantum confinement, occur at lower energies then predicted by theory. These features are observed for a third sample, with nearly identical energies as those in Fig. 4-7 A (first peak at 1.13eV, not shown). However, for all samples shown in Fig. 4-7 only the second observed 2PA transition is parity allowed according to the ***k·p*** model. The first, and in the case of the PbS samples, the third 2PA feature, occur at energies for which the model predicts the first and the second 1PA allowed transitions ($1S_h \rightarrow 1S_e$ and $1P_h \rightarrow 1P_e$, respectively), indicated by the green lines in Fig. 4-7. The third two-photon transition cannot be measured for all samples, since the transitions are close to the 1PA edge, and the size inhomogeneity prevents us from investigating the 2PA spectrum for photon energies larger than ~0.85 x E_g. However, for all samples we observe a strong increase of 2PA at energies higher than the first two-photon allowed peak, indicating the proximity of a third 2PA peak possibly corresponding to the $1P_h \rightarrow 1P_e$ transition. While the presence of 2PA peaks at energies equal to that of and $1P_h \rightarrow 1P_e$ transition could possibly be explained by the increasing number of states due to any anisotropy, the 2PA peak at the position of the $1S_h \rightarrow 1S_e$ transition unambiguously confirms that the inversion symmetry of the wavefunctions are broken and need to be considered in the analysis of optical transitions and electronic structures of lead-salt quantum dots.

As can be seen in Fig. 4-7, the magnitude of the 2PA at the $1S_h \rightarrow 1S_e$ transition increases with decreasing QD radius for PbS and PbSe. This is evident by comparing the ratio of the magnitude of the 2PA at the energy of the first one-photon allowed transition ($1S_h \rightarrow 1S_e$ transition) and the magnitude of the 2PA at the energy of the allowed SP transitions as shown in Fig. 4-7. A similar trend is observed if one compares the ratio between the third and second 2PA

peaks measured in PbS QDs (Fig. 4-7). The relative strengthening of the formally parity forbidden 2PA (at $1S_h \rightarrow 1S_e$ and $1P_h \rightarrow 1P_e$) compared to the magnitude of the allowed two-photon SP peaks with decreasing QD radii indicates that the mechanism responsible for the breaking of the parity selection rules originates from the quantum confinement. As suggested in Ref. [50]: Drastic effect of structure inversion asymmetry this may be due to the shift of the crystal lattice away from the QD spherical center thereby lifting the perfect inversion symmetry of the wavefunctions so that forbidden transitions become allowed. A shift of the center atom away from the center of the QD will have a more pronounced effect for the smallest QDs in this study which, from the estimated sizes, have only ~7 atoms across the diameter, as compared to ~13 atoms across for the largest dots. Also conceivable is, that shape variations away from the perfect sphere or simply surface roughness is responsible for the breaking of the wavefunctions symmetry in smaller QDs.

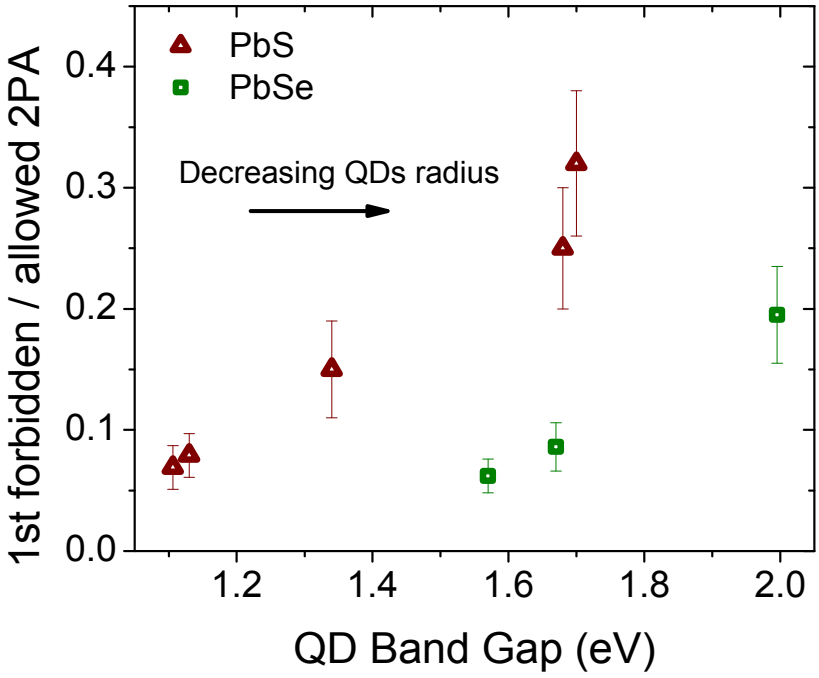

Figure 4-8: Ratio of the 2PA cross-section at the energy of the first one-photon allowed transition divided by the 2PA cross-section at the energy of the first group of two-photon allowed transitions plotted versus the band gap of the QDs.

The experimental observation of 2PA at the $1S_h \rightarrow 1S_e$ energy for PbSe QDs is in contrast to the results of Ref.[46] where 2PA at the position of the first 1PA allowed transition was not found. This is despite their observation of relatively strong 1PA at the energy of the first two-photon allowed SP transitions in PbSe QDs. Our results show that the 2PA at the $1S_h \rightarrow 1S_e$ energy is appreciable only for small PbSe QDs, with a band gap larger than ~1.55 eV, and the samples studied in Ref. [46] were notably larger than the ones investigated here (the smallest dot studied in Ref. [46] has a band gap of ~1.05 eV).

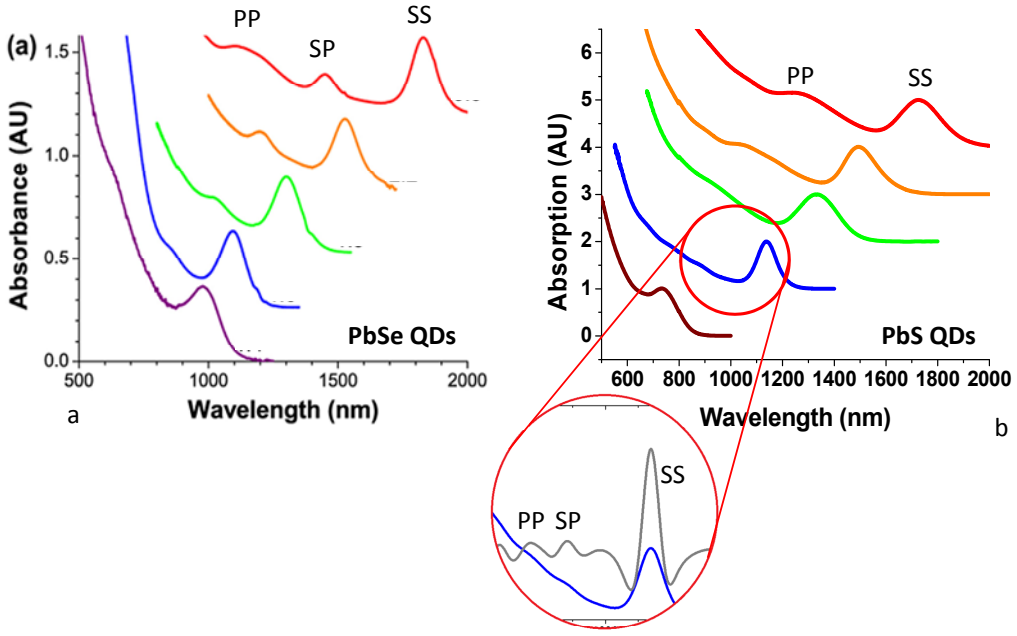

Figure 4-9: Linear absorption spectrum of PbSe QDs from Ref. [51] (a) and PbS measured in our laboratory (b). The insert highlights the energy region of the SP transition in a PbS QD which is emphasized by the inverted second derivative of the linear absorption spectra (gray line)

While the results from Fig. 4-5and Fig 4-7 and show that the parity selection rules are broken in both PbS and PbSe QDs, from Fig. 4-8 it is evident that the effect is stronger in PbS QDs. One possible explanation could be the difference in energy separation of the valence quantum confined energy levels in PbSe and PbS QDs, which would result in smaller intermediate state resonance enhancement for PbSe (denominator in Eq. 2-50). However, for the QD sizes investigated here, the intermediate state resonances are very similar for PbS and PbSe QDs and do not account for the difference in the magnitude of the 2PA at the $1S_h \rightarrow 1S_e$ transition energy.

Comparing the magnitude of the second linear absorption peak in PbS QDs from Fig. 4-2 and Fig. 4-5 to the magnitude of the second peak in PbSe QDs from the literature [51-53], it is clear that the second peak is less pronounced in PbS. This could be an indication that while the second

peak in PbSe QDs is due to contributions from anisotropy and symmetry breaking, the weaker second peak in PbS has its origin in symmetry breaking alone.

However, comparing the 2PA spectrum of PbS and PbSe, one sees that the ratios between the magnitude of the formally parity forbidden and parity allowed 2PA is lower in PbSe than in PbS (Fig. 4-8), indicating a stronger breaking of the inversion symmetry in PbS than in PbSe. So, while the measured 2PA peak at the $1S_h \rightarrow 1S_e$ transition shows that symmetry breaking needs to be considered to fully describe optical transitions in lead-salt QDs, the relatively stronger second peak in the 1PA spectra of PbSe versus PbS suggests that this second peak in PbSe is actually a combination of transitions due to band anisotropy and breaking of the inversion symmetry, with the latter being stronger for smaller QDs.

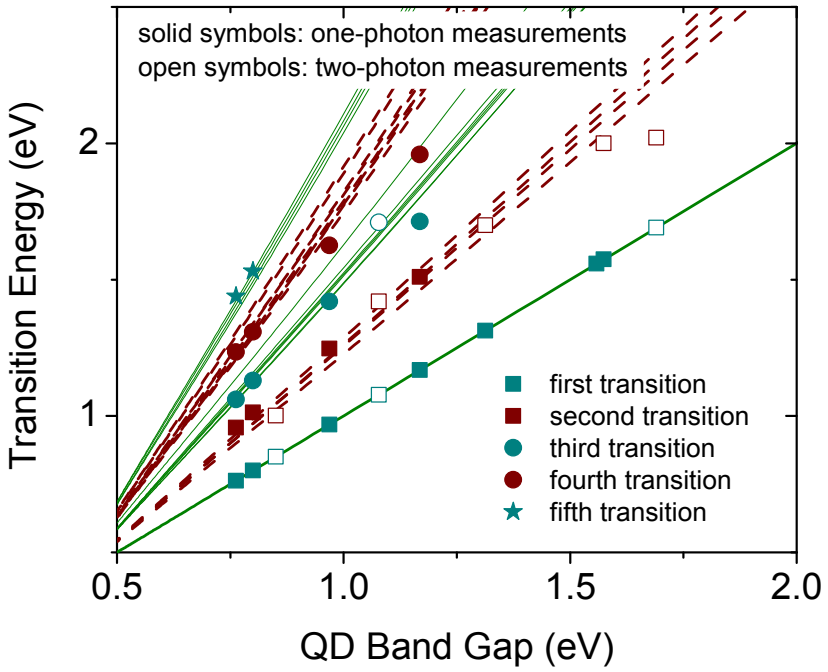

Figure 4-10: Transition energies in PbS QDs as measured by one and two-photon experiments plotted verses the QD band gap (energy of the first absorption peak). Transitions identified in the linear spectrum are shown as solid symbols while the open symbols are measured by either Z-

scan or 2PF. Theoretical predictions are shown as green/solid lines and red/dashed lines for parity conserving transitions and transitions between states of different parity respectively.

Figure 4-10 summarizes the identifiable features in the one- and two-photon spectra of PbS QDs and shows good agreement with the isotropic ***k·p*** four-band envelope function formalism up to the fifth transition and over a wide range of QD sizes. This illustrates that, for the more isotropic PbS QDs, all measurable features are predicted by the model if formally parity forbidden transitions are included.

4.3. *Enhancement of Two-Photon Absorption with Increased Quantum confinement*

The dependence of the 2PA magnitude on the size of the QDs is of importance for applications such as optical switches, two-photon absorption fluorescence imaging and optical power limiting. Initial theoretical calculations suggested that the two-photon absorption (2PA) in QDs should increase with increasing quantum confinement [54]. However data taken in our group have shown that the 2PA cross-sections of CdSe and CdTe QDs are in fact decreasing for smaller QDs even after the results have been normalized to the volume of the QDs [55]. It was then realized that, while the oscillator strength of the single transition is indeed increasing for smaller dots, the spreading of the density of states due to increasing quantum confinement overcompensates for this increased oscillator strength and ultimately smaller QDs have smaller 2PA cross-sections. The picture is different in the lead salt semiconductor materials which as mentioned in Chapter 4 possess similar effective masses of their electronic carriers and therefore the quantum confined energy levels in the valance and conduction band are symmetrically

distributed (Fig. 4-1). This leads to 2PA transitions which in contrast to their counterparts in other QDs (as it is the case for the one-photon transitions) are confined to narrow energy regions (see Fig. 2-8). As a result the increase of the individual transition strength may not be compensated and the 2PA could be effectively increased.

In order to investigate whether in fact the 2PA cross-sections increase with increased quantum confinement the same data as in section 4.2 is analyzed with respect to the strength of the 2PA at the energy of the parity conserving SP transitions. The cross-sections per QD in Goeppert-Mayer (GM) is calculated from the experimentally determined 2PA coefficient α_2 (cm/GW) by means of Eq. 4-1.

$$\delta(\omega) = \rho^{-1} \frac{\hbar\, \omega\, \alpha_2(\omega)}{N}. \qquad (4\text{-}1)$$

In Eq. 4-1 ρ is the local field correction factor from Maxwell-effective medium theory [56],

$$\rho = \frac{3\varepsilon_S}{\varepsilon_{QD}+2\varepsilon_S}, \qquad (4\text{-}2)$$

which is assumed to be constant over the range of the experiment. N is the concentration of the QDs in the sample in $1/cm^3$ and $\varepsilon_{S,QD}$ is the dielectric constant of the solvent and of the QD respectively. Concentrations are calculated using a method by Ludovico Cademartiri et. al [49]. By integrating the optical density (OD) of the first 1PA peak. Since on the short wavelength side of the first peak, higher laying transitions influence the absorption, only the first halve of the peak is integrated and then multiplied by 2. Samples with a narrow size distribution will exhibit high but narrow peaks and samples with broader distributions will have lower but broader peaks, therefore by integrating the area of the absorption one can compensate for the effect of the different size distributions of QDs in the samples. The value of the integral ($\int OD$) is then

divided by the empirically determined extinction coefficient ε and the length of the sample (1mm in our case). This way an empirical measure of the concentration, c in mol/cm^3, is found.

$$c = \frac{\int OD}{\varepsilon(r) \times l}. \tag{4-3}$$

Where ε(r) is the extinction coefficient in M^{-1} cm^{-1} found in ref. [49]

$$\varepsilon(r) = 203079\, r^{2.49}. \tag{4-4}$$

In order to be consistent, the radius (r) in nm used in Eq. 4-4 is calculated from an again empirically found formula (Eq. 4-5) in the same reference [49].

$$E_1(eV) = 0.41 + 0.96/r^2 + 0.85/r. \tag{4-5}$$

Here E_1 is the energy (in eV) of the first linear absorption peak.

The 2PA cross-sections σ calculated from the measured 2PA coefficient α_2 are shown in Fig. 4-11. The 2PA cross-section at the first 2PA allowed peak decreases with the size of the QDs ranging from 22,000 GM, for the largest QDs (r = 2.61 nm) to 6900 GM for the smallest QDs (r = 1.55 nm). However, if the measured 2PA cross-sections are normalized by the volume of the QD's, the trend is reversed, and, at the first 2PA allowed peak, the volume normalized 2PA cross-section increases from 500 GM/nm^3 to 800 GM/nm^3 as the QD's radius decreases from 2.61 nm to 1.55 nm. While it may not be surprising that larger QDs possess larger 1PA and 2PA cross-sections it is important for any possible application that the volume normalized cross-sections are increasing with decreasing size, since for a given volume filled with QDs the smaller dots will have the larger two-photon coefficient α_2.

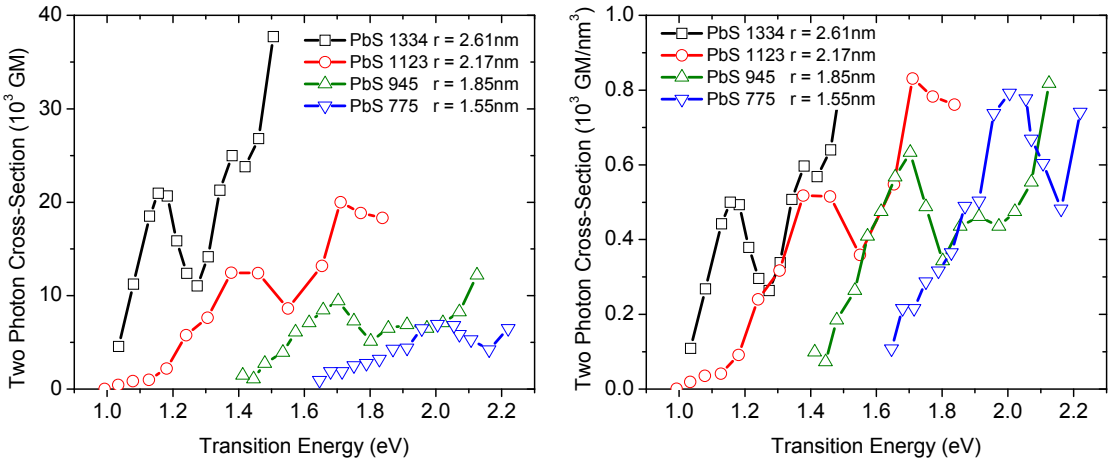

Figure 4-11: (a) 2PA cross-section spectra for PbS QDs of different size. (b) 2PA cross-section of the same samples normalized to the volume of the QDs.

In order to compare the 2PA cross-sections of different samples to the predictions of the ***k·p*** model it is important to consider their size distributions. The same logic that was used to determine the QD concentration from the area under the first linear absorption peak applies here and is used to compare the 2PA strength. By fitting the $1P_h \rightarrow 1Pe$ peaks with a Gaussians the areas underneath these peaks is determined. This integrated 2PA can then be compared to the predicted oscillator strength. Generally good agreement between theory and experiment is found for the trend of the 2PA with changing QD size. This is true for the 2PA cross-sections per QD as well as the volume normalized cross-sections (see Fig. 4-12).

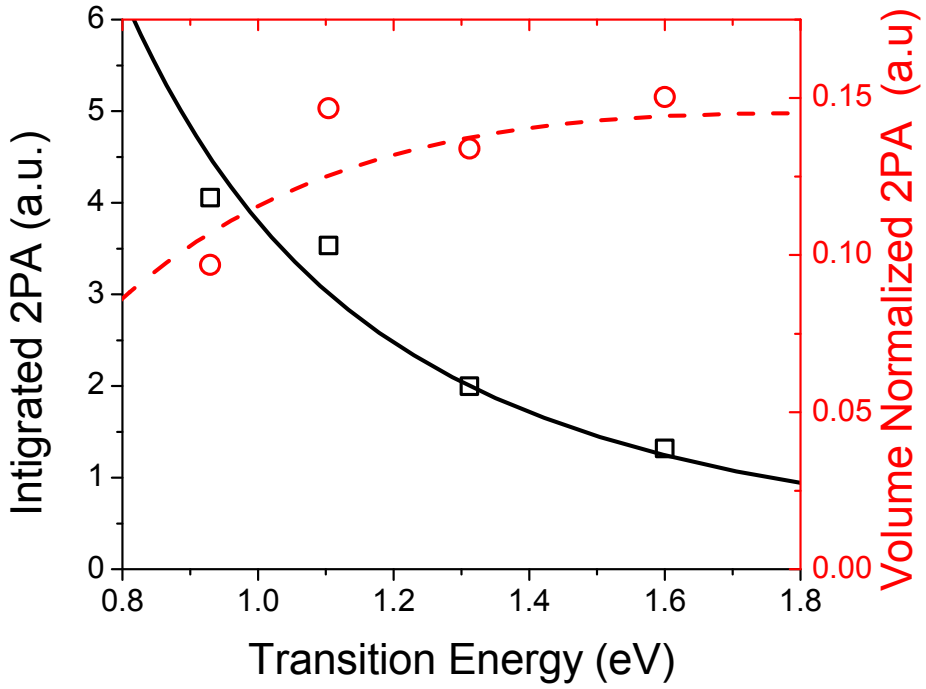

Figure 4-12: Integrated volume normalized 2PA as measured in Fig. 4-11 black (red) symbols compared to the predictions of the ***k·p*** theory, solid black (dashed red) lines.

4.4. ***Nondegenerate 2PA in PbS QDs***

One approach to further enhance the 2PA in QDs is to use photons of different energies. This is known as nondegenerate 2PA. This is in contrast to the degenerate 2PA of the previous chapter where the wavelength of the 2 photons absorbed is identical. In the nondegenerate case the resonant denominator in Eq. 2-49 can be made small leading to intermediate state resonance enhancement (IRSE) and ultimately enhanced 2PA. A more intuitive picture is to imagine the virtual level involved in the process. Since the time in which a system can exist in a virtual excited state after it has been excited by a photon is determined by the Heisenberg uncertainty

principle [57] $\tau = \hbar/\Delta E$, the second photon must follow the first within this time in order to complete the transition into a real level whereby the transition has to conserve the energy of the two photons involved. If the detuning energy between a real level and the virtual level (ΔE) is small, the lifetime (τ) is relatively large and the chance of a complete 2PA process is increased. By using photons of different energies the detuning energy (ΔE_2 in Fig. 4-13) can be made smaller than for the degenerate case (ΔE_1 in Fig. 4-13) and consequently the 2PA is enhanced. This has been shown to work extremely well in bulk semiconductors by our group [58], where up to 180x enhancement was demonstrated.

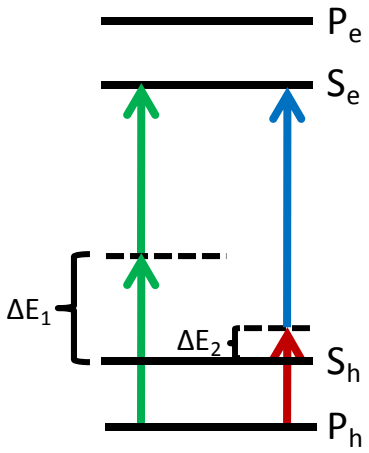

Figure 4-13: Degenerate versus non-degenerate 2PA in a generic QD. In the degenerate case (green arrows) the photon energy is the same for both photons and the detuning energy (ΔE_1) of the virtual level (dashed line) is large. For the non-degenerate case on the other hand the virtual level can be relatively close to a real level (solid lines) hence the detuning energy (ΔE_2) is small.

While it is possible to measure nondegenerate 2PA by two color Z-scans [59, 60] this technique is difficult to align and, therefore, we opted to use the somewhat easier to manage WLC pump-probe method described in section 3.6.

The PbS QD sample used to study nondegenerate 2PA has its first linear absorption peak at 920nm with an optical density of 12.3. For such low linear transmittances ($T=5\times10^{-13}$) the linear absorption spectra cannot be measured directly with a spectrophotometer (Varian Cary 500) and therefore the linear absorption spectrum is determined by overlaying and scaling the linear absorption spectra of a lower concentration sample of the same QDs at the onset of the absorption where for both samples the transmittance can still be measured. The method has been tested by diluting a test sample successively and then subjecting the dilutions to the same procedure. A linear scaling of the peak optical density and the concentrations was found, verifying the validity of the method as well as ruling out the possibility of QD aggregation in these high concentrations. In order to avoid degenerate 2PA from the short wavelength component of the two beams needed for nondegenerate 2PA the high irradiance pump beam is set to a wavelength which correspond to photon energies smaller than ½ E_g. The specific values for the energy and the beam waist in FW/e of the pump are in Table 4-2.

Table 4-2: Pump beam parameters

λ_{Pump} *(nm)*	E_{Pump} *(μJ)*	w_{Pump} *(μm)*
2100	7	380
2400	5	440

The energy of the probe is on the order of pJ and focused to a spot size of ~60μm. With these parameters the probe irradiance is of the order of 5 MW/cm^2. Since the pump and the probe have significantly different wavelengths the dispersion of the sample will cause them to travel with different group velocities. For the 1 mm sample thicknesses used in these experiments the group-velocity dispersion is large enough that this is a significant effect. This reduces the time and effective sample length over which the pump and the probe interact within the sample. This effect has to be considered in the analysis of a degenerate pump probe experiment. The analytical form of the normalized nonlinear transmittance Q (defined as F(1)/F(0)), for pulses with Gaussian temporal profiles, is given in Eq. 4-6 [36]. F(0) is the probe fluence at the front surface where the beams enter the sample and F(1) is the fluence of the probe after the transmittance through the sample. (The Z coordinate in this equation is normalized to the length of the sample L (Z=z/L) i.e. Z = 1 corresponds to z = L)

$$Q(\sigma, \tau_d, W, \rho, \Gamma) = \frac{e^{-2\sigma}}{W\sqrt{\pi}} \int_{-\infty}^{\infty} exp\left\{ -\left(\frac{\tau + \tau_d - \rho}{W}\right)^2 - \frac{\Gamma\sqrt{\pi}}{\rho}[erf(\tau) - erf(\tau - \rho)] \right\} d\tau \quad (4\text{-}6)$$

Here σ is the normalized linear absorption ($\sigma = \alpha L/2$), τ_d is the initial relative delay between pump and probe, W is the ratio of the temporal width of probe and pump ($W = w/w_p$), ρ denominates the group velocity mismatch (GVM) ($\rho = \frac{L}{w_p c}\Delta n_g$) and finally Γ is the normalized 2PA coefficient ($\Gamma = \beta I_p L$). Eq. 4-6 is used to fit the experimental pump probe traces. In the fitting routine τ_p is the variable over which the Q is recorded and σ as well as W are parameters which are known from the experimental setup. This leaves ρ and Γ as fitting parameters. Fig.

4-14 shows a typical fit of a pump-probe experiment where $\sigma = 0$, W=0.896, $\rho = 0.75$ and $\Gamma = 0.073$.

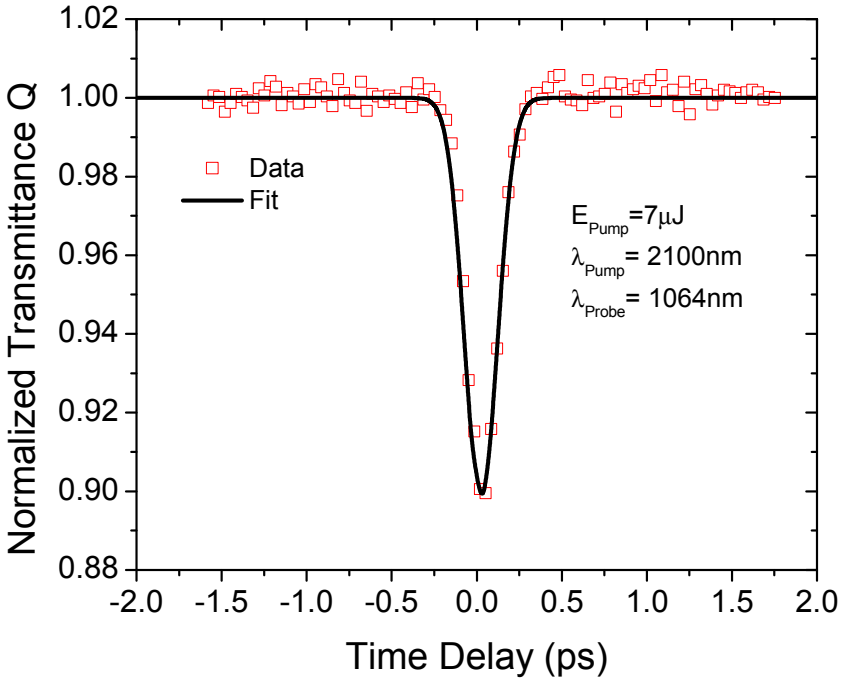

Figure 4-14: Nondegenerate Pump-Probe trace of a PbS QD.

By selecting different parts from the WLC the nondegenerate 2PA spectra of a PbS QD is measured (see Fig. 4-15). The 2PA cross-sections are found to increase with the degree of the nondegeneracy from 700 GM for the degenerate case, to over 1300GM if the pump is set to 2.1μm, to 3100 GM for the case where the photon energies have the greatest nondegeneracy in these experiments and therefore IRSE is large. Greater nondegenerecy cannot be achieved, since, due to the size distribution of the QDs, the probe beam wavelength would fall into the linearly absorbing regime.

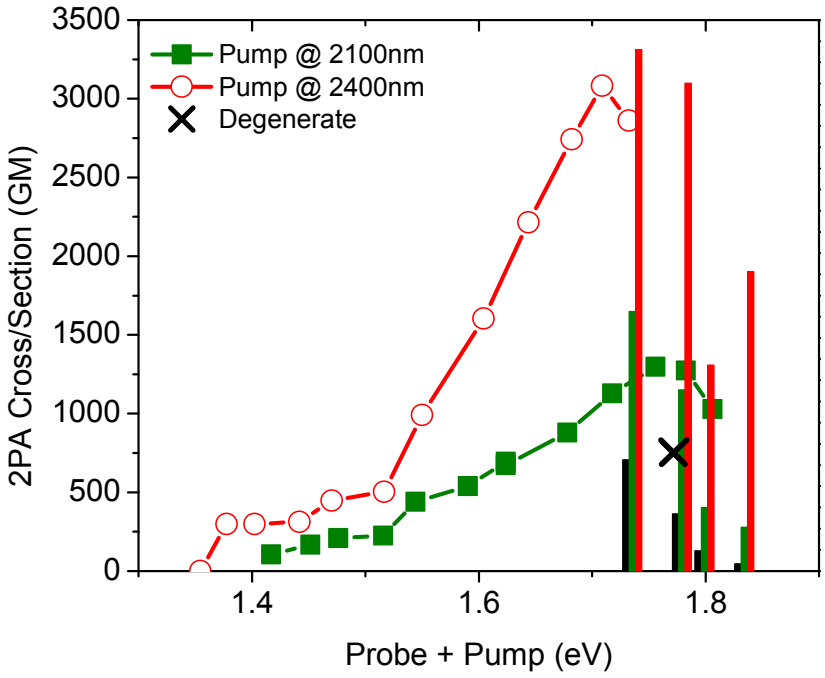

Figure 4-15: Nondegenerate 2PA of a PbS QDs. The QD is pumped at two different wavelengths (2.1μm; green/solid symbols and 2.4μm; red/open symbls) and probed over a range from 1.02μm to 1.5μm. Also included in the figure is the degenerate 2PA at the peak of the SP feature (black cross). The predictions of the ***k·p*** model for the SP transitions are shown as vertical lines (color codes according to the respective experimental values).

The IRSE in PbS QDs compares favorably to the IRSE in CdSe QDs where for the same ratio between pump and probe photon energies, the enhancement is ~2.2x that of the degenerate case (as compared to ~4.5x in PbSe). The difference is again explained by the equal and small effective masses of PbS. The separations between the first QCL (S_1) and the second QCL (P_1) is lager in PbS due to the small effective masses of the electrons and holes compared to CdSe ($m^*_{e,PbS} < m^*_{e,CdSe}$ and $m^*_{h,PbS} \ll m^*_{h,CdSe}$). As is illustrated in Fig. 4-16 the energy mismatch between the real QCL and the virtual level is much smaller in PbS than in CdSe ($\Delta E_{PbS} < \Delta E_{CdSe}$), furthermore the valence S_h state to the electronic P_e state has nearly the same energy

asthe $P_h \rightarrow S_e$ transition which is not the case for CdSe. This transition (crossed out transition in Fig. 4-16) dose therefore not contribute to the two-photon cross-sections at this energies in CdSe.

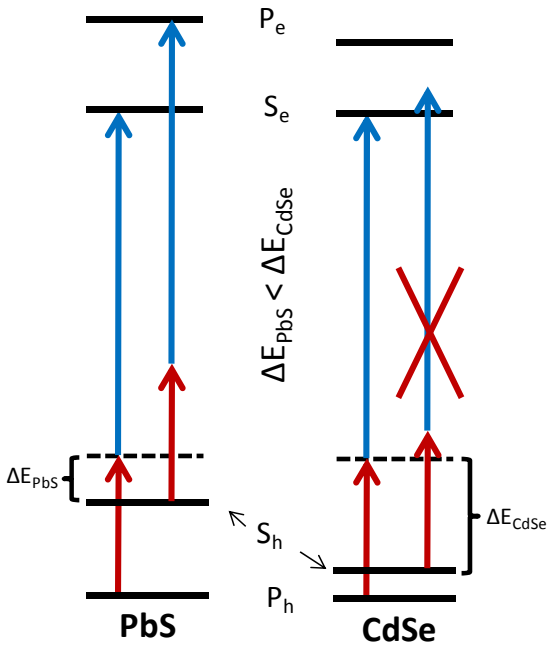

Figure 4-16: Schematic of 2PA in PbS and CdSe showing the energies of the QCL (bleck lines), the virtual levels (dashed lines), the detuning energies (ΔE) and the energies of the two non-degenerate photons involved in the transition (arrows).

Good agreement is found by comparing the experimental results to the predictions of the ***k·p*** model. In Fig. 4-15 the oscillator strength as calculated by the **k·p** model is shown as vertical lines for the degenerate case (black lines) and the non-degenerate case pumped at 2100nm and 2400nm (green and red lines respectably). The relative increase of the oscillator strength agrees well with the increasing two-photon absorption cross-sections found experimentaly.

CHAPTER 5:
TIME DYNAMICS OF THE EXCITED STATES

The previous section was mainly concerned with the interband excitation of carriers by one- and two-photon absorption processes. It is an entirely different matter, however, to determine what happens to carriers once they have been excited into a higher state since the carriers can relax back to the ground state via several channels, radiation being only one of them.

The peculiar band structure of PbS QDs with its almost identical energy levels for electron and holes makes it difficult to independently investigate the dynamics of each type of carrier i. e., electrons and holes. On the other hand as mentioned before, the mirror-like symmetry of the bands bundles the electronic transitions into narrow energy regions so that the spectral features are very well defined. This facilitates the study of the temporal behavior of the electron-hole pairs. Furthermore, since electrons and holes in the respective QCL have very similar energy and effective mass, one can assume that they also have similar intraband dynamics. This chapter addresses the carrier dynamics in PbS QDs and invoke their highly symmetric band structure to explain some of the differences observed in this material as compared to PbSe and CdSe QDs.

The samples studied in this section were prepared in a 1mm quartz cell and the QD concentration was adjusted for a linear transmittance of 80% at the energy of the first absorption peak. A linear transmittance of ~80% is a good compromise between too small of a signal for lower concentrations and a tolerable amount of pump beam depletion as it travels through the sample. Uniform excitation throughout the sample is desirable, since in many cases the carrier dynamics depend on the number of excited excitons per QD which in turn depends on the pump irradiance. Therefore, strong pump depletion is to be avoided whenever possible

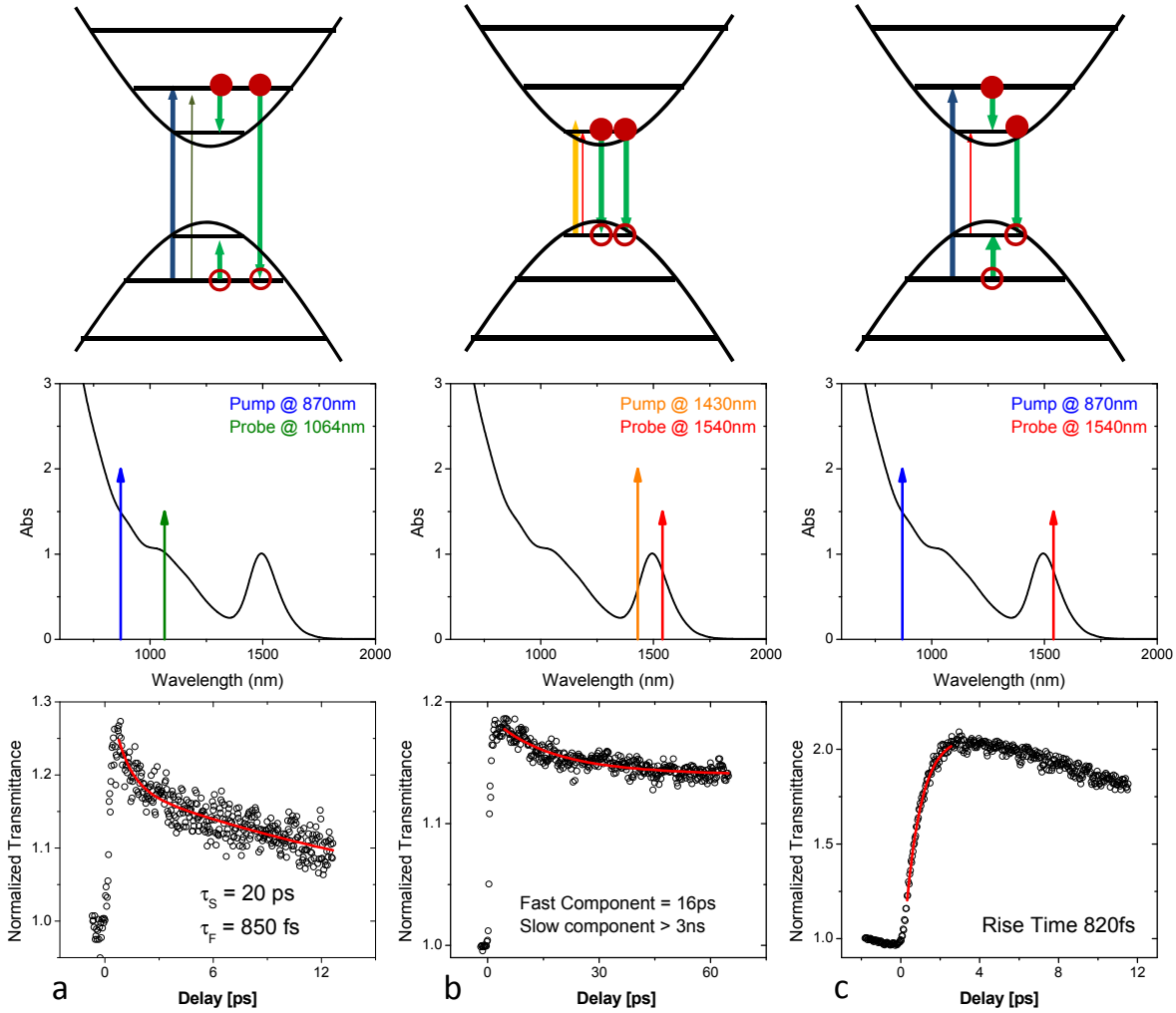

Figure 5-1: Pump-probe measurements of 3nm PbS QDs. In (a) The excitons are excited via the $1P_h \rightarrow 1P_e$ transitions and the P_h and P_e populations are monitored as a function of time. Then carriers are excited from the S_h into the S_e level (b) and the same population is probed. In (c) carriers are again excited into the 1P level and the population and subsequent depopulation of the 1S level is probed.

By exciting carriers with the strong pump beam into any of the QCLs and then probing at different energies and varying time delays, the excited state dynamics of the QDs can be investigated. The pump-probe technique introduced in Chapter 3.6 has the time resolution necessary to study these sometimes very fast relaxation times. By varying the pump and /or

probe wavelength the inter- and intra-band dynamics of the photo-excited carriers can be investigated. In Fig. 5-1 the pump probe traces for a sample of colloidal PbS QDs with average diameter of 3nm are shown.

5.1. *Intraband dynamics*

In order to investigate the intraband carrier dynamics, the pump wavelength is chosen to excite the carriers to high energy levels (at least 1P) and the probe is tuned to wavelengths resonant with the transition between QCL whose carrier dynamics are investigated. In the experiment shown in Fig. 5-1a and 5-1a, the carriers are excited with photons energetically just above the $1P_h \rightarrow 1P_e$ transitions. Once excited, the carriers will immediately (within the time resolution of the experiment) relax down to the 1P levels, this is evident from the immediate rise of the transmittance at zero delay. Once in the 1P QCL carriers relax on a picoseconds time scale. As mentioned before, for PbS, electrons and holes have the same effective masses and from now on we will discuss the dynamics of the electrons and assume that the same holds true for the holes. In Fig. 5-1a the probe is resonant with the $1P_h \rightarrow 1P_e$ transition and therefore the lifetime of carriers in the P levels is measured. Two distinct decays can be identified by fitting the electron dynamics from the $1P_e$ state with a double exponential decay of the form

$$T_{norm} = 1 + A_F e^{-t/\tau_F} + A_S e^{-t/\tau_S}. \qquad (5\text{-}1)$$

This double exponential decay is observed only for high numbers of electrons excited per QD. Two possible scenarios can explain this observation. The fast component (τ_F = 820fs) in Fig. 5-1a is attributed, in both scenarios, to carrier relaxation from the $1P_e$ ($1P_h$) to the $1S_e$ ($1S_h$) QCL. Since the 1S level in the lead salt QDs is 8-fold degenerate only a maximum of 8 electrons can

relax directly into the $1S_e$ state. Any carrier in excess of 8 in the 48-fold degenerate 1P levels must then decay through a different pathway. This channel is associated with the longer lifetime of τ_S = 20ps. Caruge et.al. [61] [Transient photoluminescence and simultaneous amplified spontaneous emission from multiexciton]and later others[62-64] have shown for CdSe QDs that direct $1P_e \rightarrow 1P_h$ radiative decay is possible if the two-fold degenerate $1S_e$ levels are saturated. Figure 5-2 shows an example of photoluminescence measured for CdSe/ZnS core-shell QD under pulsed (140 fs – FWHM) and CW excitation at 390 nm. The high density of electrons per QD created by the femtosecond pulse leads to filling of the 1S levels and therefore direct photoluminescence from $1P_e \rightarrow 1P_h$ can be observed, where in the case of CW excitation the filling of the 1S levels is negligible and photoluminescence is only observed from the first excited state. As shown by Klimov et.al. [65], the direct $1P_e \rightarrow 1P_h$ decay happens within 10's of picoseconds for CdSe QDs. A similar filling of the S levels and consequently direct $1P_e \rightarrow 1P_h$ radiative decay is conceivable for PbS QDs. However, the eight fold degeneracy of the 1S state in PbS should make the Auger depopulation of the 1S QCL faster and the long decay of the 1P level could also be attributed to the reoccupation of the 1S level by the remaining 1P electrons. Since in both scenarios the number of carriers which can relax via the initially unoccupied 1S level is given by the degeneracy of the 1S level, the ratio of carriers relaxing via the fast and the slow channel will change depending on the pump irradiance i. e., if less than 8 electrons are excited per QDs, all the electrons can decay via the fast channel, populating the 1S level, but if more than 8 carriers occupy the 1P levels some of them have to relax via the slow channel..

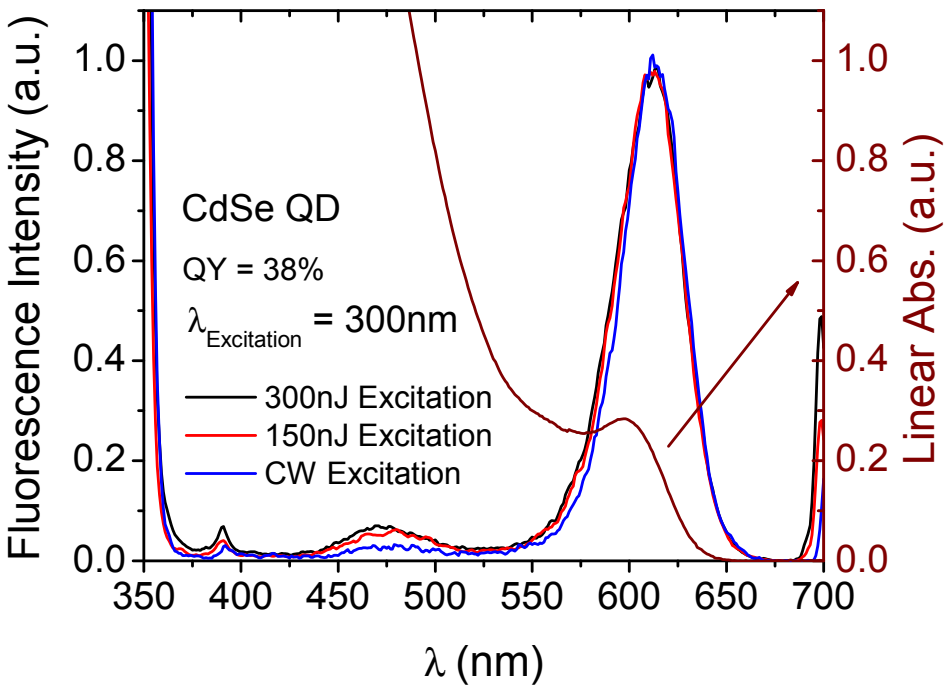

Figure 5-2: Linear absorption and fluorescence spectrum of a 3nm CdSe QD sample. The feature at 475nm is attributed to direct radiative carrier relaxation from the 1P levels.

Fig. 5-3 shows the 1P depopulation for PbS QDs excited with ~ 16 and 24 electrons per QD. The time constants τ_F and τ_S of the two relaxation channels as well as the number of carriers relaxing via the fast channel as expressed by the parameter A_F are independent of the pump energy. Only the contribution of the slow relaxation channel changes significantly as indicated by the parameter A_S. This parameter changes from 0.08 in the low energy experiment to 0.18 at high energy, indicating a larger fraction of excited carriers to relaxes via the slow relaxation channel.

A reasonable assumption is that the absorption cross section of an electron in a quantum confined 1P level is independent of the number of electrons in this level. Then Beer–Lambert's law ($I = I_0 10^{-OD}$) can then be written as

$$I = I_0 10^{-(48-N)OD_e}, \tag{5-2}$$

where 48 is the degeneracy of the 1P QCL, N is the number of excited electrons per QD and OD_e is the contribution to the optical density from a single electron in the QD ground state. Within this model the normalized transmittance can be expressed as a function of the average number of excited electrons per QD by

$$\frac{T_N}{T_0} = \frac{10^{-(48-N)OD_e}}{10^{-48\,OD_e}} = e^{N \cdot OD_e}. \tag{5-3}$$

Since the amplitude of the fast decay (A_F) represents the normalized transmittance of a QD with 8 excitons the parameter OD_e can be calculated from the fitting parameter A_F of 0.08 to be 4.18E-3.

$$\frac{T_8}{T_0} = 1.08 = 10^{8\,OD_e} \Rightarrow OD_e = \frac{\mathrm{Log}(1.08)}{8} = 4.18 \times 10^{-3} \tag{5-4}$$

With this value for the parameter OD_e the number of carriers at zero delay can be calculated. They turn out to 15.4 for 6μJ pump and24 for the 10μJ pump. The number of carriers which will have to decay via the slow channel are therefore 15.4 -8 = 7.4 and 24 – 8 = 16. The ratio of carriers relaxing via the fast and slow channel is 0.93 and 2 in good agreement with the ratio of the fitting amplitudes A_F/A_S of 1 and 2.25 for the 6μJ and 10μJ pump respectively.

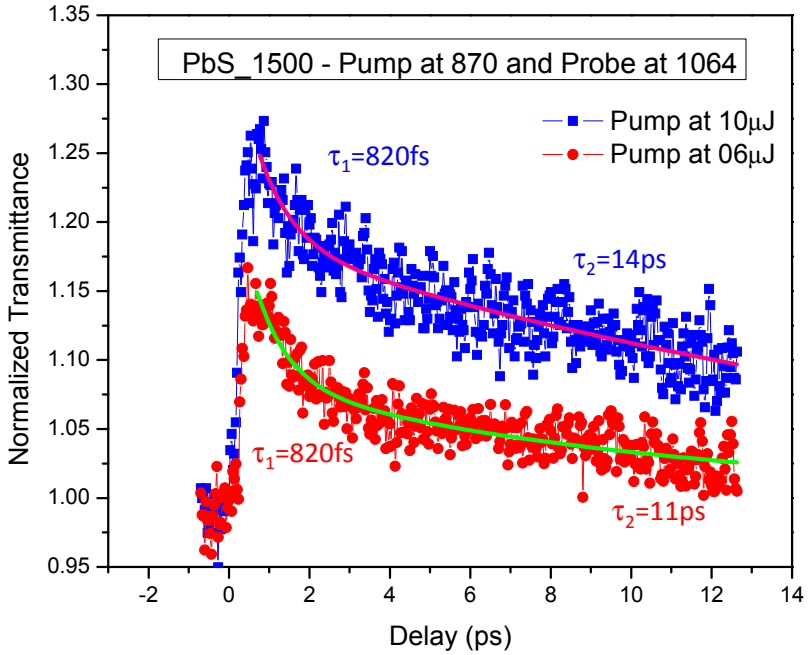

Figure 5-3: Pump probe experiment for a 3nm PbS QD. The red symbol is the normalized transmittance at 1064nm after the sample has been excited with a 6μJ Pump pulse at 870nm. The curve is fit with a double exponential decay (see Eq. 5-1) with the parameters $A_F = 0.08$, $\tau_F = 820fs$, $A_S = 0.08$ and $\tau_S = 11ps$ as indicated by the green line. The blue symbols are from an experiment with the same parameters except that the pump pulses have energy of 10μJ. The parameters for the exponential fit (red line) are $A_F = 0.08$, $\tau_F = 820fs$, $A_S = 0.18$ and $\tau_S = 14ps$.

Another way to observe the fast depopulation component of the 1P level, is to measure the rising population of the 1S level as the electrons pumped into the 1P level relax in to it (see Fig. 5-1b). This is achieved by pumping the $1P_h \rightarrow 1P_e$ transition and probing the $1S_h \rightarrow 1S_e$ transition.

Figure 5-4a shows examples of 1S population rising time for three different QD sizes. The results from shows that the smaller the QD, the faster the 1P→1S decay, even though the energy between the QCL is larger. The same trend has previously been observed for other QD structures, and in order to compare the lifetime of the carriers in the P levels to literature data for

different QDs [51], the energy loss rate calculated. The energy loss rate is defined as the energy difference between the quantum confined 1P and 1S level divided by the intraband relaxation time as determined from the exponential fit. These results are inconsistent with the expected so called “phonon bottle neck”. A “phonon bottle neck” [66] was expected in semiconductor QD because the energy separation between adjacent QCL is several times larger than the Longitudinal Optical (LO) phonon energy (27 meV for PbS) and therefore any phonon assisted relaxation would have to take place by simultaneous emission of several phonons making the process very unlikely and slow. However, the energy relaxation time as shown in Fig. 5-4b is found to be on a fast ps time scale and furthermore increases for smaller QDs where the phonon bottle neck should be strongest due to the larger energy separation between adjacent QCL. In the CdSe QD system, since the effective mass of the holes is much larger than of the electrons, the QCL in the conduction band are only weakly confined and in terms of phonon energy present a quasi-continuum. Therefore, the hole relaxation to the top of the valence band is very fast. The holes can then, in an Auger-like confinement enhanced e-h energy transfer, as proposed by Efros et al. [67] and Mikhailovsky et al. mediate the fast relaxation of the hot electrons without the need of multi phonon interactions. In PbSe QDs, on the other hand, the mirror like symmetry of the QCL in the conduction and valence band do not allow for the fast hole relaxation and consequently the e-h energy transfer mechanism is unlikely, and the intraband decay is slower than for CdSe, but follows the same size dependence. It was shown by Schaller et al. [51] that, at room temperature, the intraband carrier relaxation in PbSe is dominated by multi-phonon emission, which is more likely for smaller QDs due to the localized nature of the wavefunctions. This interpretation is justified by the temperature activated exponential increase of the carrier energy loss rate for temperatures higher than ~150K. However for temperatures lower than ~

150K the carrier relaxation rate stays constant, indicating that when the temperature is not high enough to activate the multi-phonon interaction, the Auger like process, like the one observed in CdSe QDs, may be the most important decay process. It therefore appears reasonable that an e-h Auger-type interaction is still present in PbSe and PbS QDs albeit small. Comparing the carrier relaxation rate from the almost perfectly symmetric QCL in PbS the somewhat less symmetric PbSe QD and finally the nonsymmetrical CdSe QDs we find a systematic increase in the carrier life time with increasing symmetry, which can be explained by the decreasing contribution of the Auger-like decay for more symmetric structures.

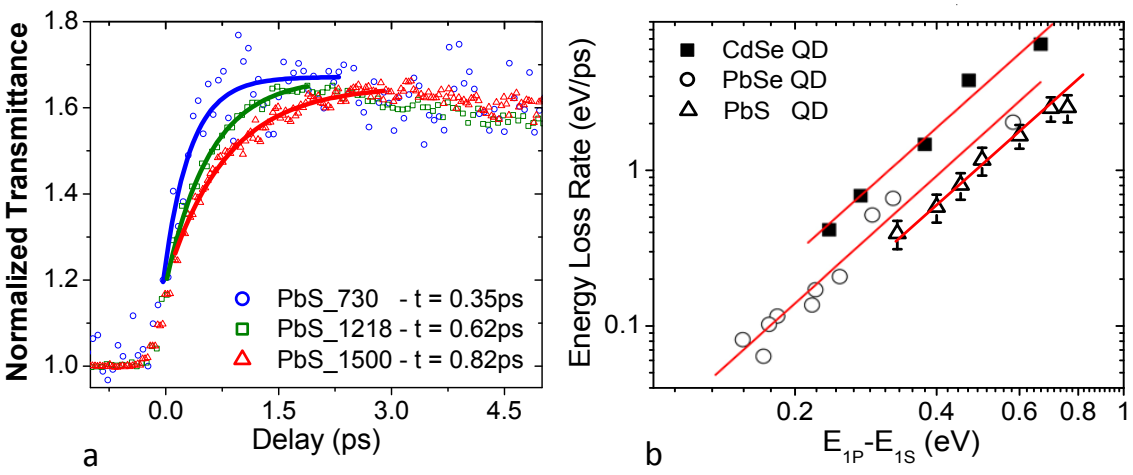

Figure 5-4: a) State filling dynamics of the S levels after carriers have been excited into the P levels for QDs of different size. b) Energy loss rate of PbS QDs compared to the energy loss rate of CdS and PbSe from the literature as a function of the P-S separation energy [51].

The spectrally resolved intraband dynamics is shown in Fig. 5-5. Carriers are excited into a higher QCL from where they relax very fast into the 1P level. The probe is than varied in wavelength and the time resolved excited state absorption spectrum is recorded. At early times (0.2ps delay) the $1P_h \rightarrow 1P_e$ transition is depleted most and carriers will then transiton towards the

quantum confined S levels. This is evident in the increasing depletion of the $1S_h \rightarrow 1S_e$ transition as time progresses (later delays) accompanied by a decreasing depletion of the P QCLs. It is even possible to make out some depletion at energies coinciding with the weak "parity forbidden" $1S_h \rightarrow 1P_e$ and $1P_h \rightarrow 1S_e$ transition.

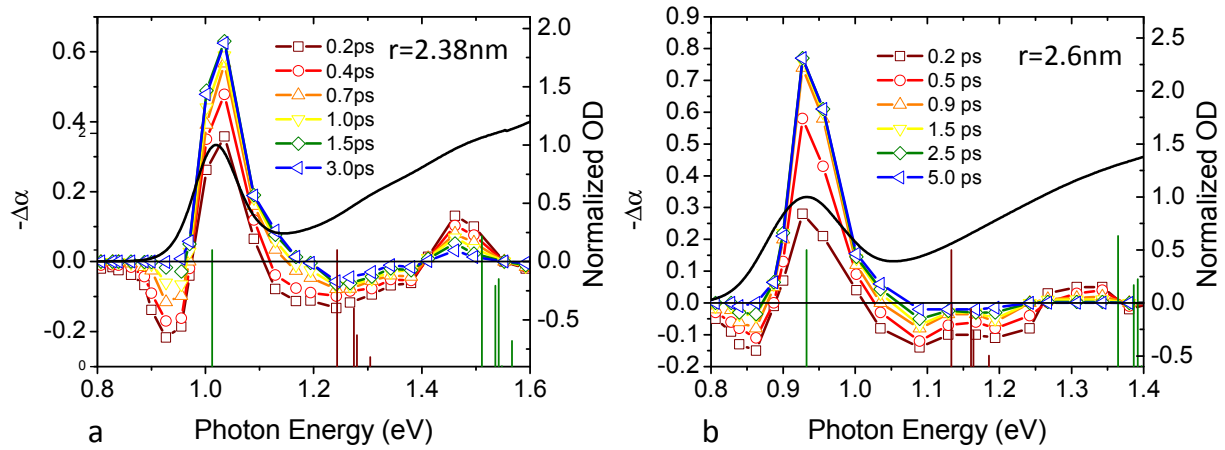

Figure 5-5: excited state spectra of PbS QDs with radius 2.38nm (a) and 2.6nm (b) at different times, shown as colored lines and symbols together with the normalized linear absorption (black line). Also shown are the transition as calculated by the **k·p** model for one and two photon absorption (green and red vertical lines respectively).

5.2. *Interband dynamics*

So far, this chapter has been focused on the intraband dynamics. By changing the pump as well as the probe wavelength the carrier dynamics of the quantum confined 1S level can be investigated (Fig 5-3c). Again the normalized transient absorption is fitted with a double exponential decay and two distinct time constants are found. A fast component of 16ps and a slow component for which, due to the limited range of the delay stage, only a lower limit of >3ns

can be extracted from the data (lifetimes of up to 2μs have been reported in the literature [68]. We interpret the data in strict analogy to what has previously been found in PbSe QDs [48]. For low pump energies the chance that a single QD absorbs more than one photon is negligible and therefore the maximum number of excitons per QD is one. In this case the dominant relaxation is by radiative decay. This is observed in the high fluorescent quantum yield of ~60% in PbS quantum dots [69] and the fluorescence lifetime of up to 2μs [68]. If the energy of the pump is increased above a certain level more than one exciton is created (on average) per QD. At this point the fast relaxation channel becomes observable. Unlike the fast component in the case of carrier relaxation out of the 1P levels, which is a constant with respect to the pump irradiance, the time constant of the fast relaxation out of the 1S level decreases for a greater numbers of excitons per QD. This is consistent with the Auger process whereby an excited electron recombines with a hole in the valence band by transferring its energy to a third particle in the 1S QCL which is therefore expelled from the 1S level. (see Fig. 5-6) [70-72].

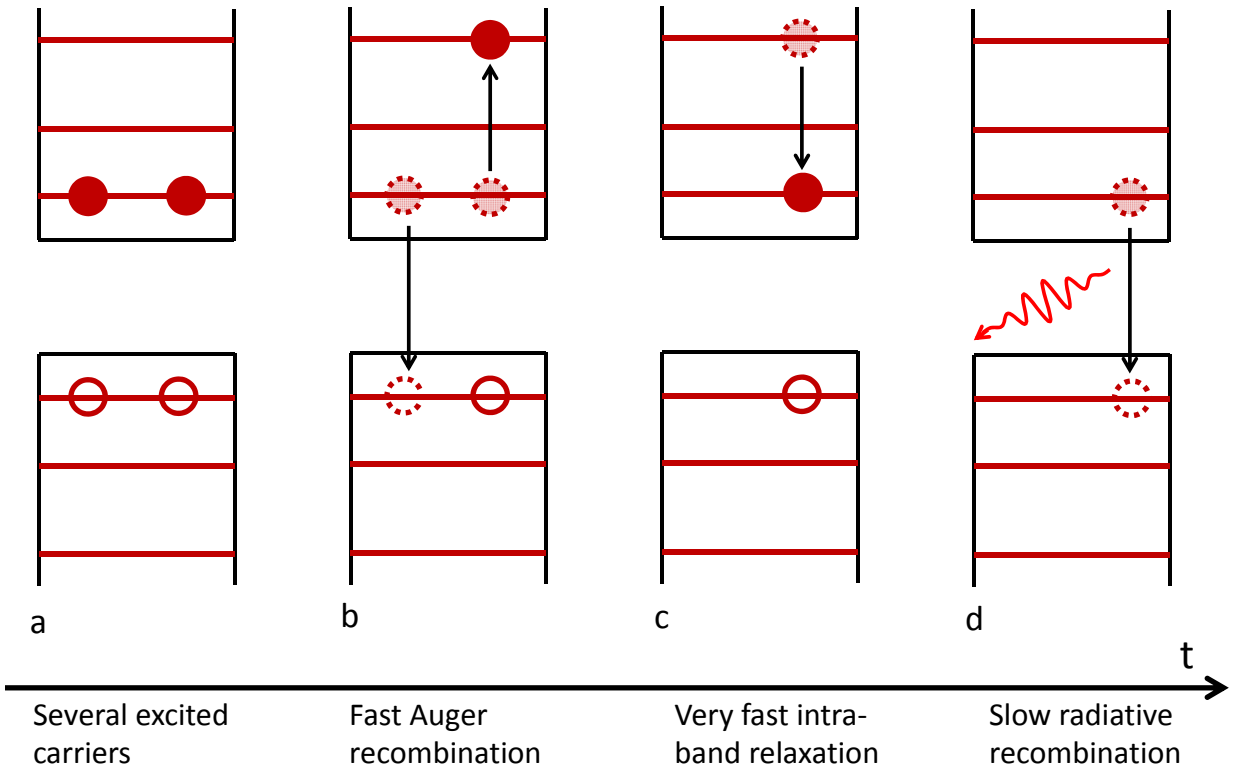

Figure 5-6: Auger recombination of carriers in The $1S_{e,h}$ QCLs.

Since we generally pump electrons into the higher lying P levels in order to take advantage of the greater optical density and degeneracy of these levels which makes it easier to generate high carrier densities, some time is required for these carriers to relax into the S level from which the Auger recombination is observed. The rate equations for the cascaded recombination are

$$\frac{dn_P}{dt} = -\frac{n_P}{\tau_P} \tag{5-5}$$

$$\frac{dn_S}{dt} = -\frac{n_S}{\tau_S} - c\, n_S^3 + \frac{n_P}{\tau_P} \tag{5-6}$$

where n_P and τ_P are the initial carrier density in the P QCLs and the time constant associated with the fast relaxation into the S level respectively. n_s and τ_s are the carrier density and time constant

associated with carriers in the S level and c is the Auger constant. This system of first order coupled differential equations has the solution

$$n_P(t) = n_0 e^{-t/\tau_P} \tag{5-7}$$

$$n_s(t) = \frac{n_0\left(1 - e^{-t/\tau_P}\right)e^{-t/\tau_s}}{\sqrt{1 + c\, n_0^2\, \tau_s \left(1 - e^{-t/\tau_P}\right)^2 \left(1 - e^{-2t/\tau_s}\right)}} \tag{5-8}$$

If we again make the assumption that the excited state absorption coefficient depends linearly on the number of excited carriers as in Eq. 5-2, it is easy to see that the change in the absorption coefficient is proportional to the number of excited carriers in the probed transition.

$$\frac{\Delta\alpha}{\alpha_0} \propto n_s \tag{5-9}$$

Therefore, Eq. 5-8 can be used to fit the data in Fig. 5-7. The common parameters are τ_P =300fs, τ_s = 1ns ($\tau_s >> \tau_i$) and a general proportionality parameter of 0.265. The time constant τ_S is much longer than the fast interband relaxation constant τ_P and is effectively set to infinity since due to the limitations of the delay stage its value cannot be determined. The Auger constant which gives the best fits (see Fig. 5-7) for all pump energies is then detriment to be c= 0.0075. This has to be scaled to the volume of the 2nm QD and therefore the Auger constant is 2.5×10^{-28} cm^6/s in agreement with the universal scaling of the auger constants found for other QD materials [73]. The remaining free parameter for the individual lines is the carrier density n_0. Fits as shown in Fig. 5-7a are achieved with n_i = 3, 1.9, 1.45, 0.78 for pump energies of 15μJ, 10μJ, 7.5μJ and 5μJ respectively. The extracted carrier densities are directly proportional to the pump energy, verifying the validity of the model (see Fig. 5-7b).

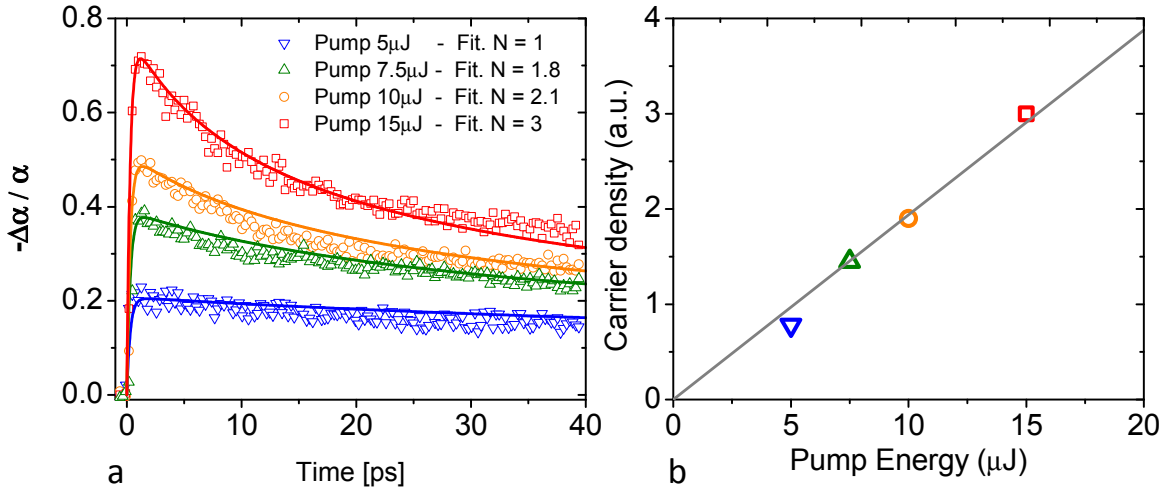

Figure 5-7: a) Carrier dynamics of the P levels after excitation with increasing pump energy. The fittings show the accelerating recombination with increasing carrier densities indicative of the Auger-mechanism. In (b) the carrier density as determined by the fittings versus the pump energy.

CHAPTER 6:
MULTI-EXCITON GENERATION

Multi-exciton generation (MEG) or carrier-multiplication (MC) is a process in which several Electron-hole pairs are created as the result of the absorption of a single photon. In an ideal case, under the limit of energy conservation, the threshold for multi-exciton generation (MEG) is $2\times E_g$ (where E_g is the energy of the QD's $1S_h$-$1S_e$ transition), and the minimum electron-hole pair creation energy is ε is E_g [74]. Here ε is defined as the energy loss of the ionizing particle during a secondary e-h creation proses and gives the slope of the increase in the CM quantum efficiency. This is shown in Fig. 6-1 where the maximum number of energetically allowed excitons is represented by the quantized step function (red) and the ideal under conservation of energy continues creation of excitons is the black line underneath the step function whose slope is the electron-hole pair creation energy ε. The region where MEG could possibly take place is shaded in gray.

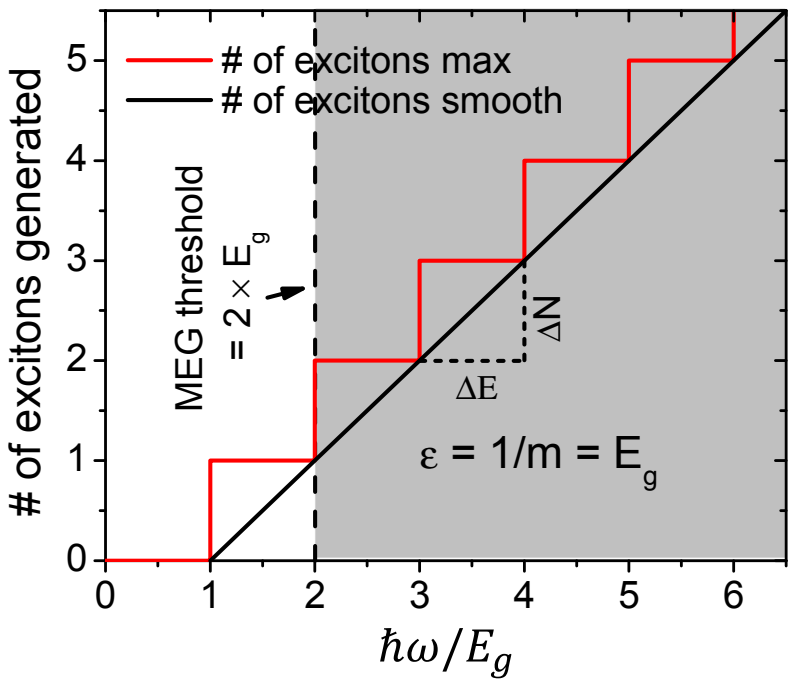

Figure 6-1: MEG under the limit of energy conservation. The red step function is the maximum number of excitons permissible due to energy conservation, while the experimentally observed smooth transition of increasing exciton generation. The gray shaded region is where MEG can take place.

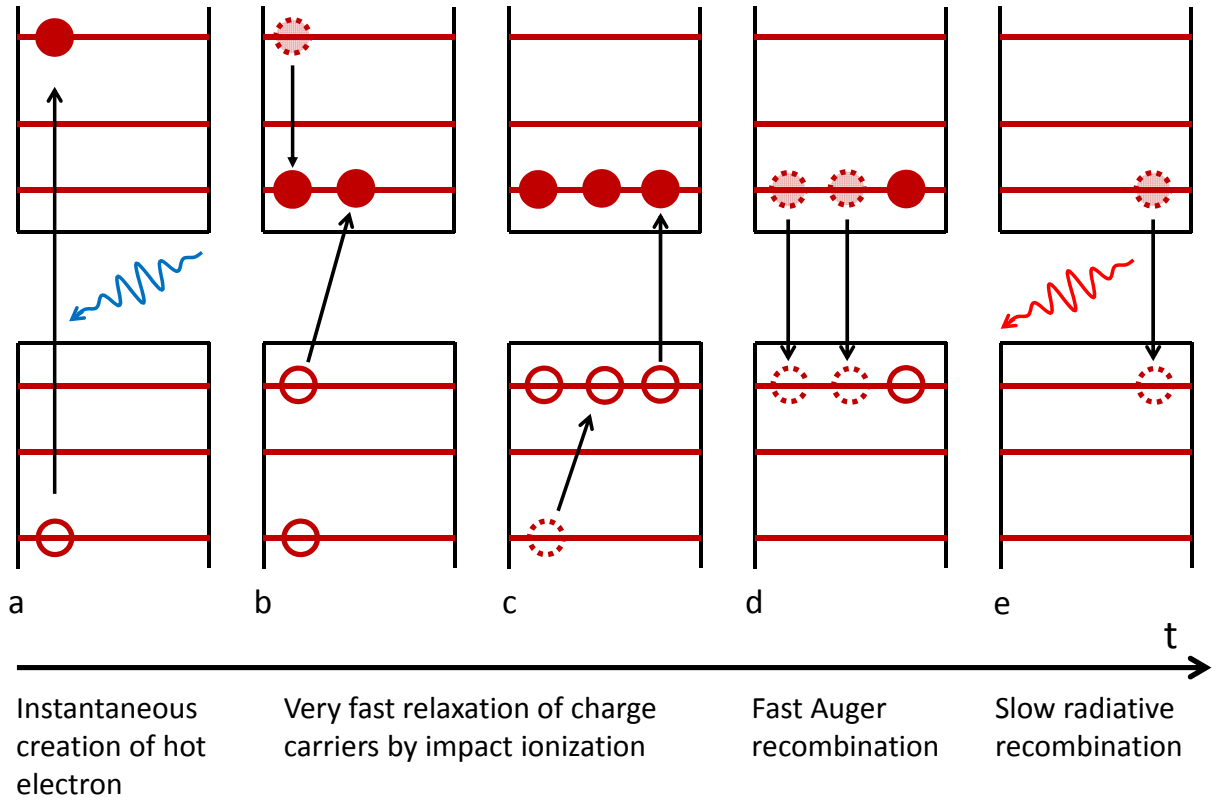

Figure 6-2: Creation and subsequent relaxation of excitons due to CM.

Under this ideal condition, Klimov et al. [75] have shown that an optimum single-junction solar cell could have conversion efficiency of up to 42%. The unique physics in QD and in particular the strong carrier interaction has stimulated much research into the possibility of enhancing MEG in semiconductor QDs. Some of the earlier reports had shown extremely high efficiency of carrier multiplication in several different species of QDs [] and quantum efficiencies up to 700 % was reported for PbSe QDs under UV irradiation [76]. However, more recent reports have shown that effects, like photo-ionization of the QDs can falsely lead to the apparent high CM signal [77]. Furthermore, the physical mechanism of CM in QDs remains under debate. In the impact

ionization process an electron is first excited to a high energy level and as it cools to the $1S_e$ level it transfers energy to a valence electron, which in turn is excited to the conduction band.

Despite extensive investigation of CM in several QDs structures, especially PbSe, little work has been reported on the more symmetric and isotropic PbS QDs. (to the best of our knowledge there are only few reports on PbS QDs and they do not investigate the size dependency of CM [78, 79].) We therefore investigate CM in several different sizes of PbS QDs, with band gap ranging from ~ 0.6 eV to ~ 1.3 eV, and compare the results to recently published studies of CM in bulk PbS [assessment of carrier nature].

The PbS QD samples for this study are prepared by the same method described in Chapter 4.1 and filled in 1mm quartz cell with optical density (OD) lower than 0.1 (typically ~ 0.05) at the $1S_h \rightarrow 1S_e$ peak. This is done to avoid strong depletion of the excitation beam at photon energies far above E_g where the absorption cross sections of the QDs is very high. The QDs one-photon absorption cross sections are calculated from the empirical method proposed by Cademartiri et.al. [49], which was previously described in Chapter 4.3.

The CM was investigated via pump probe experiments. For each sample, the probe wavelength is tuned to the peak of the $1S_h \rightarrow 1S_e$ transition and the pump is varied in order to investigate the CM at different photon energies. The experiments are performed at several different pump fluence, but in order to avoid multi-photon absorption per QD, only data for which the average number of absorbed photons per QD is less than 0.2 are used to calculate the MC efficiencies. If the fraction of QDs which have absorbed a photon is small compared to the fraction of QDs which have not absorbed a photon we can say with confidence that a negligible number (<2%) of QDs will have absorbed more than one photon, since the probability of absorbing a certain number of photons follows a Poisson distribution (see Fig. 6-3).

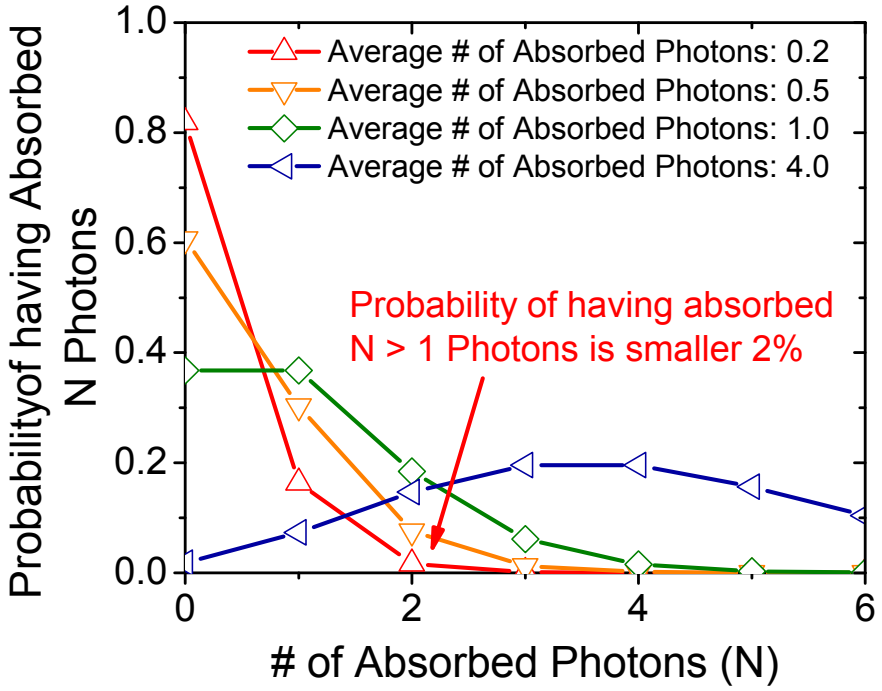

Figure 6-3: Probability of absorbing an integer number of photons as a result of an average number of photons absorbed per QD. For an average absorption of 0.2 photons per QD ≈ 82% of QDs will not have absorbed any photons, ≈ 16 % of QDs will absorbed exactly one photon and < 2% will have absorbed more than one photon.

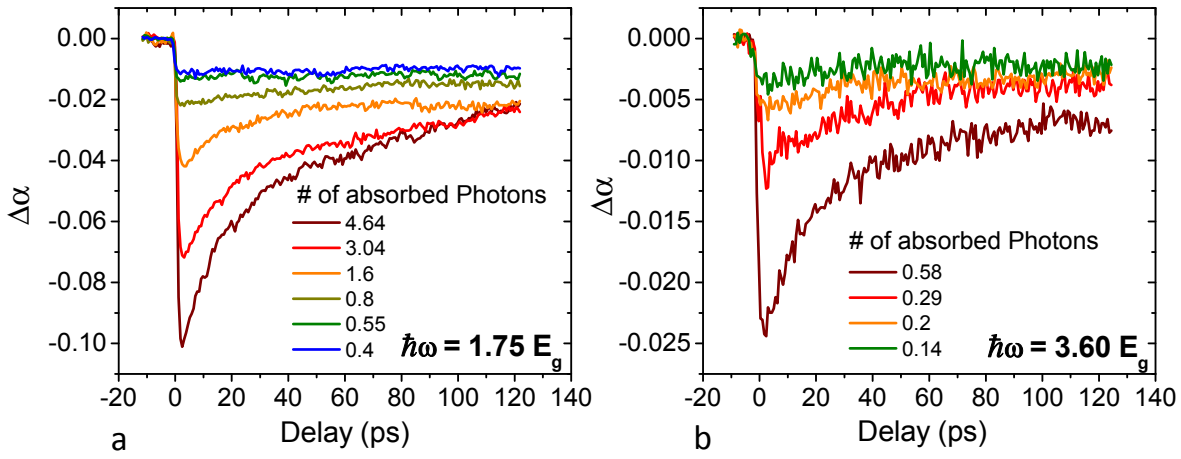

Figure 6-4: Transient absorption of a 2.5nm PbS QD. The $1S_h \rightarrow 1S_e$ transition is probed at 1400nm. The samples are pumped with photon energies corresponding to $1.75E_g$ (800nm) and $3.60E_g$ (390nm) in (a) and (b) respectively.

Figure 6-5 shows the CM efficiency for 5 different sizes of PbS QDs, with band gap range from 0.6 – 1.3 eV, and for bulk PbS, as measured in Ref. [80].

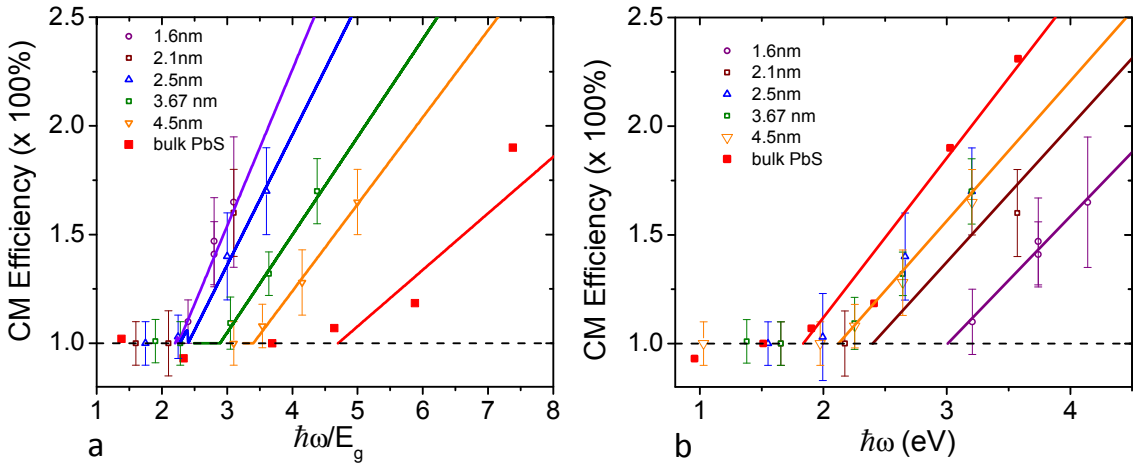

Figure 6-5: Carrier multiplication efficiency of PbS QDs with different sizes and bulk as a function of band gap normalized photon energy (bulk data from Ref [80])

The magnitude of the CM efficiency is obtained from the ratio of the transmittance at zero delay to the transmittance at a point in time where only one exciton remains (see Fig. 6-1e). The method is based on the observation, described in Chapter 5.2, that for QDs with more than one exciton in the S levels carrier relaxation takes place via the fast Auger process (see Fig. 6-1d). It is therefore possible to determine the fraction of QDs which have absorbed a photon verses the number of QDs which have not absorbed a photon from the long lived single exciton state in which all QDs will eventually be after all multi-exciton states have decayed via the fast Auger process. The maximum change in absorption around zero delay on the other hand is a measure of the total number of excitons created via MEG (Fig. 6-1a). The transient absorption curves (Fig. 6-4) are fitted numerically by slicing the sample into narrow regions to account for the beam depletion due to the high optical density especially at high photon energies. The number of photons absorbed per QD in each slice is calculated from which the ratio of absorption at early and later times can be calculated assuming a CM efficiency. By changing the CM efficiency, to reproduce the experimental values, the real CM efficiency of the sample is found. For each QD sample in Fig. 6-5a and b, the data above the CM threshold is then fit with a straight line. The inverse of the slope of the fits in Fig 6-5b gives the electron-hole pair creation energy, ε, and the CM energy threshold ($\hbar\omega_{th}$) is defined by the point where the fitting line intersects CM = 1. From the fits in Fig. 6-5a, we can see that $\hbar\omega_{th}$ continuously decreases from ~ $4.8\times E_g$ for bulk PbS until a plateau is reached very close to the theoretical limit of $2\times E_g$ for the smallest QDs.

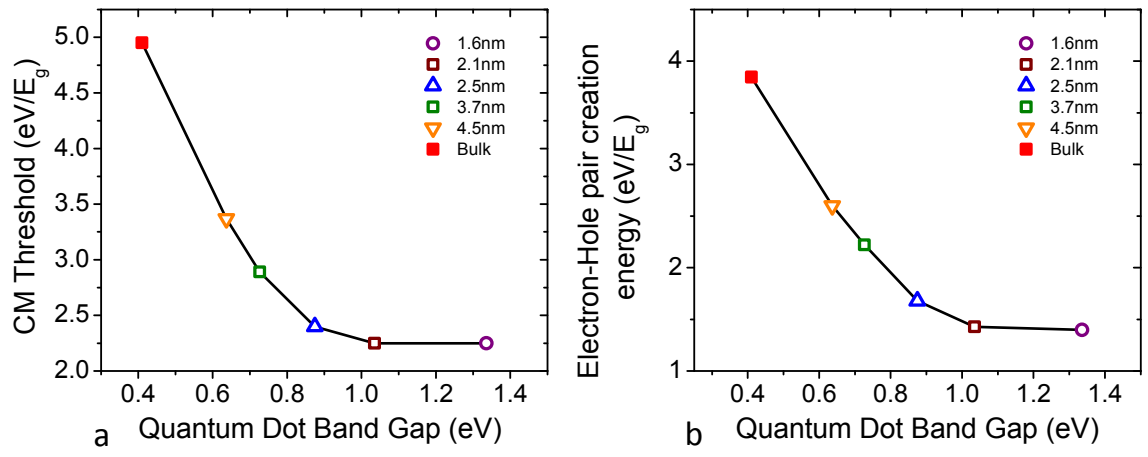

Figure 6-6: CM threshold and electron-hole pair creation energy versus the energy of the $1S_h \rightarrow 1S_e$ transition for a range of different size PbS QDs in (a) and (b) respectivaly.

Fig. 6-6a and b also shows the dependence of $\hbar\omega_{th}$ and ε on the QD size. The CM threshold changes from ~5×E_g to ~2.3×E_g and ε from ~ 3.8 E_g to ~ 1.5 E_g in bulk PbS to the smallest QD. If plotted in terms of absolute energy (eV units instead of multiples of E_g), as seen in Fig. 6-5b, the CM threshold is constant ~ 2.1 eV for for the bulk and the 3 largest QDs, increasing only for QDs with E_g > 1 eV. To the best of our knowledge, no rigorous theoretical studies of CM in PbS QDs are available. Several authors have reported on the possible causes for CM in QDs, but it is still controversial [74, 78, 81, 82]. Because of the very short time scale in which the CM takes place (sup 200 fs) [81], which seemed too short to be explained by impact ionization, many possible mechanisms have been invoked to explain the fast CM. The creation of a coherent superposition of single- and multi-exciton state due to the absorption of a photon with energy > $2E_g$ was proposed by Ellingson et al. [78], which than dephase on a short timescale into the multi-exciton state. Schaller et al. [81] have suggested that direct photogeneration of multi-excitons via virtual single-exciton states is taking place, explaining the observed dynamics.

Rupasov et al. from the same group [74] later proposed that CM in QDs predominantly take place via virtual biexciton states (a state of two electron-hole pares).

Due to the parity selection rules, the first possible biexciton state must involve three 1S levels and one 1P level, so the threshold for CM would be [74] $\hbar\omega_{th} = 2\ E_g + (E(1P_e\text{-}1S_e)$. For the case of PbS, $\hbar\omega_{th} \sim 2.22 \times E_g$ which agrees well with the limit measured for the smallest QDs ($\hbar\omega_{th} \sim 2.3\ E_g$). However, since we have shown (see chapter 4.2) that the parity selection rules in small lead-salt QDs are not valid this argument might have lost some of its power. On the other hand, Franceschetti et.al. [82] have theoretically predicted that, for PbSe QD, the impact ionization for photon energies higher than 3 eV can be as fast as 20 fs and, by comparing the density of states for exciton and biexciton states, they show that, via impact ionization only, the threshold for CM in PbSe with 1.55nm in radius is ~ 2.3 E_g, which again is in very good agreement with experimental findings. Currently a consensus seems to be forming and impact ionization is considered to be the most probable mechanism for CM in QDs. In the impact ionization process an electron is first excited to a high energy level and as it cools to the $1S_e$ level it transfers energy to a valence electron, which in turn is excited to the conduction band (see Fig. 6-2 a to b to c). Even though these impact ionization predictions are for PbSe and not for PbS QDs, we expect that the results for PbSe QDs can be generalized to PbS QDs of the sizes studied here. This is due to the similar intraband and interband energies, as well as the comparable density of states. For the same band gap, PbS and PbSe QDs should have very similar CM efficiencies. Figure 3 shows our data for PbS QDs compared to the tight-binding calculations of CM (considering only impact ionization) for PbSe QDs with E_g = 0.6 eV and 1.2 eV. We find remarkable agreement between our experimental results and the predicted for PbSe, indicating that the theoretical predictions are valid. The measured energy threshold also agrees well with predictions by both,

direct biexciton generation and impact ionization, but the good agreement with the impact ionization model suggests that there is no need to invoke exotic processes like the superposition of single- and multi-exciton states or virtual single- or bi-exciton states to explain CM in QDs.

The scarce density of allowed transitions between the almost mirror symmetric QCL of the valence and conduction band in PbS and PbSe QDs would shift the CM threshold towards higher energies, if the strict selection rules from a simple $\boldsymbol{k \cdot p}$ model are valid. This is because in order to promote an electron from the top of the QCL in the valence band to the lowest QCL in the conduction band any hot electron (or hole) would have to reside at least $1\times E_g$ above (below in the case of the holes) of the lowest QCL in its respective band. Due to the selection rules in the lead salt QDs transitions which result in these conditions require photon energies of $\sim 3\times E_g$. However, in Chapter 4.2, we have shown experimentally that the parity of the wavefunctions in PbS and PbSe QDs is broken, so that one-photon absorption transitions between states with the same parity are allowed. Therefore an electron can make a transition from the $1S_h$ QCL to the $1P_e$ QCL and then relax to the $1S_e$ QCL by promoting a second electron to the same level. This could favor the shift of $\hbar\omega_{th}$ towards the energy conservation limit of $2 \times E_g$.

The results shown in Fig. 6-5 were obtained from TA measurements in static QDs (no stir or flow cell was used). McGuire et.al. [77] have shown for some PbSe QDs, a large difference in apparent CM efficiency between static and stirred QDs sample, especially under UV excitation. Apparent CM efficiency of up to ~ 50% higher in static sample (as compared to the stirred ones) are measured with TA at 1 kHz repetition rate, and up to 300 % higher CM is measured in static samples by up-converted photoluminescence (uPL) with 250 kHz repetition rate when compared to a stirred sample [77]. The larger apparent CM efficiency has been attributed to cumulative photo-ionization of the QDs, which is expected to be long lived (at least few ms) and dependent

on the pump photon energy and on the sample investigated. In order to rule out the influence of any long lived process in our CM signals we have performed several tests:

1) We verified the absence of a buildup of the transmittance when the delay is set such that the probe precedes the pump pulse (negative time delay). Long lived photo ionization (> 10ms) should accumulatively decrease the linear absorption of the QD, leading to increased transmittance of the probe beam due to the presence of the pump, even for negative time delays. No measurable changes in the linear transmittance of the probe, due to presence of the pump, were observed suggesting that if there is photo-ionization for the samples investigated, the effect should be small.

2) Assuming that the lifetime of the photo-ionized QD is between 1 – 10 ms, a change of the pump repetition rate would change the CM efficiency signal if a significant amount of QDs are ionized, however, by changing the laser repetition rate from 1 kHz to 500 Hz, no measurable difference on the TA signal was observed.

3) As a third test, for the smallest QD (PbS-930, E_g = 1.33 eV), with the lowest CM threshold, we performed TA studies while flowing the suspension and compare the results to the static case. The flow cell (1 mm x 10 mm) was set to a flow rate of ~ 600 ml/min. Whether the flow in the cell is laminar or turbulent is indicated for the flow cell dimensions and the flow rate by the Reynolds number. Reynolds number is calculated for a wide duct by Eq. 6-1 [83]

$$R = \frac{\rho v D_H}{\mu} \tag{6-1}$$

Where ρ is the density, v the average velocity, D_H the hydraulic diameter and μ is the viscosity. These parameters for the flow cell geometry and the flow medium (toluene) are: $\rho=0.8669\times10^3$ kg/m^3, v=1m/s, D_H=2mm and $\mu=0.59\times10^{-3}$ Pa·s. The hydraulic diameter for a

wide duct is 2 times the separation of the slabs (2×1mm) [Introduction to Fluid Mechanics]. For Reynolds number < 2300 the flow is laminar and for Reynolds number >4000 the flow is purely turbulent [84]. In the flow geometry used in the experiment the Reynolds number is calculated to be 2939 by Eq. 6-1. This indicated that we are right at the edge of purely laminar flow. We therefore can use the equation of motion for a Newtonian fluid (Eq. 6-2).

$$\nabla^2 v = \frac{1}{\mu}\nabla p \qquad (6\text{-}2)$$

Since the pressure gradient in a channel of constant cross-section has to be uniform turnout Eq. 6-2 simplifies to $\nabla^2 v = c$. This is still complicated to solve in two dimensions[85, 86], but since we are only interested in the velocity profile in the center of the flow cell the problem can be reduced to a one dimensional problem in the direction of the narrow dimension of the duct. The solution is

$$v(x) = \frac{c}{2}(x - x^2), \qquad (6\text{-}3)$$

where the constant c is calculated by integration Eq. 6-3 over the cross-section of the cell and equating it with the flow rate (600mL/S) to be 12(1/m·s)

The pump and probe beams are centered on the cell (in the vertical axis), where the flow velocity is the highest. In order to avoid any cumulative effect, it is necessary that each QD leaves the pump and probe volume in less than 1 ms (laser rep rate of 1 kHz), and for our flow conditions this is reached ~ 30 μm from the surface of the cell. This is shown in Fig. 6-7 where the velocity profile of a laminar flow in the geometry of the flow cell as calculated by Eq. 6-3 is divided by the diameter of the probe to estimate the time it takes replace the volume exposed by a single pump pulse. Only within a narrow layer as indicated by the gray regions, is the volume not replaced before the next pump pulse arrives. For most of the probed sample the volume is

replaced before the next pump pulse arrives no accumulative effects are to be expected. We also need to consider the depletion of the pump beam due to the high optical density especially at high photon energies (OD ~ 2.0). Only on the front face of the sample is the pump strong while its effect can be neglected on the back surface. Based on the optical density and flow dynamics, we estimate that about 10 % of the QDs, can possibly be hit by more than one pump pulse.

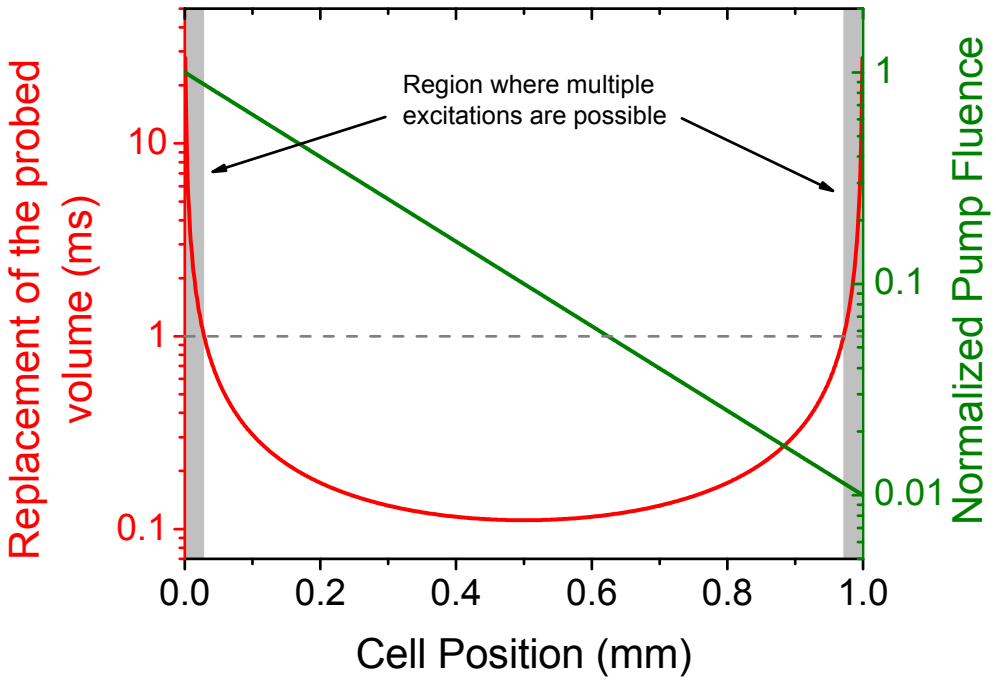

Figure 6-7: Time it takes to replace the volume of the QDs exposed to the pump beam (red curve). Also shown is the depletion of the pump as it travels thorough the sample assuming a optical density of 2 (green line)

Figure 4 shows a comparison between the results obtained for the sample PbS-930 in the static and flowing situation (pump at 390 nm). No significant difference is observed, indicating that, if photo-ionization is influencing our CM results, this phenomenon should not account for more than ~ 10% of our CM signal. The result from the flow cell experiment together with the

other tests described above suggests that our results are free of the influence of photo-ionization (at least within our experimental error).

McGuire et.al. [87], have proposed a model to correct the apparent CM efficiency due to photo-ionization, in uPL experiments, assuming that the charging of the QDs does not change the CM efficiency. Based on this model, we can estimate the real CM efficiency measured in a TA experiment under the presence of photo-ionization. Using the method proposed by McGuire et.al. [87], we obtain that

$$\eta_{App} = (1+\eta)\frac{1+{}^{f}/_{7}}{1-f} - 1,$$

where η_{App} and η are the apparent and real CM efficiency and f is the fraction of charged QDs. Comparing the flown and static measurements we see no difference (within the noise) between the long delay TA signal for the static and flown sample, and we estimate that the charging does not affect more than 10% of the QDs. So if we assume that ~5-10% of the QDs studied here are influenced by photo-ionization, the real CM efficiency for the 1.6nm PbS QD pumped at 4.1 eV would be 1.56 ± 0.05 instead of 1.67, which this is accounted for by our experimental error bars.

The results of the CM in QDs are promising characteristic for applications in photovoltaic. However, for such devices, colloidal QDs in liquid suspensions are undesirable and solid state samples would need to be used. Using a solid exchange technique as described in Ref [88], we prepare thin films of QDs and investigate their CM. In short, the solid exchange method substitute the QDs oleic-acid ligand with ethanedithiol, during spin coating on to a planar glass substrate linking the QDs into a rigid matrix. This technique only results in good quality films for small PbS QDs with band gap larger than ~ 1.2 eV [88], and so we were able to prepare films

only from the smallest QDs 1.6nm sample. Figure 6-8 compares the TA signal for the solution to the thin film.

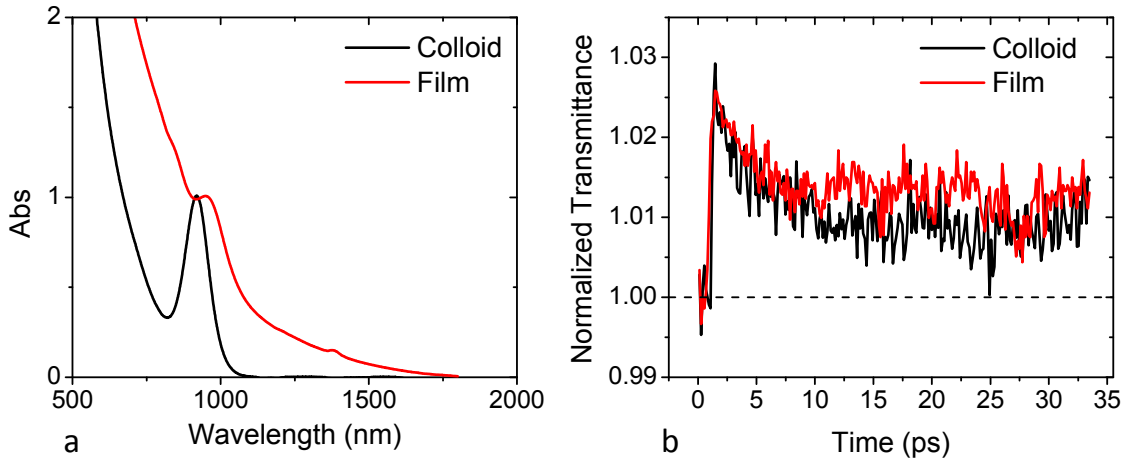

Figure 6-8: (a) linear absorption of 1.6nm PbS QD in solution and as film. (b) TA of samples shown in part a. Both samples are pumped with 380nJ at 300nm. The probe wavelength is set to match the absorption peak of the colloid and the film at 925nm and 950nm respectively.

The measurements were performed under the same experimental conditions and show that, for pumping at $\hbar\omega$ = 4.1 eV (300nm), the CM for the film sample is ~ 1.4 while for the solution based it is 1.67. Also, measurements done at lower photon energies shows that the CM threshold for the film is higher than for the solution based QD (for $\hbar\omega_{th} = 2.4\ E_g$ no CM was observed for the film, different to what is shown in Fig. 6-5 for the solution based 1.6nm sample). Since it is a solid sample, no stirring or flowing is possible hence only the first two methods discussed above could be used to test for photo-ionization of the QDs. It is therefore possible that the measurements are affected by photo-ionization and the actual CM efficiency might be even smaller than 1.4 for pump photon energies of 4.1 eV. As discussed in Ref. [89] different surface properties are expected to influence the CM in QDs and is therefore possible that films prepared

from other ligand might not show the reduced CM efficiencies. However a better understanding of this influence is necessary and will have to be part of future work.

The low CM threshold together with the low electron-hole pair creation energy is ε in PbS QDs are very promising characteristics for their use in third-generation photovoltaic devises. However, due to the nature of the CM one necessarily ends up with multiple carriers in a single QD and therefore the Auger recombination process will remove excited carriers very fast. In order for carries to contribute to a photocurrent they would therefore have to be captured equally fast.

CHAPTER 7:
CONCLUSIONS

In this dissertation the properties of lead salt QDs were studied. Several optical methods have been implemented to gain a better understanding of the one- and two-photon absorption as well as the excited state dynamics of these QDs. A four-band envelope function model was adapted to calculate the positions and oscillator strengths of the two-photon transitions. The results are compared to the experimentally determined two-photon cross-sections as measured by Z-scan or 2PF in the degenerate case or by pump-probe measurements for the non-degenerate case. Good agreement is found between the experimental data and the model in terms of transition energies as well as for the relative magnitudes of degenerate and non-degenerate transition strengths. Despite the good predictive power of the model for the lowest energy one- and two-photon transitions some features observed in the linear spectrum are not predicted by this theory. Other models, which were discussed in this work , consider the anisotropy of the electronic band structure to predict some of the missing features for the PbSe QDs, but to our knowledge this approach does not work for the more isotropic PbS materials. Moreover, none of the models predicts 2PA at the energy of the first one photon transition which was observed in this work. This problem can be solved by relaxation of the selection rules. The experimentally verified occurrence of 2PA at the energy of the $1S_h \rightarrow 1S_e$ transition is viewed as strong evidence in favor of the symmetry breaking argument and possible physical reasons are given to justify this interpretation.

The time dynamics in PbS QDs has also been investigated and analyzed in analogy to the better studied PbSe QDs. It was found that the same physical models apply and that the relaxation

times are comparable but generally longer than in PbSe. This has been explained by the more symmetric band structure of PbS compared to PbSe and CdSe.

Finally the multi-exciton generation, MEG, efficiency in PbS QDs was measured. We found that the threshold for MEG has a clear QD size dependence and for the smallest QDs studied the threshold is 2.3 E_g, very close to the theoretical limit of $2E_g$. We also found a clear shift of the electron-hole pair creation energy with the change in QD size. The results agree well with theoretical predictions for impact ionization in PbSe QDs, which are similar in band structure to the PbS QDs studied here, suggesting that no other processes needs to be invoked to explain CM in these materials. The amount of possible QD charging was also investigated, showing no measurable influence on our results. Finally, CM in films prepared from small PbS was investigated and similar but somewhat less favorable results compared to the colloidal samples were found.

APPENDIX A:
INSTRUCTIONS FOR THE MATHCAD PROGRAM

In this section a step by step instruction to operate the Mathcad code to calculate the energy and oscillator strength for the QCLs in lead salt QDs is given. The code is based on the ***k·p*** model outlined in Chapter 2.3. The intent is to enable a person, even though he or she might not be familiar with the details of the formalism, to operate the program. Parameters which require the user input are framed and highlighted in red. The results are highlighted in green and can be exported in the usual copy and paste manner. In order to monitor the progress of the calculation the trace window should be made visible and the debugging mode activated.

First the user is required to choose the material either, PbS ore PbSe, and the radius (in nm) of the QD.

PbX := "PbS"

a := 1.775

In section "Energies of 1 Photon transitions" the energies of the one-photon transitions are calculated The input parameters for the function "M1Ph_unsorted(2, 3, 2, 3, a)" are set by default to 2, 3, 2, 3 and *a* where *a* is the radius of the QD defined in the first step and the numbers 2, 3, 2 and 3 are the heist quantum number for which transitions are calculated in the order of n_v, l_v, n_c, l_c. This leads to 80 distinct transitions which should be enough for most cases. While it is possible to have the program calculate transitions with higher quantum numbers this transitions will accrue at k values outside the range for which the approximations made in the model are valid.

The transitions are then sorted according to their energies and a range of transitions in order of their energy is selected. (in the interest of time only transitions of interest to the should be selected)

first1ph := 0 last1ph := 3

The index starts at 0 for the transition with the lowest energy. The output is a matrix which contains the quantum numbers of the transitions n_v, l_v, j_v, π_v, n_c, l_c, j_c, π_c in column 0-7. The the energy of the transition (E_{Trans}) followed by a place holder for the transition strength which will be calculated in a later step, is found in column 8 and 9. This pace holder is set to one for all transitions. Finely the values for k_v and k_c are in the last two matrix entries.

M1Ph =

	0	1	2	3	4	5	6	7	8	9	10	11	12	13	14
0	1	0	0.5	1	1	0	0.5	-1	1.3628965628	1	1.6138436793	...			

The transitions in "M1ph" will be used in a second step to calculate the oscillator strength.

In order to calculate the transition strength go to "Calculate 1 or 2 photon transitions for single Dot" and enable the calculation of "OS1Ph(M1Ph,a)" by right clicking the field and then choosing "enable evaluation"

OS1Ph(M1Ph, a) =

The result will be the same matrix than in the previous section but with the transition strength in column 9.

For the calculation of the two-photon transitions the same procedure is to be followed.

First in section "Energies of 2 Photon transitions" of transitions to be calculated is chosen in the red fields for the first and the last two-photon transition

first2ph := 0 last2ph := 3

The result is displayed in matrix from

M2Ph =

	0	1	2	3	4	5	6	7	8	9	10	11	12	13	14	15
0	1	0	0.5	1	1	1	1.5	1	.7354252669	1	.6138436793	...				

This results are than used to calculate the 2PA strength in section "Calculate 1 or 2 photon transitions for single Dot" by activating the evaluation of

OS2Ph(M2Ph, a, ni_max, li_max) =

The only difference, compared to the calculation of the 1PA, is that the program requires information about the number of intermediate states to be used. This is provided by specifying the maximum values of the quantum numbers (n_i and l_i) for this states.

ni_max := 4 li_max := 6

Since the section rules for this system are such that any transition with $\Delta m > \pm 1 = 0$ the maximum of the quantum number l_i must not exceeded the heist l of the initial and final state. (Lager values for l_i will not change the results, but will slow the calculation)

Alternatively the transitions are calculated for a range of QDs with different radii. This is done for one-photon transitions in section "Calculate 1 photon transitions for range of Dots" and for two-photon transitions in "Calculate 2 photon transitions for range of Dots".

The input parameters for the 1PA calculations are

r_min_1Ph := 3.375 r_max_1Ph := 3.375 del_r_1Ph := 0.1

first_1Ph := 0 last_1Ph := 5

Where r_min_1Ph is the radius of the smallest QD and r_max_1Ph is the radius of the largest QD. del_r_1Ph specifies the step size of the radius. In its current version the program only calculates the energies of the one-photon transition as a function of the QD size and not the transition strength. (The user is encouraged to extend the capability of the program to include the

oscillator strength.) The results again are presented presents in matrix form, where the first column contains the radius of the QD and the energies of the transitions are followed in increasing order with place holding zeros for the oscillator strength.

Calculate 1Ph transition energy only

$$\text{MEofR1Ph}(r\_min\_1Ph, r\_max\_1Ph, del\_r\_1Ph, first\_1Ph, last\_1Ph) = \begin{pmatrix} 3.375 & 0.7569654597 & 0 & 1.0452179134 & 0 & 1.0596284502 \\ 3.475 & 0.741305118 & 0 & 1.0170104563 & 0 & 1.0307014237 \\ 3.575 & 0.7267351917 & 0 & 0.990798944 & 0 & 1.0038127971 \\ 3.675 & 0.713152131 & 0 & 0.9663868604 & 0 & 0.9787631819 \end{pmatrix}$$

Two photon transition energies are calculated either with the corresponding oscillator strength or, in the interest of computation time, without.

The input parameters are the same as for the one-photon transitions with the edition of the intermediate state quantum numbers n_i and l_i.

r_min := 3.375 r_max := 3.375 del_r := 0.1

first := 0 last := 5

ni_max := 5 li_max := 5

The results are presented in the same way as for the one-photon transitions, but contain the oscillator strength in place of the zeros, if so chosen.

Calculate 2Ph transition energy only

$$\text{MEofR2Ph}(r\_min, r\_max, del\_r, first, last, ni\_max, li\_max) = \begin{pmatrix} 3.375 & 0.8916833756 & 0 & 0.9098738375 & 0 & 0.9104999975 \\ 3.475 & 0.8702461239 & 0 & 0.8875425209 & 0 & 0.8880694505 \end{pmatrix}$$

LIST OF REFERENCES

1. Wundke, K., et al., *PbS quantum-dot-doped glasses for ultrashort-pulse generation.* Applied Physics Letters, 2000. **76**(1): p. 10-12.

2. Nozik, A.J., *Quantum dot solar cells.* Physica E-Low-Dimensional Systems & Nanostructures, 2002. **14**(1-2): p. 115-120.

3. Shnirman, A. and G. Schon, *Quantum measurements performed with a single-electron transistor.* Physical Review B, 1998. **57**(24): p. 15400-15407.

4. Ustinov, V.M., *Quantum dot lasers*. Oxford science publications. 2003, Oxford: Oxford University Press. ix, 290 p.

5. Larson, D.R., et al., *Water-soluble quantum dots for multiphoton fluorescence imaging in vivo.* Science, 2003. **300**(5624): p. 1434-1436.

6. Hook, J.R. and H.E. Hall, *Solid state physics*. 2nd ed. The Manchester physics series. 1991, Chichester ; New York: Wiley. xxi, 474 p.

7. Kelly, K.L., et al., *The optical properties of metal nanoparticles: The influence of size, shape, and dielectric environment.* Journal of Physical Chemistry B, 2003. **107**(3): p. 668-677.

8. Efros, A.L. and A.L. Efros, *Interband Absorption of Light in a Semiconductor Sphere.* Soviet Physics Semiconductors-Ussr, 1982. **16**(7): p. 772-775.

9. Brus, L.E., *A Simple-Model for the Ionization-Potential, Electron-Affinity, and Aqueous Redox Potentials of Small Semiconductor Crystallites.* Journal of Chemical Physics, 1983. **79**(11): p. 5566-5571.

10. Gammon, D., et al., *Homogeneous linewidths in the optical spectrum of a single gallium arsenide quantum dot.* Science, 1996. **273**(5271): p. 87-90.

11. Kilina, S.V., et al., *Ab initio time-domain study of phonon-assisted relaxation of charge carriers in a PbSe quantum dot.* Journal of Physical Chemistry C, 2007. **111**(12): p. 4871-4878.

12. Wang, L.W. and A. Zunger, *Local-Density-Derived Semiempirical Pseudopotentials.* Physical Review B, 1995. **51**(24): p. 17398-17416.

13. M. L. Cohen, J.R.C., *Electronic Structure and Optical Properties of Semiconductors, Solid State Sciences*. 1988, Berlin: Springer.

14. Kang, I. and F.W. Wise, *Electronic structure and optical properties of PbS and PbSe quantum dots.* Journal of the Optical Society of America B-Optical Physics, 1997. **14**(7): p. 1632-1646.

15. Lowdin, P.O., *Studies in Perturbation Theory .X. Lower Bounds to Energy Eigenvalues in Perturbation-Theory Ground State.* Physical Review, 1965. **139**(2A): p. A357-&.

16. Stier, O., *Electronic and optical properties of quantum dots and wires*. 2000, Berlin Wissenschaft & Technik Verlag.

17. Altarelli, M., *Band Structure, Impurities and Excitons in Superlattices, Heterojunctions and Semiconductor Superlattices*, ed. Allan. 1986, Berlin: Springer.

18. Kane, E.O., *in Handbook on Semiconductors*, ed. W. Paul. Vol. 1. 1982, Amsterdam North Holland.

19. Mitchell, D.L. and R.F. Wallis, *Theoretical Energy-Band Parameters for Lead Salts.* Physical Review, 1966. **151**(2): p. 581-&.

20. Marcuse, D., *Principles of quantum electronics*. 1980, New York: Academic Press. xvi, 494 p.

21. Kienberger, R., et al., *Atomic transient recorder.* Nature, 2004. **427**(6977): p. 817-821.

22. Arecchi, F.T., et al., *Laser handbook*. Vol. 2. 1972, Amsterdam, New York,: North-Holland Pub. Co.; American Elsevier Pub. Co.

23. Strickland, D. and G. Mourou, *Compression of Amplified Chirped Optical Pulses.* Optics Communications, 1985. **56**(3): p. 219-221.

24. De Silvestri, S., G. Cerullo, and G. Lanzani, *Coherent vibrational dynamics*. Practical spectroscopy. 2008, Boca Raton, FL: CRC Press. xv, 267 p.

25. Stegeman, G., *Nonlinear Optics Class Notes*. 2006.

26. Brewer, R.G., *Frequency Shifts in Self-Focused Light.* Physical Review Letters, 1967. **19**(1): p. 8-&.

27. Shimizu, F., *Frequency Broadening in Liquids by a Short Light Pulse.* Physical Review Letters, 1967. **19**(19): p. 1097-&.

28. Cheung, A.C., et al., *Phase Modulation of Q-Switched Laser Beams in Small-Scale Filaments.* Physical Review Letters, 1968. **20**(15): p. 786-&.

29. Agrawal, G.P., *Nonlinear fiber optics*. 4th ed. 2007, Amsterdam ; Boston: Elsevier / Academic Press. xvi, 529 p.

30. Brodeur, A. and S.L. Chin, *Ultrafast white-light continuum generation and self-focusing in transparent condensed media.* Journal of the Optical Society of America B-Optical Physics, 1999. **16**(4): p. 637-650.

31. Balu, M., *Experimental Techniques for Nonlinear Material Characterization; A Nonlinear spectrometer using a White-Light continuum Z-scan*, in *College of Optics and Photonics*. 2006, University of Central Florida: Orlando.

32. Sheikbahae, M., et al., *Sensitive Measurement of Optical Nonlinearities Using a Single Beam.* Ieee Journal of Quantum Electronics, 1990. **26**(4): p. 760-769.

33. Xia, T., et al., *Eclipsing Z-Scan Measurement of Lambda/10(4) Wave-Front Distortion.* Optics Letters, 1994. **19**(5): p. 317-319.

34. Kasha, M., *Characterization of electronic transitions in complex molecules.* Discuss. Faraday Soc., 1950. **9**: p. 14-19.

35. Xu, C. and W.W. Webb, *Measurement of two-photon excitation cross sections of molecular fluorophores with data from 690 to 1050 nm.* Journal of the Optical Society of America B-Optical Physics, 1996. **13**(3): p. 481-491.

36. Negres, R.A., et al., *Experiment and analysis of two-photon absorption spectroscopy using a white-light continuum probe.* Ieee Journal of Quantum Electronics, 2002. **38**(9): p. 1205-1216.

37. Negres, R.A., *Ultrafast nonlinear spectrometer for material characterization*. 2001, UCF/CREOL.

38. Wei, S.H. and A. Zunger, *Electronic and structural anomalies in lead chalcogenides.* Physical Review B, 1997. **55**(20): p. 13605-13610.

39. Streetman, B.G. and S. Banerjee, *Solid state electronic devices*. 6th ed. Prentice Hall series in solid state physical electronics. 2006, Upper Saddle River, N.J.: Pearson/Prentice Hall. xviii, 581 p.

40. Hines, M.A. and G.D. Scholes, *Colloidal PbS nanocrystals with size-tunable near-infrared emission: Observation of post-synthesis self-narrowing of the particle size distribution.* Advanced Materials, 2003. **15**(21): p. 1844-1849.

41. Rogach, A.L., et al., *Infrared-emitting colloidal nanocrystals: Synthesis, assembly, spectroscopy, and applications.* Small, 2007. **3**(4): p. 536-557.

42. Andreev, A.D. and A.A. Lipovskii, *Anisotropy-induced optical transitions in PbSe and PbS spherical quantum dots.* Physical Review B, 1999. **59**(23): p. 15402-15404.

43. Tudury, G.E., et al., *Effect of band anisotropy on electronic structure of PbS, PbSe, and PbTe quantum dots.* Physical Review B, 2000. **62**(11): p. 7357-7364.

44. Franceschetti, A., et al., *Origin of one-photon and two-photon optical transitions in PbSe nanocrystals.* Physical Review B, 2009. **79**(24)

45. An, J.M., et al., *The peculiar electronic structure of PbSe quantum dots.* Nano Letters, 2006. **6**(12): p. 2728-2735.

46. Peterson, J.J., et al., *Uncovering forbidden optical transitions in PbSe nanocrystals.* Nano Letters, 2007. **7**(12): p. 3827-3831.

47. Du, H., et al., *Optical properties of colloidal PbSe nanocrystals.* Nano Letters, 2002. **2**(11): p. 1321-1324.

48. Wehrenberg, B.L., C.J. Wang, and P. Guyot-Sionnest, *Interband and intraband optical studies of PbSe colloidal quantum dots.* Journal of Physical Chemistry B, 2002. **106**(41): p. 10634-10640.

49. Cademartiri, L., et al., *Size-dependent extinction coefficients of PbS quantum dots.* Journal of the American Chemical Society, 2006. **128**(31): p. 10337-10346.

50. Goupalov, S.V., *Selection rules for optical transitions in PbSe nanocrystal quantum dots: Drastic effect of structure inversion asymmetry.* Physical Review B, 2009. **79**(23)

51. Schaller, R.D., et al., *Breaking the phonon bottleneck in semiconductor nanocrystals via multiphonon emission induced by intrinsic nonadiabatic interactions.* Physical Review Letters, 2005. **95**(19)

52. Moreels, I., et al., *Size-Dependent Optical Properties of Colloidal PbS Quantum Dots.* Acs Nano, 2009. **3**(10): p. 3023-3030.

53. Moreels, I., et al., *Composition and size-dependent extinction coefficient of colloidal PbSe quantum dots.* Chemistry of Materials, 2007. **19**(25): p. 6101-6106.

54. Cotter, D., M.G. Burt, and R.J. Manning, *Below-Band-Gap 3rd-Order Optical Nonlinearity of Nanometer-Size Semiconductor Crystallites.* Physical Review Letters, 1992. **68**(8): p. 1200-1203.

55. Padilha, L.A., et al., *Frequency degenerate and nondegenerate two-photon absorption spectra of semiconductor quantum dots.* Physical Review B, 2007. **75**(7)

56. Ricard, D., P. Roussignol, and C. Flytzanis, *Surface-Mediated Enhancement of Optical-Phase Conjugation in Metal Colloids.* Optics Letters, 1985. **10**(10): p. 511-513.

57. Driggers, R.G., *Encyclopedia of optical engineering*. 2003, New York: Marcel Dekker. 3 v. (xvi, 3049, 55 p.).

58. Cirloganu, C., *Experimental and Theoretical Approaches to Characterization of Electronic Nonlinearities in Direct-Gap Semiconductors*, in *College of Optics and Photonics*. 2010, UCF: Orlando.

59. Ma, H., A.S.L. Gomes, and C.B. Dearaujo, *Measurements of Nondegenerate Optical Nonlinearity Using a 2-Color Single Beam Method.* Applied Physics Letters, 1991. **59**(21): p. 2666-2668.

60. Sheikbahae, M., et al., *Measurement of Nondegenerate Nonlinearities Using a 2-Color Z-Scan.* Optics Letters, 1992. **17**(4): p. 258-260.

61. Caruge, J.M., et al., *Transient photoluminescence and simultaneous amplified spontaneous emission from multiexciton states in CdSe quantum dots.* Physical Review B, 2004. **70**(8).

62. Bonati, C., et al., *Spectral and dynamical characterization of multiexcitons in colloidal CdSe semiconductor quantum dots.* Physical Review B, 2005. **71** (20)

63. Fisher, B., et al., *Multiexciton fluorescence from semiconductor nanocrystals.* Chemical Physics, 2005. **318**(1-2): p. 71-81.

64. Franceschetti, A. and M.C. Troparevsky, *Radiative recombination of triexcitons in CdSe colloidal quantum dots.* Journal of Physical Chemistry C, 2007. **111**(17): p. 6154-6157.

65. Klimov, V.I., et al., *Electron and hole relaxation pathways in semiconductor quantum dots.* Physical Review B, 1999. **60**(19): p. 13740-13749.

66. Bockelmann, U. and G. Bastard, *Phonon-Scattering and Energy Relaxation in 2-Dimensional, One-Dimensional, and Zero-Dimensional Electron Gases.* Physical Review B, 1990. **42**(14): p. 8947-8951.

67. Efros, A.L., V.A. Kharchenko, and M. Rosen, *Breaking the Phonon Bottleneck in Nanometer Quantum Dots - Role of Auger-Like Processes.* Solid State Communications, 1995. **93**(4): p. 281-284.

68. Clark, S.W., J.M. Harbold, and F.W. Wise, *Resonant energy transfer in PbS quantum dots.* Journal of Physical Chemistry C, 2007. **111**(20): p. 7302-7305.

69. Wise, F.W., *Lead salt quantum dots: The limit of strong quantum confinement.* Accounts of Chemical Research, 2000. **33**(11): p. 773-780.

70. Ai, X.C., et al., *Femtosecond investigation of charge carrier dynamics in CdSe nanocluster films.* Journal of Chemical Physics, 1997. **106**(8): p. 3387-3392.

71. Klimov, V.I., et al., *Quantization of multiparticle Auger rates in semiconductor quantum dots.* Science, 2000. **287**(5455): p. 1011-1013.

72. Padilha, L.A., et al., *Recombination processes in CdTe quantum-dot-doped glasses.* Applied Physics Letters, 2004. **85**(15): p. 3256-3258.

73. Robel, I., et al., *Universal Size-Dependent Trend in Auger Recombination in Direct-Gap and Indirect-Gap Semiconductor Nanocrystals.* Physical Review Letters, 2009. **102** (17)

74. Rupasov, V.I. and V.I. Klimov, *Carrier multiplication in semiconductor nanocrystals via intraband optical transitions involving virtual biexciton states.* Physical Review B, 2007. **76** (12)

75. Klimov, V.I., *Detailed-balance power conversion limits of nanocrystal-quantum-dot solar cells in the presence of carrier multiplication.* Applied Physics Letters, 2006. **89** (12)

76. Schaller, R.D., et al., *Seven excitons at a cost of one: Redefining the limits for conversion efficiency of photons into charge carriers.* Nano Letters, 2006. **6**(3): p. 424-429.

77. Mcguire, J.A., et al., *New Aspects of Carrier Multiplication in Semiconductor Nanocrystals.* Accounts of Chemical Research, 2008. **41**(12): p. 1810-1819.

78. Ellingson, R.J., et al., *Highly efficient multiple exciton generation in colloidal PbSe and PbS quantum dots.* Nano Letters, 2005. **5**(5): p. 865-871.

79. Nair, G., et al., *Carrier multiplication yields in PbS and PbSe nanocrystals measured by transient photoluminescence.* Physical Review B, 2008. **78**(12).

80. Pijpers, J.J.H., et al., *Assessment of carrier-multiplication efficiency in bulk PbSe and PbS.* Nature Physics, 2009. **5**(11): p. 811-814.

81. Schaller, R.D., V.M. Agranovich, and V.I. Klimov, *High-efficiency carrier multiplication through direct photogeneration of multi-excitons via virtual single-exciton states.* Nature Physics, 2005. **1**(3): p. 189-194.

82. Franceschetti, A., J.M. An, and A. Zunger, *Impact ionization can explain carrier multiplication in PbSe quantum dots.* Nano Letters, 2006. **6**(10): p. 2191-2195.

83. Fox, R.W., A.T. McDonald, and P.J. Pritchard, *Introduction to fluid mechanics*. 6th ed. 2004, New York: Wiley. xii, 787 p.

84. Holman, J.P., *Heat transfer*. 9th ed. McGraw-Hill series in mechanical engineering. 2002, New York: McGraw-Hill. xx, 665 p.

85. Cornish, R.J., *Flow in a Pipe of Rectangular Cross-Section* Proceedings of the Royal Society of London., 1928. **120**(786): p. 691-700.

86. Spiga, M. and G.L. Morini, *A Symmetrical Solution for Velocity Profile in Laminar-Flow through Rectangular Ducts.* International Communications in Heat and Mass Transfer, 1994. **21**(4): p. 469-475.

87. McGuire, J.A., et al., *Apparent Versus True Carrier Multiplication Yields in Semiconductor Nanocrystals.* Nano Letters, 2010. **10**(6): p. 2049-2057.

88. Hinds, S., et al., *Smooth-Morphology Ultrasensitive Solution-Processed Photodetectors.* Advanced Materials, 2008. **20**(23): p. 4398-4402.

89. Beard, M.C., et al., *Variations in the Quantum Efficiency of Multiple Exciton Generation for a Series of Chemically Treated PbSe Nanocrystal Films.* Nano Letters, 2009. **9**(2): p. 836-845.

Filename: Gero Nootz_PhD_2010 final.docx
Directory: C:\Users\Scott Webster\Desktop
Template: G:\Katie's share\Thesis & Dissertation\TD_ Forms and Files\T_D_Thesis and Dissertation template.dot
Title: UNIVERSITY OF CENTRAL FLORIDA
Subject:
Author: kgrigg
Keywords:
Comments:
Creation Date: 8/13/2010 2:43:00 PM
Change Number: 26
Last Saved On: 8/20/2010 11:26:00 AM
Last Saved By: Scott Webster
Total Editing Time: 859 Minutes
Last Printed On: 8/20/2010 11:47:00 AM
As of Last Complete Printing
Number of Pages: 129
Number of Words: 46,888 (approx.)
Number of Characters: 267,268 (approx.)